University of Southampton Research Repository

UNIVERSITY OF SOUTHAMPTON

FACULTY OF ENGINEERING AND PHYSICAL SCIENCES

Optoelectronics Research Centre

Development of Novel Mid-Infrared Optical Fibres

by

Andrea Ventura

A thesis submitted for the degree of Doctor of Philosophy

November 2020

Declaration of Authorship

I, ANDREA VENTURA, declare that this thesis titled, 'DEVELOPMENT OF NOVEL MID-INFRARED OPTICAL FIBRES' and the work presented in it are my own. I confirm that:

- This work was done wholly or mainly while in candidature for a research degree at this University.

- Where any part of this thesis has previously been submitted for a degree or any other qualification at this University or any other institution, this has been clearly stated.

- Where I have consulted the published work of others, this is always clearly attributed.

- Where I have quoted from the work of others, the source is always given. With the exception of such quotations, this thesis is entirely my own work.

- I have acknowledged all main sources of help.

- Where the thesis is based on work done by myself jointly with others, I have made clear exactly what was done by others and what I have contributed myself.

Signed:
_____

Date:
_____

UNIVERSITY OF SOUTHAMPTON

Abstract

FACULTY OF ENGINEERING AND PHYSICAL SCIENCES

Optoelectronics Research Centre

Doctor of Philosophy

by Andrea Ventura

The last decades have seen a steady progress in what mid-Infrared (mid-IR) technology can offer to medical, industrial, sensing, environmental and military applications. Remote thermal imaging and fibrerised mid-IR laser delivery are two applications for which special optical fibres that are flexible, sufficiently low loss and robust would be needed. Despite considerable work in the area, no such a solution exists yet that meets all the requirements.

In this thesis, the design, fabrication and characterisation of a fibre bundle for thermal imaging, as well as hollow core antiresonant fibres for mid-IR laser delivery are described. The final fabricated bundle is compact in outer diameter, flexible and allows thermal imaging with good resolution of objects as cold as a human body. Modelling work has also been performed to optimise the structure of the bundle for operation at longer wavelengths where cheap microbolometric thermal cameras work and where cold objects have their maximum infrared emission.

The second part of this thesis presents the design and fabrication of tellurite and chalcogenide hollow core antiresonant fibres aimed for the delivery of CO and CO_2 lasers radiation (5.4 and 10.6 μm), respectively. Several tellurite fibres with losses lower than 10 dB/m in the mid-IR spectral range, and a few preliminary chalcogenide prototypes have been obtained in the project.
Modelling studies conclude the work and illustrate how to decrease the optical losses of both tellurite and chalcogenide hollow core antiresonant fibres.

Acknowledgements

Looking over the past few years, I would like to express my deepest thanks to all the wonderful people that have made this experience possible. Firstly, I would like to thank my supervisor Prof. Francesco Poletti, which strongly supported, guided and motivated me during my three years of academic life. I would like to thank him for his helpful advices, for his endless patience and for being such a prominent figure in my studies. I thank him for allowing me to enter the world of optical fibres and for involving me in this fascinating research area.

I also would like to express my deepest gratitude to Dr Joris Lousteau for his help, guidance and for sharing his expertise during the first part of my PhD journey. I would also like to thank him for the choice of the bundle materials and for explaining me the fibre bundle fabrication process. I would like to express my deepest thanks to Dr Natalie Wheeler for her incredible support and for the endless times she managed to read my thesis. I cannot thank all my supervisors enough for giving responsibility and freedom for planning my research project. A special acknowledgment goes to Fedia, Juliano and Jaroslaw for helping and supporting me. Thanks to Jaroslaw for the tellurite glass billets and for its infinite patience. My research would have not been possible without the help of Nick, who trained me and allowed me to learn the extrusion process from scratch. I would also thank him for his time, explanations and suggestions. A particular thank goes to Dr Greg Jasion, who helped me with the simulations and scripts to import the geometry of fabricated fibres in Comsol. I would also thank Qiang Fu for his explanations about the OPO and for its help/suggestion during the fibre loss measurement using the OPO. Thanks to the ECS mechanical workshop and in particular to Mark Long, who made the fabrication of extremely precise extrusion dies possible. Without its patience I couldn't obtain the results of this thesis. I also thank the ORC/University of Southampton for supporting me.

I also thank Prof. Petr Janicek for the refractive index measurements of tellurite glass and FEP polymer, and for being available to discuss the results. I am grateful to thank all the colleagues I met at the ORC, especially Fernando, Andrea, Davide, Ilaria e Nico. A special person I met at the ORC is Francesco for all the help, suggestions and support inside and outside the university world and now he's one of my close friend.

Un ringraziamento particolare va ai miei genitori, a Daniela e ad Alice per il loro sostegno e per essermi stati sempre vicini nei momenti di difficoltà.

Ringrazio Susanna, Leon, Cecilia, Juan, Enrico, per la loro amicizia e per farmi sempre sentire a casa anche in un paese straniero. Ringrazio Michela, la mia dolce metà, che mi e' sempre stata vicino, mi ha capito, aiutato e incoraggiato, soprattutto durante il mio percorso di dottorato. Grazie a lei ho potuto completare questo splendido percorso della mia vita. Un grazie speciale va ad Enrico, Mariarosa e Francesco per essere sempre presenti e per la forza d'animo che quotidianamente mi trasmettono. Un sentito ringraziamento è dovuto ai miei nonni per l'affetto dimostratomi e per avermi saputo appoggiare in ogni occasione. Un grazie sincero va a tutti gli amici che mi sono stati vicini. Un ringraziamento particolare va al mio grande amico Alfonso, per avermi fatto conoscere un posto a me sconosciuto e per il suo continuo supporto anche da lontano. Infine vorrei ringraziare tutte le persone che con i loro consigli, critiche, suggerimenti e sostegno morale mi hanno permesso di crescere e migliorare.

Contents

List of Figures

List of Tables

Abbreviations

AOI	Angle of incidence
$BLIP$	Background Limited Infrared Detector
COP	Cyclic olefine polymer
D^*	Detectivity
$EWFD$	Electromagnetic Waves Frequency Domain
FEM	Finite Element Method
FEP	Fluorinated Ethylene Propylene
$FTIR$	Fourier Transform Infrared
$HC-AR$	Hollow core antiresonant
$HC-ARF$	Hollow core antiresonant fibre
HCF	Hollow core fibre
$HC-MOF$	Hollow core microstructured optical fibre
ID	Inner diameter
$InSb$	Indium Antimonide
$MCVD$	Modified Chemical Vapour Deposition
$mid-IR$	mid-Infrared
MCT	Mercury Cadmium Tellurite
NA	Numerical aperture
$NANF$	Nested antiresonant nodeless hollow core fibre
NEP	Noise Equivalent Power
OD	Outer diameter
OPO	Optical Parameter Oscillator
$PBGF$	Photonic Bandgap fibre
$PCVD$	Plasma-activated Chemical Vapour Deposition

PES	Polyethersulfone
PFA	Perfluoroalkoxy
PEI	Polyetherimide
$PMMA$	Poly Methyl Methacrylate
PML	Perfectly Matched Layer
R	Responsivity
TMM	Transfer matrix method

To my parents, my sister, Alice and Michela, who supported and encouraged me during this journey . . .

Chapter 1

Introduction

Over the last few decades, applications exploiting the mid-Infrared (mid-IR) range of the electromagnetic spectrum (3-50 μm) have gained progressively more importance for medical, industrial, sensing, environmental and military applications. The accessible mid-IR spectrum by present technology (3-12 μm) is particularly useful for surgery and material processing thanks to CO and CO_2 lasers [1, 2] and for chemical sensing and thermal imaging [3–6]. Mid-IR guiding optical fibres, thanks to their compactness, flexibility and length, give the possibility to exploit these applications in places where humans cannot access.

This thesis focuses on the development of optical fibre technologies capable of transmitting mid-IR radiation for two specific purposes: endoscopic thermal imaging and laser delivery. A coherent infrared fibre bundle has been developed to address the former, while the latter has been pursued through the design and fabrication of mid-IR hollow core optical fibres.

Thermal imaging consists of the detection of infrared radiation emitted from objects at a temperature higher than 0 K by using arrays of detectors and cameras sensitive to the infrared part of the spectrum where hot bodies emit electromagnetic radiation [7].

Although numerous infrared detectors and cameras have been developed over the years, and are now commercially available for use when direct sight of the object is possible, no commercial solution currently exists to obtain thermal images of hard to reach points. Numerous applications would benefit from an endoscope capable of collecting infrared/thermal images of places where humans cannot enter. This

would be extremely useful, for example, to check the state of thermal shields inside nuclear reactors, to study the heating of turbines in jet engines or to optimise industrial manufacturing processes [8, 9]. A potential solution to this problem would be a coherent fibre bundle able to guide infrared light. Fibre bundles operating in the visible spectral range have been available commercially for decades [10] and consist of an array of optical fibres fused over their entire cross-section or only at the extremities, where each core behaves as a pixel of the image one wants to transmit. The number of cores/pixels in a fibre bundle is important for the resolution of the transmitted images. Fibre bundles operating in the visible spectral range are based on silica glass, which is opaque above 3 μm wavelength. For this reason, in order to transmit thermal images through a fibre bundle, the core material must be based on mid-IR transparent glasses. Since these glasses have lower thermal and mechanical properties than silica, the fabrication of a fibre bundle for the mid-IR is more difficult compared to a bundle for the visible spectral range.

Several mid-IR fibre bundles have been reported in the literature using silver halide crystalline [11–13], hollow core [14, 15] and chalcogenide fibres [16–20]. The latter type shows better performance than silver halide and hollow core fibre versions and represents the closest technology in order to have a functional mid-IR bundle. Despite this, fibre bundles presented in literature have shown problems in terms of length, flexibility, dimensions and cross-talk between adjacent cores. In order to perform thermal imaging in hard to reach areas, a compact bundle that is flexible, with a length of at least a few metres, transparent in the mid-IR wavelength range and with a low inter-core cross-talk, is needed. This thesis reports design and fabrication work aimed at producing a fibre bundle for thermal imaging with such properties. In particular, a fibre bundle which consisted of 1200 chalcogenide glass cores and a Fluorinated Ethylene Propylene (FEP) polymer cladding has been fabricated using the stack and draw technique. The bundle was compact in outer diameter (1.1 mm), flexible and allowed to perform thermal imaging of human body through a length of 65 cm. The high refractive index contrast between the core glass and cladding polymer helped to obtain a low cross-talk, so that no qualitative image deterioration was noticeable.

Another problem, for which no convincing commercial solution currently exists, is that of the flexible delivery of mid-IR radiation from a suitable laser onto the application workbench through an optical fibre that is capable of handling high

power density and maintaining stable transverse operation. For this reason, in this project, after having developed a functional fibre bundle for thermal imaging, a mid-IR transmitting fibre for mid-IR laser delivery has been investigated. CO and CO_2 lasers are employed in surgery to cut tissues [1], in industrial applications to cut materials such as steel and polymer [2, 21, 22], and for gas sensing [23]. These lasers emit at 5.4 and 10.6 μm, respectively, and so these two wavelengths have been selected as a target for this project. Nowadays, only one commercial fibre exists for the delivery of CO_2 laser radiation of moderate powers, the Omniguide fibre [24]. This is a hollow core fibre exploiting an annular Bragg grating structure around the core to guide light. It works well for applications in medical surgery, but, it suffers from guidance of multiple modes, which prevents tight focusing of its output, and from the presence of low melting temperature polymer around the core, which limits the maximum total output power to a few 10s of Watts [25]. Developing fibres with a single Gaussian-shaped mode is essential for such applications where tight focusing and high cutting precision is needed. The only commercial instrument allowing transport of a Gaussian beam from laser to application workbench consists of a series of arms and mirrors [26]. Due to its large dimensions, it is a cumbersome solution with limited operability in inaccessible points. Since optical fibres represent a good solution to deliver laser radiation in the mid-IR, several solid and hollow core fibres have been developed in the past. Solid core fibres for mid-IR laser delivery are limited by the low melting temperature of the mid-IR glasses used, which prevents transmission of high power laser radiation [21, 27] and by the non-linearity of infrared materials [28]. Hollow core fibres can overcome these limitations. In particular, hollow core antiresonant fibres (HC-ARFs), which consist of one layer of several capillaries attached to a tubular jacket, have shown the best performances for laser delivery among hollow core fibres. Since silica HC-ARFs allow to guide light with acceptably low loss only up to $\sim$4.5 μm [29, 30], in order to transmit CO and CO_2 laser radiation, other glasses more transparent to mid-IR radiation must be used. Fabrication of such fibres using mid-IR glasses is more challenging than using silica glass due to their lower mechanical and thermal properties [31].

Different HC-ARFs for CO and CO_2 laser delivery have been reported in the literature based on tellurite, borosilicate and chalcogenide glasses [32–37]. Some of these works only achieved very short fibre lengths and/or presented non-uniformities due to the fabrication process. In particular, two different methods have been used in

the past to develop mid-IR HC-ARFs: the stack and draw method and the extrusion and draw method. The latter enables production of HC-AR preforms where the capillaries are already fully fused to the preform jacket tube. Furthermore, an extrusion-based approach minimises the number of thermal steps needed to fabricate the final HC-ARF, avoids the dislocations of capillaries during the draw and potentially reduces non-uniformities.

In the second part of this thesis, the fabrication of tellurite and chalcogenide HC-ARFs using the extrusion and draw method, for CO and CO_2 laser delivery, respectively, is reported. This work shared materials and processes with the mid-IR bundle projects and benefited from the knowledge and experience acquired in producing mixed glass-polymer fibres for the bundles. The HC-ARFs produced in this thesis are coated with FEP polymer to protect them from environmental scratches. The polymer's low Young's modulus gives the fibres enhanced flexibility, representing an improvement over all previous uncoated attempts reported in the literature. The best fibres produced in this project were based on tellurite glass and have loss of 8.2, 4.8 and 6.4 dB/m at 5 μm, 5.6 μm and 5.8 μm, respectively. By improving the fibre structure and uniformity, modelling suggests that losses of the order of 0.05 dB/m can be achieved at both 5.4 and 10.6 μm.

1.1   Outline

Following this introduction, the thesis is structured as follows:

In Chapter 2, the background of solid core fibres, including their guidance and loss mechanisms, as well as their fabrication methods is reported. Moreover, the Finite Element Method (FEM), used extensively in this work to simulate the loss of solid core fibres, is introduced and a study aimed at producing accurate simulations with a low error is reported.

In Chapter 3, some background concepts about thermal imaging are first presented. Then, the state of the art of mid-IR fibre bundles for thermal imaging is described.

Chapter 4 describes the fabrication method of a mid-IR fibre bundle made of chalcogenide glass core and FEP polymer cladding fibres. Moreover, in this chapter, the characterisation of the fibre bundles material is reported. In the last part,

the technique developed to polish several fibre bundle ends at the same time is described.

Chapter 5 reports detailed characterisation of the fibre bundle. In particular, the loss of the fibre bundle was measured with the cut-back method. The fibre bundle was tested by using a thermal camera and thermal images of a human hand were obtained using a 65 cm long fibre bundle. Additionally, the inter-core cross-talk was measured. The last part of this chapter presents a modelling study aimed at improving the fibre bundle in future iterations and to make it transparent between 8 and 12 μm wavelength, the spectral region where low temperature objects as the human body have the highest emission and low-cost thermal cameras operate.

Chapter 6 describes the motivation for producing low loss mid-IR optical fibres, in particular for CO and CO_2 laser delivery. The second part of the chapter reports the relevant theory (including guidance mechanisms and loss components) and the fabrication methods of HC-ARFs. Two studies are reported to validate the accuracy of FEM models for straight and bent fibres. In addition, a literature review describing state of the art of mid-IR HC-ARFs is presented.

In Chapter 7, the selection of materials needed to fabricate HC-ARFs transparent at $\sim$5 and $\sim$10 μm, is presented. HC-ARF structures able to transmit with very low losses at these wavelengths are designed and the fabrication method of mid-IR tellurite and chalcogenide HC-AR preforms is described. In particular, the optimisation of the fabrication process, which enabled fabrication of HC-AR preforms with uniform capillaries, is reported.

Chapter 8 focuses on the description of the fabrication and characterisation of tellurite and chalcogenide HC-ARFs. The chapter is concluded with FEM studies aimed to understand the future steps needed to decrease the fibre loss further.

In Chapter 9, overall conclusions for the work presented in this thesis are given and a future perspective is drawn.

Chapter 2

Background on fibre optics

In this chapter, the background of solid core fibres, necessary to understand the guiding mechanism of optical fibres, their loss mechanisms and their fabrication techniques, is presented. In the first part, the guiding mechanism and the fabrication methods of solid core fibres are described. The second part of this chapter provides an introduction to the FEM which has been used extensively in this thesis to simulate the loss of solid core fibres. The accuracy of the simulation models, which I developed to simulate straight waveguide loss in an optical fibre, has been verified by reproducing known results and obtaining a low relative error.

2.1   Optical fibre

An optical fibre is a waveguide that has the function of transmitting light with low attenuation. Optical fibres are composed by a core, where the light is transmitted, surrounded by a cladding which minimises the light leaking out into the core of adjacent fibres (i.e. array of optical fibres) [38, 39]. The vast majority of optical fibres have a cylindrical symmetry and the most estensively used and successfully deployed optical fibres rely on a step or graded refractive index profile to confine light in the core.

2.1.1 Solid core fibre

In conventional optical fibres, the refractive index of the core n_0, is higher than that of the cladding n_1. In these fibres, the cladding refractive index is typically uniform along the radius whereas the core refractive index can be uniform (step index fibre) as shown in Figure 2.1a or graded along the radius (graded index fibre) as shown in Figure 2.1b [40]. Other kind of optical fibres are the double clad fibre and dispersion-shifted fibres [41]. Step index fibres (Figure 2.1a) have a core refractive index which is constant and they present an abrupt index change at the core-cladding interface. In graded index fibres (Figure 2.1b), the core refractive index shows its maximum value at the centre of the core and it decreases gradually within the core to its minimum value at the core-cladding boundary [41]. In double-clad fibres, the core region, which has a constant refractive index n_0, is surrounded by a cladding layer with a lower refractive index than that of the core n_1 and another cladding layer with a refractive index n_2 which is between the refractive index of the first cladding layer n_1 and that of the core n_0 (Figure 2.1c) [41]. In dispersion-shifted fibres, the core refractive index has a triangular shape with its maximum at the centre of the core n_1 and a double clad (Figure 2.1d) [41].

In the fabrication of conventional silica-based fibres, it is possible to control the refractive index profile in the preform fabrication phase by using vapour phase techniques. In this thesis, the use of a mid-IR transmitting glass was needed (see Chapter 4), where vapour phase techniques are challenging [31]. Also, since a high refractive index contrast between core and cladding was required as described in Chapter 4, the rod-in-tube method [42] was used to fabricate the fibre and I focussed on step index fibre designs. The simplest way to understand light guidance in an optical fibre is using ray tracing optics. Light propagating in an optical fibre is confined into the core region thanks to the mechanism of total internal reflection. A ray, which is incident from free space into the air-core interface with an angle θ_i, is refracted with an angle θ_r (Figure 2.2). The relationship between the incident and the refracted angle is described by the famous Snell's law

$$n_{air} sin\theta_i = n_0 sin\theta_r \tag{2.1}$$

where n_{air} and n_0 are the air and the core refractive index, respectively. The refracted ray propagates in the core until it hits the core-cladding interface with
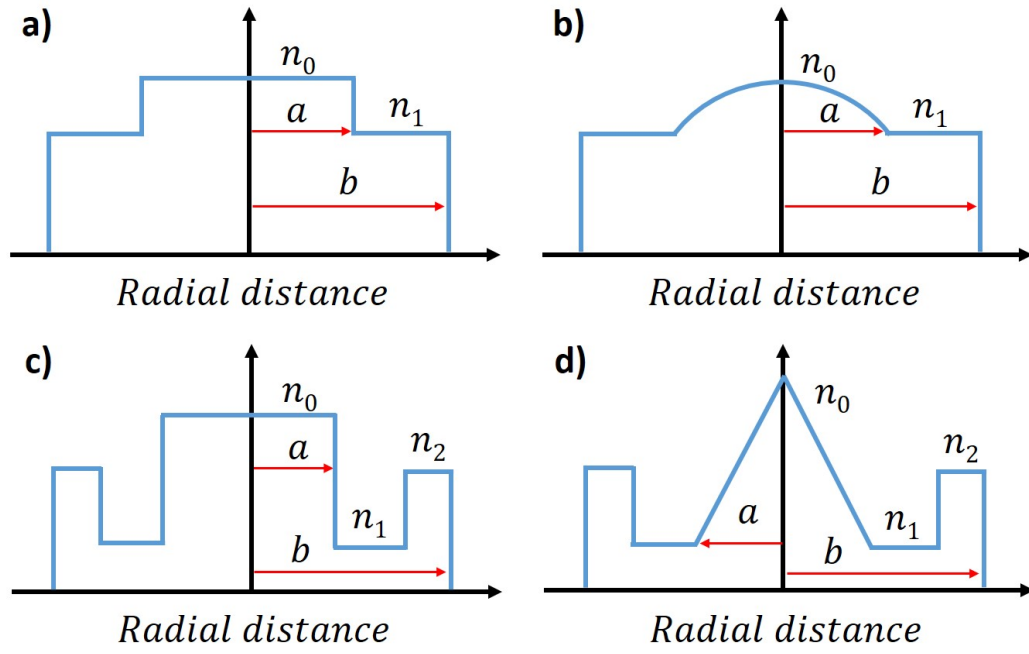
FIGURE 2.1: Refractive index profile of (a) step index fibre, (b) graded index fibre, c) double clad fibre and d) dispersion-shifted fibre [41]. The core radius and the fibre radius are indicated as a and b, instead n_0, n_1 and n_2 represent the refractive index of the core, the first cladding layer and the second cladding layer.

an angle ϕ (Figure 2.2). If the angle ϕ is greater than the critical angle ϕ_c, defined as

$$sin\phi_c = \frac{n_1}{n_0},$$ (2.2)

light is reflected at the core-cladding interface and it is confined into the core. This is the so-called total internal reflection and it is shown in Figure 2.2a. If ϕ is smaller than the critical angle ϕ_c, a fraction of the incident light is refracted at the core-cladding interface and is lost, i.e. it cannot be guided along the fibre [41] as shown in Figure 2.2b. By combining Equations 2.1 and 2.2 it is possible to calculate the numerical aperture NA of the fibre, which is expressed as

$$n_{air}sin\theta_i = n_0cos\phi_c = \sqrt{n_0^2 - n_1^2} = NA$$ (2.3)

which determines the maximum acceptance angle of an incident ray from free space into the air-core interface θ_i. The higher the NA, the larger the acceptance angle θ_i [43]. To have a high NA, the core refractive index must be much higher than that of the cladding.
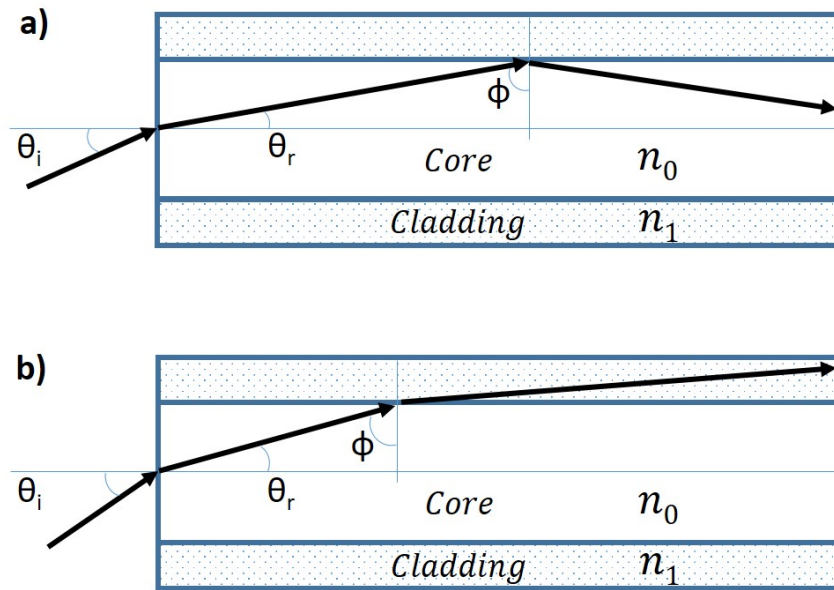
FIGURE 2.2: a) Reflection of the light incident to the core-cladding interface and b) refraction of the light incident to the core-cladding interface [41].

The light propagation mechanism through an optical fibre can also be described more accurately by the electromagnetic waveguiding theory starting from Maxwell equations, which for a non-conductive and a non-magnetic medium are expressed as

$$\nabla \times \mathbf{E} = -\frac{\partial \mathbf{B}}{\partial t} \tag{2.4}$$

$$\nabla \times \mathbf{H} = \frac{\partial \mathbf{D}}{\partial t} \tag{2.5}$$

$$\nabla \cdot \mathbf{D} = 0 \tag{2.6}$$

$$\nabla \cdot \mathbf{B} = 0 \tag{2.7}$$

where $\mathbf{E}$ and $\mathbf{H}$ represent the electric and magnetic fields, respectively [41] and they are in cylindrical coordinates ($\mathbf{E}$(r,ϕ,z) and $\mathbf{E}$(r,ϕ,z)) assuming an implicit time dependence of the fields exp(-iωt). $\mathbf{B}$ and $\mathbf{D}$ are the magnetic and electric

flux densities and they are expressed as

$$\mathbf{B} = \mu_0 \mathbf{H} \tag{2.8}$$

$$\mathbf{D} = \epsilon_0 n^2 \mathbf{E} \tag{2.9}$$

where n, ϵ_0 and μ_0 represent the refractive index, the vacuum permittivity and the vacuum permeability, respectively. By taking the curl of Equation 2.4 and combining Equations 2.5, 2.8, 2.9, one can obtain the following equation [41]

$$\nabla \times (\nabla \times \mathbf{E}) - n^2 k_0^2 \mathbf{E} = 0 \tag{2.10}$$

where k_0 is the vacuum wave vector. For a step index fibre, since the refractive index n is constant along the radial direction for both core and cladding, it is possible to simplify Equation 2.10 inside either core or cladding as

$$\nabla \times (\nabla \times \mathbf{E}) = \nabla(\nabla \cdot \mathbf{E}) - \nabla^2 \mathbf{E} = -\nabla^2 \mathbf{E} \tag{2.11}$$

giving the wave equation

$$\nabla^2 \mathbf{E} + n^2 k_0^2 \mathbf{E} = 0 \tag{2.12}$$

When appropriate boundary conditions are set for example the continuity of the field at the core/clad interface, this equation becomes an eigenvalue equation which involves Bessel functions [43] (see Section 2.3.2). Bessel functions are defined as cylindrical functions because they are present in the solution of Laplace's equation in cylindrical coordinates. The eigensolutions of the eigenvalue equation are the propagating modes. Since the refractive index is constant along the z axis (propagation direction), the solution of the wave equation for the electric and magnetic field can be expressed as

$$\mathbf{E}_j = \mathbf{e}_j(r, \phi)e^{i\beta_j z} \tag{2.13}$$

$$\mathbf{H}_j = \mathbf{h}_j(r, \phi)e^{i\beta_j z} \tag{2.14}$$

where e_j/h_j and β_j represent the eigenvector and the propagation constant or eigenvalue for the j-th mode, respectively [40].

In an ideal step index fibre the modes are bound and there is no loss. The core and cladding materials however add some unavoidable attenuation due to absorption and Rayleigh scattering [40]. This causes the attenuation of the propagating light and it is due to absorption of the fibre material and Rayleigh scattering [41]. The material absorption can be classified as intrinsic and extrinsic absorption. Intrinsic absorption is related to the transmission window of the fibre material [41]. In particular, a glass has a transmission window that is limited in the short wavelength region by ultraviolet absorption and in the long wavelength region by multiphonon absorption [41]. The ultraviolet absorption is associated to the transition of electrons from the valence to the conduction band [44]. The multiphonon absorption, which limits the transmission of the glass in the long wavelength region, is due to strong vibrations of the glass molecules and atoms [44]. Extrinsic absorption is related to the waveguide physical imperfections and impurities of the fibre material [45]. These impurities are attributed to contamination, crystallisation and, for example, water which can be present in the fibre material. In fact, oxide glasses show a strong absorption peak due to OH vibration [46].

The attenuation due to Rayleigh scattering, which is another intrinsic mechanism of loss, limits the short wavelength region of the transmission window of a glass, and it is due to density fluctuations of the fibre material. These density fluctuations, cause a variation in the refractive index [41]. The Rayleigh scattering causes a loss (α_R) in optical fibres which can be expressed as

$$\alpha_R = \frac{C}{\lambda^4} \tag{2.15}$$

where C is a constant which depends on the fibre material [41]. In Chapter 4 I will show the absorption of the core glass which I used to fabricate solid core mid-IR transmitting fibres.

In the case of absorbing optical fibre, the propagation constant is complex and it is defined as

$$\beta_j = k_0(n + ik) \tag{2.16}$$

where $n + ik$ is the complex refractive index. Its imaginary part k represents the extinction coefficient such that

$$k = \frac{\alpha\lambda}{4\pi}, \tag{2.17}$$

where α represents the power absorption coefficient and it is expressed in m^{-1} and λ is the free-space wavelength. By substituting the complex propagation constant in Equations 2.13 and 2.14, the electric and magnetic fields become

$$\mathbf{E}_j = \mathbf{e}_j(r, \phi)e^{ik_0nz}e^{-k_0kz} \tag{2.18}$$

and

$$\mathbf{H}_j = \mathbf{h}_j(r, \phi)e^{ik_0nz}e^{-k_0kz} \tag{2.19}$$

The term e^{-k_0kz} represents the electric and magnetic fields attenuation.

The modes of an optical fibre with cylindrical symmetry can be classified as [40]:

- hybrid modes (HE_{vm} or EH_{vm})

- transverse electric (TE_{0m}) modes ($E_z = 0$)

- transverse magnetic (TM_{0m}) modes ($H_z = 0$).

The subscript v represents the order of the Bessel functions. For each v, m solutions exist [46]. In a step index fibre the number of propagation modes is regulated by the normalised frequency called V-number expressed as

$$V = \frac{2\pi\rho\sqrt{n_{core}^2 - n_{cladding}^2}}{\lambda} = \frac{2\pi\rho}{\lambda}NA \tag{2.20}$$

where ρ is the core radius, λ is wavelength and the term $\sqrt{n_{core}^2 - n_{cladding}^2}$ is the NA [45]. The number of guided modes in an optical fibre for high V-number values (V≫1) [40] can be approximated as

$$M \approx \frac{V^2}{2}. \tag{2.21}$$

As I will show in Chapter 4, the solid core fibres which were used to develop a fibre bundle for thermal imaging, have a high index contrast between core and cladding

(Δn>1.4), and then a high NA (NA>2) and a V$\gg$1. The high index contrast fibre was chosen to improve the confinement of the optical modes into the core and to minimise the cross-talk between cores in the fibre bundle. Having a high V-number, the fibre bundle will be multimode and the high order modes will cause a higher power in the cladding compared to low order modes. In order to reduce this power in the cladding due to high order modes, a single mode fibre bundle could be the solution. However, in a multimode fibre bundle the high order modes will not propagate up to the end of the bundle because of their high loss, so they will not affect the inter-core cross-talk. Moreover, since the fundamental mode in a multimode fibre has a lower power in the cladding compared to a single mode fibre, a multimode fibre bundle represents the best option to reduce the cross-talk.

To simulate the fraction of power in the core for a generic propagation mode (see Chapter 5), I applied the following procedure. The total power flow in an optical fibre for each j-mode (P_j) can be calculated by integrating the Poynting vector over an infinite cross section (A_∞) and it is

$$P_j = \frac{1}{2} \int_{A_\infty} e_j \times h_j^* \cdot \hat{\mathbf{z}} dA. \tag{2.22}$$

In order to calculate the amount of power inside the core for each propagating mode, it is possible to calculate the fraction of modal power in the core η_{j-core} which is defined as

$$\eta_{j-core} = \frac{power\ flow\ within\ the\ core}{total\ power\ flow}. \tag{2.23}$$

In particular, the fraction of power within the core for each propagating mode is expressed as

$$\eta_{j-core} = \frac{\frac{1}{2} \int_{A_{core}} e_j \times h_j^* \cdot \hat{\mathbf{z}} dA}{P_j}, \tag{2.24}$$

where A_{core} is the core cross section. By likewise replacing the cladding area $A_{cladding}$ to the core area in the equation above, it is possible to calculate the fraction of mode power within the cladding $\eta_{j-cladding}$ [40]. Figure 2.3 shows the fraction of modal power within the core for a fibre with NA=2 as a function of its V-number. Here, the fundamental mode has the highest fraction of power in the core for a given V-number. The fraction of modal power within the core
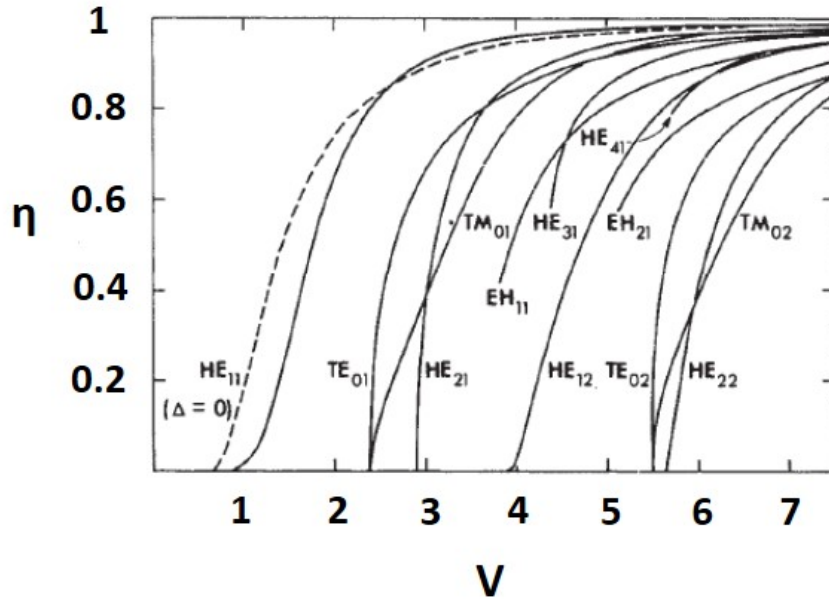
FIGURE 2.3: Fraction of modal power within the core for a fibre with NA = 2 as a function of V-number (Reproduced from [40]).

varies between 0 and 1 and it increases with the V-number. By increasing the V-number, the fibre guides more and more modes; simultaneously, the confinement in the core of all guided modes is increased. Starting from the fraction of the total modal power in the core and the cladding area and by knowing the core and cladding bulk material loss (α_{core} and $\alpha_{cladding}$, respectively), the attenuation constant γ' of an optical fibre due to absorption in the core and cladding can be estimated as [47]

$$\gamma' = (\alpha_{core} \times \eta_{core}) + (\alpha_{cladding} \times \eta_{cladding}) \tag{2.25}$$

2.2 Solid core fibre fabrication

The current procedures to fabricate optical fibres using a drawing tower were invented over 60 years ago [39]. The fabrication of solid core fibres consists of drawing a fibre from a solid preform, or directly from a melt thanks to the double crucible technique [48]. The preform can be fabricated using several techniques, such as Modified Chemical Vapour Deposition (MCVD) method [49], Plasma-activated Chemical Vapour Deposition (PCVD) method [50] and the rod-in-tube method [42, 51]. The MCVD and PCVD techniques are hugely used for silica solid

core fibres [49, 50]. The rod-in-tube is the most used method to develop preforms made from soft-glasses [31]. Since in this project I worked with soft-glasses as chalcogenide and tellurite glasses, I have focussed here only on the rod-in-tube preform fabrication technique.

2.2.1 Solid core preform fabrication

The rod-in-tube technique allows combination of different materials to form the core and cladding of the fibre [42]. In the rod-in-tube technique, there are two main approaches to fabricate the preform. The first one consists of the realisation of a preform where the core is already embedded into the cladding [52], while the second one, and most widely employed approach in the development of soft-glass fibres, relies on the development of the preform by inserting a glass rod which represents the core into a cladding tube [42, 51]. The first approach of the rod-in-tube technique consists of pouring a melt glass which represents the core into a cladding tube [52].

In the second approach, the core rod can be developed by casting the glass in a specific mould directly from melt or by extrusion, whereas the cladding tube can be obtained by rotational casting, drilling or extrusion [31]. Rotational casting consists of the casting of a melt glass into a mould and then the mould is rotated until the glass is cooled down [31]. This method enables fabrication of a glass tube [31]. Mechanical or ultrasonic drilling techniques can be used to obtain tellurite, fluoride and chalcogenide glass tubes [31]. In both the cases of casting and drilling, the glass rod and tube surfaces need to be polished after they have been detached from their moulds to reduce the glass surface roughness which could introduce scattering in the final fibre [31, 53–55].

In Chapter 4, I will show the fabrication of solid core preforms made by a commercial chalcogenide core rod and a commercial polymer cladding tube using the rod-in-tube technique.

The extrusion process consists of the deformation of a billet of glass or polymer through a die aperture which confers the desired cross section to the material [56]. This provides an alternative means to fabricate glass rods and tubes. Figure 2.4 shows the schematic of the extrusion setup. In particular, a billet of glass is inserted inside a sleeve which is connected to a die [57]. Then, the sleeve and the
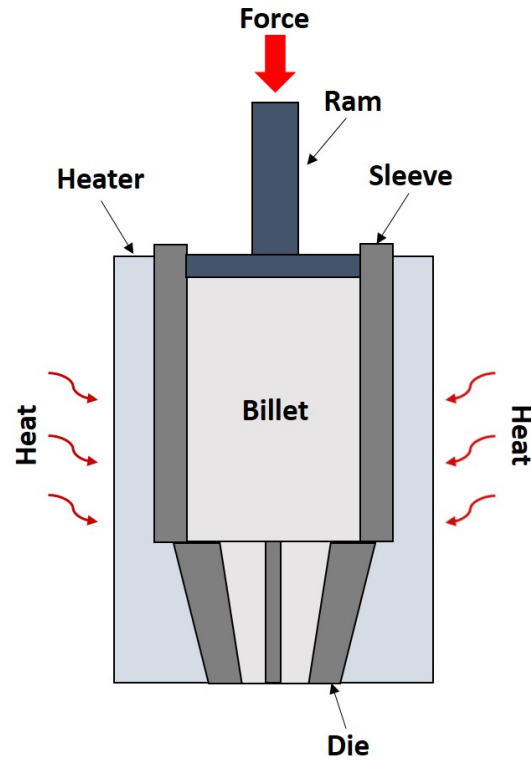
FIGURE 2.4: Schematic of extrusion setup [57].

die are inserted inside an extrusion heater [57] which regulates the billet material temperature and hence its viscosity thanks to a controller. By applying a force on the billet through a ram which is placed on top of the billet and by moving the extrusion heater in the opposite direction of the ram with a constant speed or force, the material inside the billet comes out from the die [57]. The design of the extrusion die is important for the shape of the extruded preform [57]. Figures 2.5a and b show a sleeve with an extrusion die for thin rods and an extrusion die for thin capillaries, respectively. The key parameters of extrusion are the temperature of the material in the sleeve, the force applied to it and the speed of the extrusion heater [31, 57]. By optimizing these parameters, it is possible to obtain a straight preform with shiny surfaces (i.e. without crystallisation) and with dimensions that are close (but never identical) to those of the extrusion die. Extrusion enables fabrication of preforms with a polished surface. This is because the extruded preform cools down in free space and it is not in contact with solids [57] as in the case of the rod-in-tube method. The preform length is limited by the billet volume. The extrusion temperature is related to the viscosity-temperature curve of the billet material. The curves of fluoride, chalcogenide and silica glass which are shown in Figure 2.6 were extracted from Tao et al. [31]. In addition,
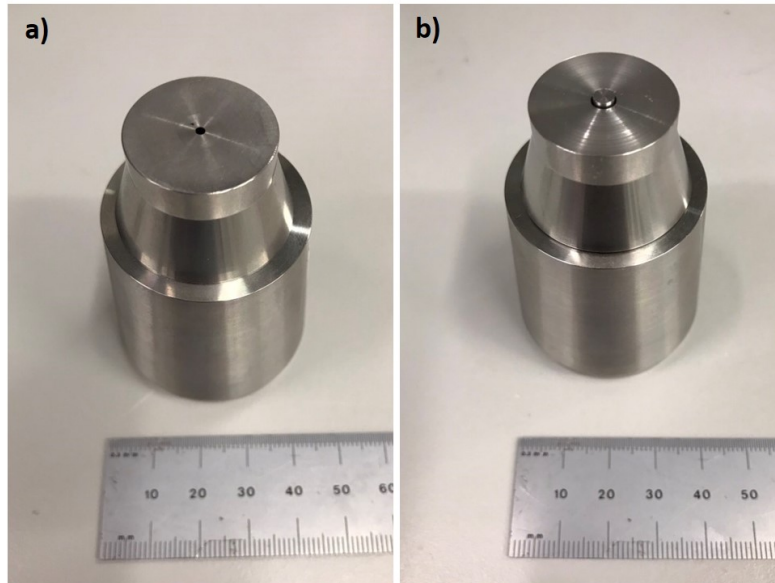
FIGURE 2.5: Extrusion sleeve and die for (a) thin rods and for (b) thin capillaries.

the viscosity-temperature curve of tellurite glass measured by my colleague Dr Jaroslaw Cimek is also shown in Figure 2.6. The viscosity range at which a billet
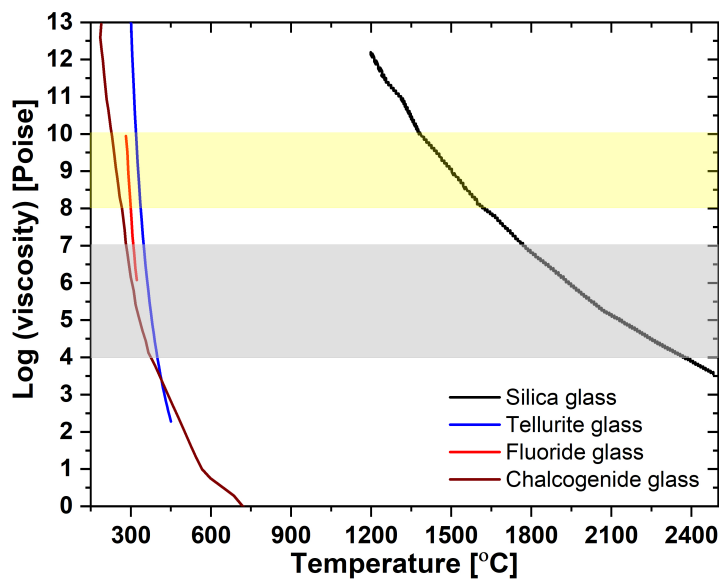
FIGURE 2.6: Viscosity dependence on the glass temperature for tellurite glass (blue curve), fluoride glass (red curve), chalcogenide glass (brown curve) and pure silica glass (black curve). The grey area represents the viscosity range for fibre drawing (10^4-10^7 Poise) [31]. Instead, the yellow area represents the viscosity range for glass extrusion (10^8-10^{10} Poise) [57]. Reproduced from [31].

can be extruded is between 10^8-10^{10} Poise (grey area in Figure 2.6) [57]. The steepness of the viscosity-temperature curves is important for the range of usable

temperatures at which a material can be extruded. The steeper the curve, the narrower the extrusion temperature range. By reducing this range, the extrusion is more difficult because a small variation in the glass temperature causes a change of viscosity. As shown in Figure 2.6 silica glass has a flatter viscosity-temperature curve compare to tellurite, chalcogenide and fluoride glasses. For this reason, the extrusion temperature range for silica glass is larger than tellurite, fluoride and chalcogenide glasses. Extruding at a high viscosity leads to an increased force applied on the billet. In Chapter 7, I will show several attempts to extrude tellurite and chalcogenide glass billets by having a constant speed of the extrusion heater. In my experiments, for example, I applied loads between 5 and 12 kN to extrude billets of TZBK tellurite glass at temperatures between 336 and 340 °C at a speed between 0.15 and 0.5 mm/min. In contrast, for chalcogenide glass extrusion, I applied loads of the order of 27 kN to the billet and the temperature and the speed of extrusion were of 348 °C and 0.05 mm/min, respectively. Chalcogenide glass was extruded at a higher viscosity compared to tellurite glass to minimise crystallisation. This explains the higher extrusion load applied to extrude the chalcogenide billet compared to the tellurite one.

2.2.2 Solid core fibre drawing

Solid core optical fibres can be obtained from the fibre drawing process. In particular, two different approaches can be adopted to draw a solid core optical fibre. The first approach, the double crucible method, consists of simultaneously drawing the core and the cladding directly from a melt [48]. The second approach is to draw it from a fabricated solid preform. In this work, the fibres reported are all fabricated from solid preforms. This is because, as shown in Chapter 4, the core rod and cladding tube used in this project were commercially available.

Figure 2.7 shows a schematic of the fibre drawing process. The preform, which is held by a mechanical clamp is fed vertically into a drawing furnace. Once the bottom of the preform is heated at a temperature higher than the preform material softening point, the glass softens and it is pulled into a fibre thanks to gravity or by the force provided by a capstan, which rotates at a given speed. The furnace of the drawing tower can be purged with inert gases as Argon or Nitrogen to minimise contaminations. As shown in Figure 2.7, it is possible to read instantly the fibre diameter through a laser based diameter gauge. In addition to this, in order to improve the mechanical robustness of the fibre, often a polymer coating is applied

to the fibre and then cured in an UV curing oven [42]. During the fibre draw, the
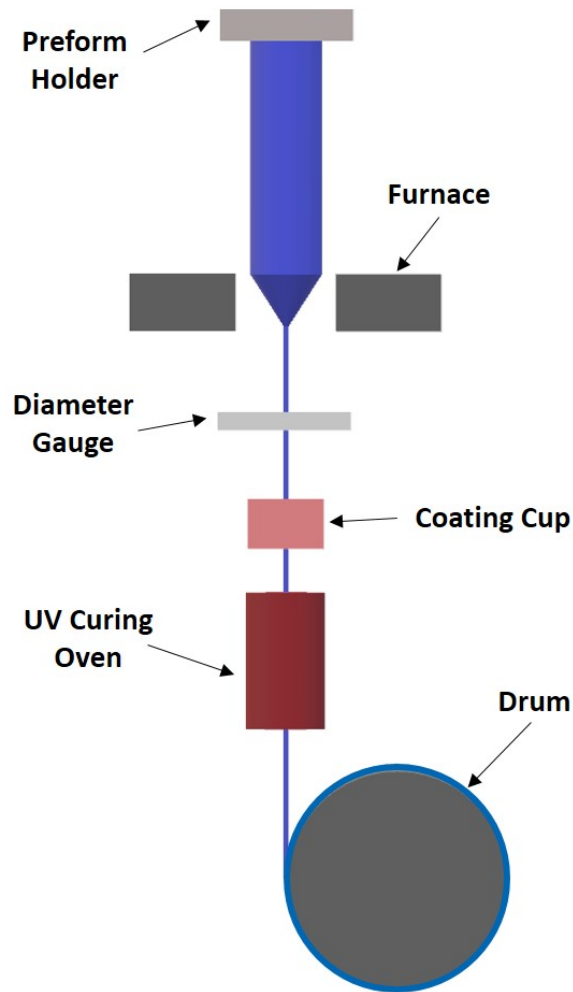
FIGURE 2.7: Schematic of fibre drawing process [42].

preform is fed with a feeding rate v_f, and the fibre is drawn at a drawing speed v_p. By changing both parameters it is possible to regulate the fibre diameter D_f, such that:

$$D_f = D_p \sqrt{\frac{v_p}{v_f}} \tag{2.26}$$

where D_p is the preform diameter [58].

The drawing temperature of a fibre depends on the viscosity of the glass. The viscosity range at which a material can be drawn into a fibre is between 10^4-10^7 Poise (grey area in Figure 2.6) [31]. Silica glass shows an almost flat viscosity-temperature behaviour. Instead soft-glasses have a steeper viscosity-temperature

curve than silica glass. This explains one of the difficulties of fabricating solid core fibres made of mid-IR glasses compared to silica fibres.

A glass with a steep viscosity-temperature curve is more difficult to draw compared to a glass with a flat viscosity curve. This is because, for a steep viscosity-temperature curve, the temperature range that needs to be achieved, controlled and maintained for the drawing process is considerably narrower [31].

The grey area of Figure 2.6 represents the viscosity range for fibre drawing (10^4-10^7 Poise) [31]. The yellow area represents the viscosity range for glass extrusion (10^8-10^{10} Poise) [57]. Again, it is noticeable that silica glass gives the possibility to draw optical fibres in a broader temperature range compared to infrared glasses.

2.2.3   Coherent fibre bundle

One of the objectives of this thesis is to fabricate a coherent fibre bundle which is transparent in the mid-IR spectral range between 3 and 12 μm, in order to transmit thermal images of targets placed in inaccessible areas. A coherent fibre bundle consists of an array of optical fibres. The fibre bundle concept was developed to generate standard (non-thermal) images of hard to reach areas inside the human body. Flexible and coherent fibre bundles made by stacking together an array of optical fibres, each of which represent a pixel, were developed in the 1950s to assist medical endoscopy [59] and they are now commercially available from multiple suppliers. Thanks to direct pixel matching between the bundle ends, in coherent fibre bundles, images on the input surface can be recreated on the output surface. In contrast, in incoherent fibre bundles the image on the input surface cannot be reproduced on the output surface, since the fibres forming the pixels have not maintained their reciprocal location within the bundle, and some sort of image processing is needed to form distinguishable images. Figures 2.8a and 2.8b show a coherent fibre bundle and an incoherent fibre bundle [60], respectively.

There are two main techniques used to develop a fibre bundle, namely the coil winding method [61] and the stack and draw approach [62]. The first one consists of the realisation of carefully aligned layers of individual optical fibres directly on drum as the fibres are drawn. Then, a number of fibre layers are epoxied, clamped and sliced at a certain point on the drum. In this way, the fabricated fibre bundle is mechanically flexible, thanks to the cementation of the only bundle ends. For example, Nishii et al. [17] developed a fibre bundle, 1 metre long, by cementing

FIGURE 2.8: a) Coherent and b) incoherent fibre bundle [60].

only the ends of 8400 AsS core and Teflon cladding fibres. The diameter of each fibre was 75 μm. Although the bundle was 5.3 x 7.8 mm in dimension, it was flexible thanks to the cementation of its ends. However, the challenge of this method is to handle small fibres. This is because by decreasing the dimension of the fibres, they can be fragile and also they can be flexible. Their flexibility could represent a problem since fibres can move during the cementation step. So, the fibre bundle could not be perfectly coherent due to potential dislocations of fibres. The second approach, namely the stack and draw technique, which is the method of choice for commercial visible bundles, typically, consists of several steps. A preform made of a cladding tube (Figure 2.9a) and a core rod (Figure 2.9b) is drawn into a fibre (Figure 2.9c). Then, pieces of fibre are stacked together (Figure 2.9d) and inserted in a jacket tube (Figure 2.9e). As a last step, the stack and the jacket tube are drawn into a fibre bundle (Figure 2.9e). The cores in the fibre bundle obtained from the stack and draw method, are embedded in a matrix material with a lower refractive index. This method allows the fabrication of a flexible fibre bundle by a single draw of stacked fibres and it might present some advantages for the fibre bundle coherency. It is also possible to obtain fibres/pixels with small core dimensions ($\sim$3 μm) directly from the draw. This represents an advantage compared to the coil winding method where it is hard handling fibres with such small dimensions. For these reasons, the stack and draw technique was chosen for the present work (see Section 4.2).

The materials used for the fabrication of the fibre bundle are important for its performance and efficiency. Fabrication of a practical fibre bundle for the mid-IR
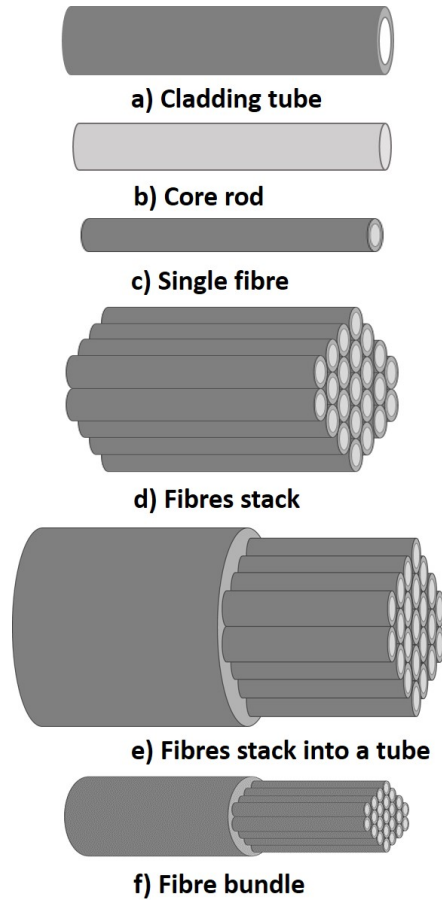
FIGURE 2.9: A schematic of the stack and draw technique.

is considerably more challenging than a fibre bundle for the visible spectral range, for numerous reasons. In the visible spectral range, the fibre cores in the bundle are small in diameter ($\sim$3 μm). For the transmission in the mid-IR spectral range the fibre bundle cores need to be larger. So, in order to obtain a fibre bundle with high spatial resolution, its outer diameter (OD) must be larger than the visible one, which could have an impact on the fibre bundle flexibility. As I will show in Chapter 4, the use of a matrix material with a low Young's modulus helps to give mechanical flexibility to the fibre bundle for the mid-IR region. The wavelength transmission range of the fibre bundle depends on the core material transmission. Fibre bundles in the visible spectral range are made with cores of silica glass and transmit between 0.4 and 2.3 μm. Mid-IR bundles, in contrast, need a core transparent in the infrared region [19]. In order to minimise the inter-core crosstalk between adjacent fibres, a high index contrast is also needed.

2.3 Modelling

In order to study the modal properties of an optical fibre, I used the FEM [63]. By using this method, it is possible to predict the modal properties of an optical fibre prior to fabrication, allowing the fabricator to target the best fibre dimensions/structure in order to achieve low transmission loss and optimum performance for a specific application. This minimises the time and the amount of material and money needed to produce optimised optical fibres. The FEM shows a good accuracy and computational speed and can also model complex fibre structures such as microstructured optical fibres [63]. In addition to this, commercial FEM solvers are well established, fast and accurate. For this reasons, I have decided to study the attenuation of solid core fibres by using the FEM. This has been implemented using Comsol Multiphysics.

2.3.1 Comsol Multiphysics

Comsol Multiphysics [64] is a powerful software that can model and simulate multiphysics problems such as heat transfer, fluid flow, structural mechanics, chemical engineering and optics thanks to the FEM [65]. The FEM allows to discretise a complex structure into little elements in a structured mesh and calculate the solution for each element. Different mesh shapes such as triangular and quadrilateral can be chosen [64]. The accuracy of the solution can be improved by increasing the number of elements (mesh) in the computational domain [43]. This leads to a longer computation time [66].

In order to study the modal properties of optical fibres, the physics interface called Electromagnetic Waves Frequency Domain (EWFD) [67] found in the Wave Optics Module can be used. The EWFD interface can calculate eigenvalues β_j and eigenvectors $\mathbf{e}_j(r, \phi)$ of the wave equation

$$\nabla^2 \mathbf{E} + n^2 k_0^2 \mathbf{E} = 0 \tag{2.27}$$

The eigenvalues of the problem can be expressed as the complex propagation constant

$$\beta_j = k_0(n + ik) \tag{2.28}$$

The rate of optical loss induced by propagation through an optical fibre can be calculated from the imaginary part of the complex propagation constant k

$$\alpha(dB/m) = \frac{4\pi k 10 log(e)}{\lambda} \tag{2.29}$$

In order to evaluate the accuracy of the FEM, it is necessary to run a convergence test optimizing the mesh size of the model until the results become close to those of analytical solutions. In other words, when this convergence is reached, the error between the analytical and the FEM solution is at its minimum.

2.3.2 Step-index fibre model validation

In order to validate a step-index fibre based on the FEM, an optical fibre toolbox which is implemented in Matlab [68] was used. It solves the characteristic equation which is defined as

$$\left[\frac{J'_n(u)}{u J_n(u)} + \frac{K'_n(w)}{w K_n(w)} \right] \left[n_0^2 \frac{J'_n(u)}{u J_n(u)} + n_1^2 \frac{K'_n(w)}{w K_n(w)} \right] = \frac{\beta^2}{k_0^2} \left(\frac{1}{u^2} + \frac{1}{w^2} \right)^2 n^2 \tag{2.30}$$

where $J_n(u)$ and $K_n(w)$ represent the Bessel and the modified Bessel functions, respectively and $J'_n(u)$ and $K'_n(w)$ represent their derivatives [43]. The terms u and w represent the normalised tranverse wave vector in the core and in the cladding, respectively and they are expressed as

$$u = a\sqrt{k_0^2 n_0^2 - \beta^2} \tag{2.31}$$

and

$$w = a\sqrt{\beta^2 - k_0^2 n_1^2} \tag{2.32}$$

By reducing the mesh size in Comsol, the difference between the solution of the analytical model and the FEM model decreases. This leads to a computation time increasing. So, the choice of the mesh size is a trade-off between the FEM model accuracy and the solution time.

Since in this thesis a fibre made of Vitron IG3 chalcogenide glass core and FEP polymer cladding was investigated (see paragraph 4.1), the convergence test was performed on a fibre made of these materials.

In Comsol, a fibre geometry with a core of 40 μm in diameter and a cladding of 180 μm in diameter was created. A Perfectly Matched Layer (PML) was added to the fibre geometry to avoid any reflection of the electric and magnetic field at the boundary [69–71]. The real and imaginary part of the complex refractive index of the core and cladding materials were set on Comsol. The real part of the complex refractive index n of the Vitron IG3 glass shown in Figure 4.1 was used for the core. The extinction coefficient k for the core material (Equation 2.17) was calculated from the attenuation of the Vitron IG3 glass as measured by using the Fourier Transform Infrared (FTIR) spectrometer with the cut-back method (Figure 4.1).

For the cladding material, the real part of the refractive index n, of the FEP polymer measured using variable angle spectroscopic ellipsometer IR-VASE, J. A. Woollam Co by Prof. Petr Janicek (Figure 4.1), was used. The exctinction coefficient k for the cladding material was calculated from the attenuation measurements carried out on a sample of FEP polymer by using a FTIR spectrometer (Figure 4.1).

Due to the high refractive index contrast between the core and the cladding material, the fibre is highly multimoded. For example, at 3 μm wavelength a fibre with a core diameter of 40 μm supports about 5000 propagation modes. A triangular shaped mesh was optimised by performing a convergence test on the fundamental mode and a generic mode. In this case, the 10th mode was selected. In this way, the accuracy of the model can be proved also for high order modes.

The fibre model was simulated in Comsol at 3 μm wavelength by changing the mesh element size in the core where most of the field is localised. The mesh size was kept fixed in the cladding region. The effective index (n eff) of the fundamental mode at mesh element size of $\lambda/3.75$, $\lambda/4.28$, $\lambda/5$, $\lambda/6$, $\lambda/7.5$ and $\lambda/10$ is shown in Figure 2.10a (blue curve). To verify the accuracy of the Comsol solution, the effective index (n eff) was calculated by using the optical fibre toolbox for a fibre with a core diameter of 40 μm (red curve). As shown in Figure 2.10a, by decreasing the element size hmax, the Comsol solution becomes closer to the analytical solution. To quantify the accuracy of the Comsol model, the error expressed as the difference of the effective index of the fundamental mode calculated analytically and the effective index of the fundamental mode simulated in Comsol was calculated. This error is shown in Figure 2.10b. It was found that an element size hmax equal to $\lambda/5$ represents a good trade-off between the solution error and the computation time, which is shown in Figure 2.11. The solution error was of

7.11 x 10^{-8}. To double check the Comsol model accuracy, the HE31 mode accu-
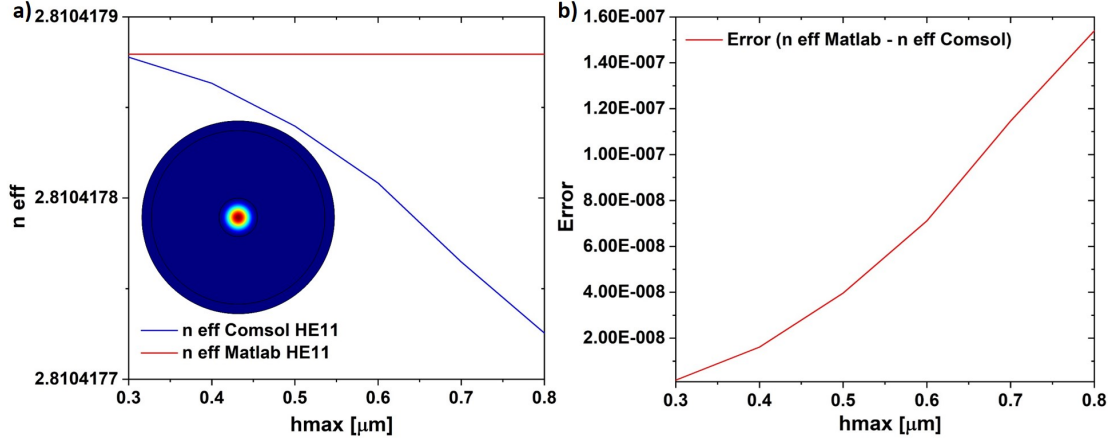
FIGURE 2.10: Validation of a solid step index fibre: a) effective index (n eff) of the fundamental mode (HE11) calculated analytically (red curve) and effective index (n eff) of the fundamental mode (HE11) simulated in Comsol (blue curve); b) Error between the effective index of the fundamental mode (HE11) calculated analytically and the effective index (n eff) of the fundamental mode (HE11) simulated in Comsol.
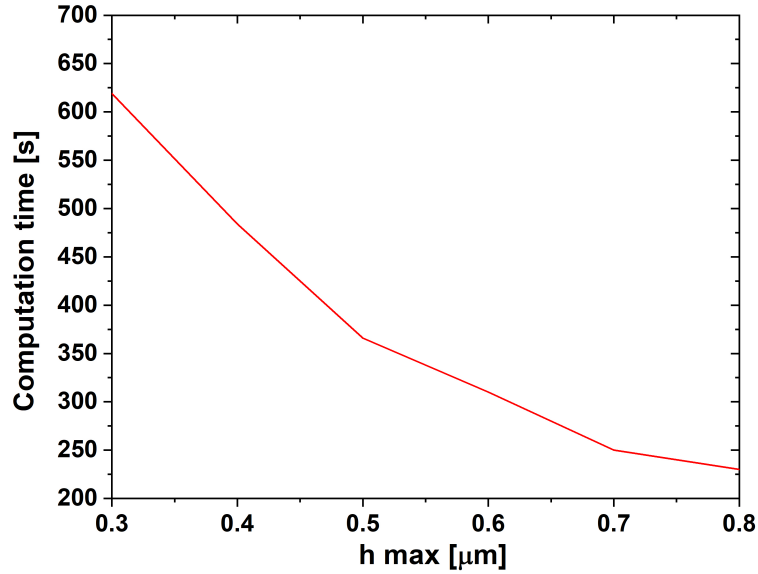
FIGURE 2.11: Simulation time in second for a step-index fibre for different element sizes.

racy was also investigated. Figures 2.12a and b show the calculated (red curve) and simulated (blue curve) effective indices of the HE31 mode. An element size of $\lambda/5$ gives a solution error of 1.86 x 10^{-6} which is small considering that the Comsol and analytical solutions differ only at the 6th decimal digit. So, also in this case, it was found that an element size of $\lambda/5$ represents a good compromise

between the solution accuracy and the computation time. This information has been used in all subsequent simulations in this thesis.
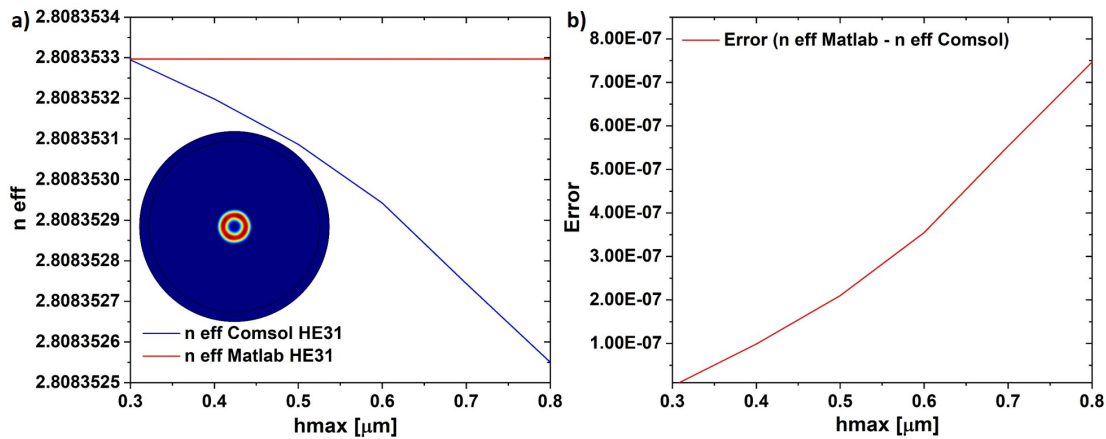
FIGURE 2.12: Validation of a solid step index fibre: a) effective index (n eff) of the HE31 mode calculated analytically (red curve) and effective index (n eff) of the HE31 mode simulated in Comsol (blue curve); b) Error between the effective index of the HE31 mode calculated analytically and the effective index (n eff) of the fundamental mode (HE31) simulated in Comsol.

2.4   Conclusion

In this chapter, background material relevant to solid core fibres has been presented. The fabrication methods of solid core fibres have been presented. In particular, the extrusion process and the fibre drawing process have been reviewed, to provide the reader with the basic information to understand the experimental work discussed in the following chapters. In addition to this, the fibre modelling study has been explained, including the validation model for solid core fibres. In the following chapter the background on thermal imaging and mid-IR transparent materials is presented.

Chapter 3

Mid-Infrared thermal imaging

In this chapter, the background on thermal imaging and the state of the art in terms of the fabrication of infrared fibre bundles for thermal imaging for application in hard to reach areas are presented.

3.1 Thermal imaging

Nowadays, thermal imaging is becoming a standard inspection technique in medical, industrial and military applications, thanks to the continuous development and improvement of lenses, filters and detectors that operate in the mid-IR wavelength region [3–6]. This technique is mainly used in medicine to study skin inflammation, skin diseases, tissues and for cancer diagnosis [3]. In the military field, thermal imaging is employed for improving night vision in cases of weak illumination, darkness and poor weather conditions [4].

Thermal imaging captures electromagnetic radiation in the mid-IR spectral range (3-12 μm) through a thermal camera, where objects at a temperature above 0 K emit electromagnetic radiation [7]. Thermal imaging can obtain thermal maps, called thermograms of a generic target mostly through the use of thermal cameras [7]. Thermal cameras are based on infrared detectors that detect the incident radiation by absorbing it and converting it into a current or a voltage signal [72]. Different thermal cameras have been developed in the past and they can be classified based on the kind of infrared detector and then on the wavelength operation range.

3.1.1 Infrared detectors

Infrared detectors are classified into two main classes as photon and thermal detectors [73]. In photon detectors, infrared radiation is absorbed by interaction with a semiconductor detector material and this produces an electric signal. In particular, the infrared radiation, which hits photon detectors, interacts with free or bound electrons. This causes a change in the electronic energy distribution and then generates an electric signal [72, 74]. Since photon detectors are based on semiconductor materials they detect in a limited wavelength range. This is because the energy of the incoming photon must be greater than the bandgap energy of the material. The absorption curve of a photon detectors shows a cut off at long wavelengths where the photon energy is close to the bandgap energy of the material [74]. This kind of detector has the highest signal to noise ratio, a high detectivity and they are fast in terms of time response. Since thermal generation makes photon detectors noisy, cryogenic cooling is required. This minimises the thermal noise of photon detectors but makes thermal cameras heavy, bulky and expensive [74]. Photon detectors are classified as quantum well detectors, extrinsic detectors, intrinsic detectors and photoemissive detectors [74].

In thermal detectors, the absorbed infrared radiation induces a change in temperature of the detector material; this leads to a variation of its physical properties and then to a generation of an electric signal proportional to the incoming IR radiation [72–74]. Thermal detectors are able to detect over a large wavelength range since the detection process is independent from the photonic nature of the incoming radiation [74]. Thermal detectors are classified as microbolometer detectors, pyroelectric detectors and thermoelectric detectors [74]. In microbolometer, pyroelectric and thermoelectric detectors, the infrared radiation absorption induces a change in the material resistance, of the internal electrical polarisation of the detector material and a voltage difference, respectively, which results in a generation of an electric signal [72–75]. Since thermal detectors are uncooled, thermal cameras equipped with this kind of detector are cheaper and smaller than the one equipped with photon detectors. Thermal detectors show a slower time response and they also have a lower detectivity compared to photon detectors [74]. The detector properties as the Responsivity (R), the Noise Equivalent Power (NEP) and the spectral Detectivity (D^*), are crucial parameters for the detector performance and efficiency. The Responsivity is defined as the ratio between the electrical output signal I_p and the incident energy P (expressed in Watt) on the detector

surface as:

$$R = \frac{I_p}{P}[A/W] \tag{3.1}$$

The Noise Equivalent Power (NEP) is the ratio between the noise per unit bandwidth and the responsivity (Equation 3.2). It represents the radiant power that produces a signal that is equal to the noise. It represents the weakest signal can be detected.

$$NEP = \frac{I_N}{R}[W] \tag{3.2}$$

where I_N is the noise current. The Detectivity (D^*) allows comparison of different detectors. D^* is the ratio between the square root of bandwidth (B) times the detector area (A_D) and the NEP (Equation 3.3) [72]:

$$D^* = \frac{(A_D B)^{1/2}}{NEP}[cmHz^{1/2}/W] \tag{3.3}$$

Figure 3.1 shows the spectral response in terms of the Detectivity of infrared detectors in the mid-IR wavelength range. The spectral response of infrared detector decreases with increasing wavelength due to a theoretical limit. This theoretical limit, called Background Limited Infrared Detector (BLIP), is due to the fluctuation background radiation. In particular, the infrared radiation incident into an infrared detector is a combination between the radiation emitted from the object and the radiation from the background. In the ideal case, in order to get the amount of radiation emitted from an object it is possible to subtract the background radiation from the radiation that arrives to the detector. However, the background radiation fluctuates and it is hard to estimate the amount of this fluctuation. Since this fluctuation represents a noise that cannot be removed from the detected radiation, the higher is the difference in temperature between the object under investigation and the background, the lower is the effect of this noise. Objects at a temperature close to the room temperature (background temperature) emit in the long wavelength region. This explains why the BLIP decreases as the wavelength increases. For example, InGaAs detectors, which operate between 0.7 and 1.7 μm, have a Detectivity of approximately at 5 x 10^{12} cmHz$^{1/2}$/W, which is higher than that of Indium Antimonide (InSb) and Mercury Cadmium Tellurite (MCT) detectors which operate at longer wavelengths. InSb detectors detect

the infrared radiation between 1 and 5 μm offering the higher Detectivity (approximately 2 x 10^{10} cmHz$^{1/2}$/W) compared to MCT and PbSe detectors, in the same spectral region. MCT detectors show a Detectivity of the order of 1 x 10^{10} cmHz$^{1/2}$/W between 8 and 12 μm. In this spectral range, microbolometer detectors have a Detectivity of 1 x 10^8 cmHz$^{1/2}$/W. Since there is a little interest in
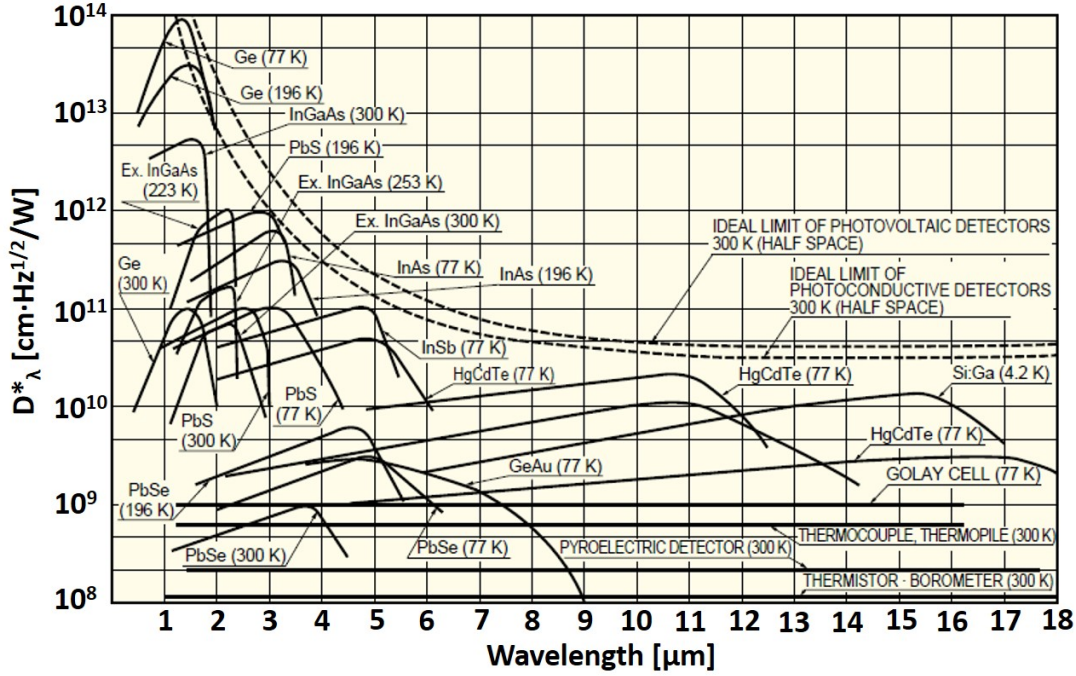
FIGURE 3.1: Spectral response of infrared detectors at different wavelengths. Reproduced from [78].

the spectral ranges where the atomospheric absorption is high, the most common infrared detectors operate in the two main spectral regions 3-5 μm and 8-12 μm, where the spectral atmospheric transmissivity is high (Figure 3.2) [76, 77].

3.1.2 Blackbody radiation

A generic body that absorbs all the incoming radiation without reflection and emits completely the absorbed radiation is defined as a blackbody. Any object at a temperature above 0 K emits an electromagnetic radiation according to Planck's law which represents the spectral radiant exitance and it is expressed as:

$$E(\lambda, T) = \frac{C_1}{\lambda^5} \frac{1}{exp\frac{C_2}{\lambda T} - 1} [W/m^2 \mu m] \tag{3.4}$$
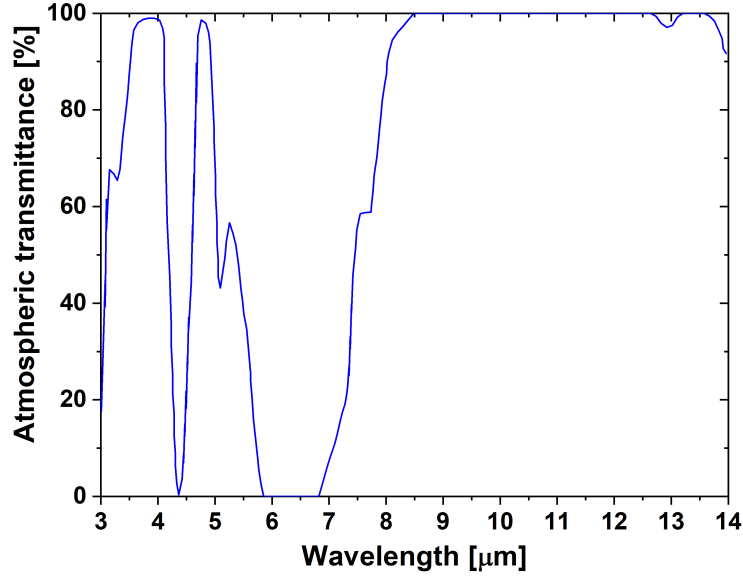
FIGURE 3.2: Spectral atmospheric transmittance. Reproduced from [77].

where T is the absolute temperature, λ is the wavelength, C_1 and C_2 are radiation constants [76] and they are equal to:

$$C_1 = 3.74 \times 10^8 [W \mu m^4 / m^2] \tag{3.5}$$

$$C_2 = 1.44 \times 10^4 [\mu m K] \tag{3.6}$$

Planck's law depends on the wavelength and on the surface temperature of the object. Figure 3.3 represents the spectral radiant exitance as a function of the wavelength and of the object temperature. Any object has its own value of emissivity ϵ, which is defined as the ratio between the effective emission of the body and the blackbody emission at the same body temperature [76]:

$$\epsilon = \frac{\int_{\lambda_0} \epsilon(\lambda) E(\lambda, T) d\lambda}{\int_{\lambda_0} E_{bb}(\lambda, T) d\lambda} \tag{3.7}$$

Its value varies between 0 and 1, according to the material and the body surface [76]. For example aluminium, zinc and tungsten have a low emissivity value as 0.05, 0.2 and 0.05, respectively. On the other hand, water, ice and quartz have high emissivity values of 0.98, 0.97 and 0.93, respectively. Steel has different values of emissivity according to the material surface. In fact, a strongly oxidised steel has an emissivity of 0.88, but a steel with a rough surface shows an emissivity of 0.96
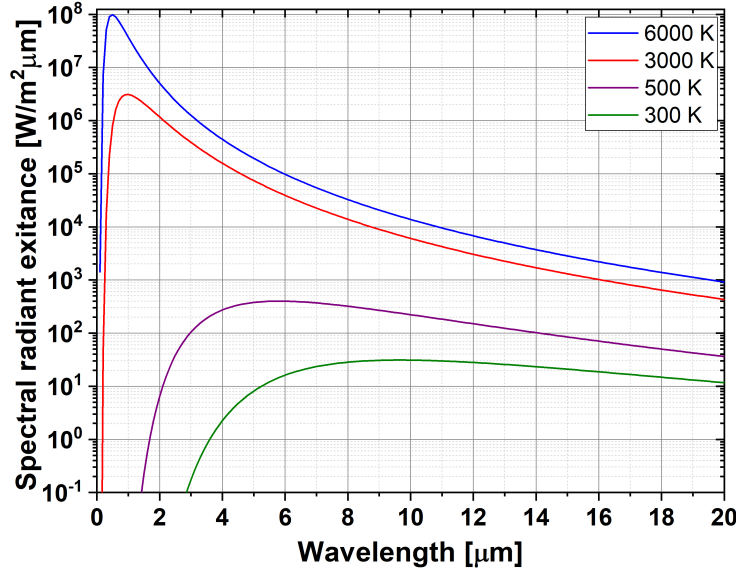
FIGURE 3.3: Spectral radiant exitance of a blackbody at different temperatures.

[79]. A blackbody shows the best value of emissivity ϵ and it is equal to 1 [76]. As shown in Figure 3.3, the peak of the spectral radiant emittance is function of the body temperature [72]. The exact wavelength of the infrared radiation peak can be obtained by differentiating Planck's law respect to wavelength and by setting the result to zero. This leads to Wien's displacement law and it is expressed as [76]:

$$\lambda_m T = 2898 [\mu m K] \tag{3.8}$$

Hence, objects at room temperature (T = 300 K) have a spectral emission peak at approximately 10 μm. For hotter objects, this peak is shifted to shorter wavelengths. In particular, a body at T = 3000 K and at T = 6000 K show spectral emission peaks at 1 μm and 0.48 μm, respectively. So, the colder the object, the longer the radiation wavelength that needs to be detected. Using the Stefan-Boltzmann law, shown in Equation 3.9, the total radiant emittance can be calculated by integrating the Planck's law over the wavelength [76].

$$E = \int_0^n E(\lambda, T) d\lambda = \sigma T^4 [W m^{-2}] \tag{3.9}$$

where σ is the Stefan-Boltzmann constant:

$$\sigma = 5.67 \times 10^{-8} [W m^{-2} K^{-4}]. \tag{3.10}$$

This law indicates that the total radiant emittance depends on the object temperature and that colder bodies emit significantly lower power.

By combining the Stefan-Boltzmann law and the decrease of the Detectivity as wavelength increases, this explains why mid-IR thermal imaging is technically more difficult compared to near-IR thermal imaging. Nowadays, one of the current limitations of mid-IR thermal imaging is the lack of a coherent fibre bundle, such as the borescope in the visible spectral range, that thanks to its flexibility, high resolution and insensibility to vibrations allows to investigate hard to reach areas. Such a device operating in the mid-IR region would be useful for numerous thermal imaging applications.

3.2 Mid-IR transmitting material

In the last few decades different materials transparent to the mid-IR have been studied. They include tellurite, germanate, fluoride and chalcogenide glasses [31], and halide and sapphire crystals. In this work, I focused only on mid-IR transparent glasses because they are drawable into fibres. Although these glasses enable transmission at wavelengths where silica glass is opaque, the mechanical and optical properties of the infrared fibres made from non-silica glass are typically worse than silica glass fibres [31]. Infrared glasses are more fragile than silica glass [80]. Fluoride and some chalcogenide glasses show a low chemical durability due their reaction with water [81, 82]. As mentioned in Chapter 2, the fabrication of infrared glass fibres is more challenging than silica glass fibres due to their steep viscosity-temperature curve [31]. For example, silica glass has a drawable temperature range of $\sim$600 °C, while for chalcogenide glass this range is only $\sim$100 °C.

Table 3.1 reports some of the physical and optical properties of infrared glasses [2, 31, 83–90].

As it is possible to see from this table, germanate, tellurite, fluoride and chalcogenide glasses transmit well beyond silica glass, which transmits up to $\sim$4.3 μm (see green curve Figure 7.1 in Chapter 7). Fluoride glasses (e.g. ZBLAN) have the lowest refractive index. On the other hand, chalcogenide glasses (As_2S_3, As_2Se_3 and GeAsSeTe) exhibit the highest refractive index and they transmit at longer wavelengths compared to other infrared glasses.

	ZBLAN	*GeO2*	*TeO2*	*As2S3*	*As2Se3*	*GeAsSeTe*
Tg [°C]	265	478	290	187	170-285	275
Refractive index (n)	1.49	1.91	1.91	2.39	2.6	2.81
Transmission range [μm]	0.3-7.5	0.5-5.5	0.4-6	1.5-6.5	2-10	1.5-20

TABLE 3.1: Physical and optical properties of infrared crystals and glasses [2, 19, 31, 83–94].

3.2.1 Mid-IR transmitting glasses

In search for best glass to use in this project, four main families of glass were considered. These were fluoride, germanate, tellurite and chalcogenide glasses. The most used composition of fluoride glasses consists of ZrF_4, HfF_4 and AlF_3 [83]. The refractive index of fluoride glasses is ∼1.49 at 1.55 μm. These glasses are transparent across wavelengths between 0.3 and 7.5 μm [31]. A key disadvantage of fluoride glass is the poor chemical stability due to moisture sensitivity [31, 84]. For this reason, fluoride glass fibres should be used in a dry environment [31]. Another disadvantage is the low crystallisation stability compared to chalcogenide glasses [31]. In addition to this, fluoride glasses are limited in terms of mechanical strength [86].

Germanate glasses (GeO_2) have a refractive index of 1.91 at 1.55 μm and the shortest cut-off wavelength between mid-IR glasses (5.5 μm) [91].

Tellurite and chalcogenide glasses offer different properties which makes them attractive for the aims of this thesis, as it will be shown in Chapters 4 and 7. For this reason it was chose to investigate both. Tellurite glasses are mainly made from TeO_2. One of the most common glass composition consists of TeO_2-ZnO-Na_2O. Tellurite glasses have a refractive index of 1.91 at 3 μm and a transmission spectrum between 0.4 and 6 μm wavelength [31]. Different tellurite glass compositions have been studied to minimise crystallisation [92].

Chalcogenide glasses are made by elements of the VIa group from the periodic table, such as S, Se, Te combined with elements from the groups IV and V, such as As, Ge, Sb, Ga [85]. Chalcogenide glasses have a lower glass transition temperature, larger refractive index and broadest transmission window compared to other infrared glasses and crystals. In addition to this, some chalcogenide glasses are thermally stable against crystallisation and insensitive to moisture [26]. For these reasons, chalcogenide glasses are largely used for infrared applications as laser delivery and thermal imaging in military, industrial and medical fields [95]. Different chalcogenide glasses have been studied in the past. They are classified as

sulfide (AsS), selenide (AsSe) and telluride (GeAsSeTe) chalcogenide glasses. In particular, telluride chalcogenide glasses (GeAsSeTe) have a refractive index which is higher than sulfide chalcogenide glasses (AsS) [88]. The addition of elements as tellurium, germanium and selenium broadens the transmission window [26], as shown in Table 3.1. Telluride (GeAsSeTe) chalcogenide glasses are transparent between 1.5 and 20 μm in wavelength [31]. Furthermore, telluride chalcogenide glasses have low phonon energies [85] and their thermal stability means that they can be drawn into fibres without crystallisation [96].

3.3 Mid-IR fibre bundle for thermal imaging: state of the art

Fabrication of a practical fibre bundle for the mid-IR is considerably more challenging than for the near-IR for numerous reasons. First, the material choice, as discussed above, often mid-IR transmitting glasses are more difficult to draw, more prone to crystallisation and with a shorter lifetime than the silica/silicate glasses typically used for the visible spectral range. Then, the dimensions of each individual pixel needs to be much larger in order to scale with the wavelength, which makes the fabrication of flexible bundles more challenging. Finally, the unfavourable combination of Stefan-Boltzmann law and decreased detectivity means that thermal imaging is harder than imaging in the near-IR. Despite this, several fibre bundles transparent in the mid-IR wavelength region have been demonstrated in the last few decades, by using silver halide crystalline fibres [11–13], hollow core fibres [14, 15] and chalcogenide fibres [16–20]. Silver halide crystalline and hollow core fibre bundles present limitations in terms of number of pixels, loss and length, and are very difficult to fabricate. In comparison, fibre bundles based on chalcogenide glasses are the most promising in terms of performance and they show the possibility to overcome these limitations. For this reason, in this work as will be shown in Chapter 4, chalcogenide glass was chosen to develop a fibre bundle transparent in the mid-IR.

3.3.1 Silver halide crystalline fibre bundles

Two fibre bundles, both 30 cm long, made of 160 and 1300 silver halide (AgClBr) fibres were developed by Paiss et al. [11]. These fibre bundles were fabricated by multiple extrusion processes. The cross section of the two fibre bundles was 3 mm^2. The fibre bundles were flexible and transmitted between 4 and 20 μm in wavelength. The fibre bundles of 160 and 1300 fibres had attenuation equal to 8 and 17 dB/m at 10.6 μm wavelength, respectively. The multiple extrusion processes caused problems related to inhomogeneity in the fibre bundle [11].

Rave et al. [12] developed fibre bundles made of 100-9000 AgClBr fibres, also by multiple extrusion processes. The fibre bundle areas and lengths ranged from 5 to 20 mm^2 and from 5 to 60 cm, respectively. They obtained a cross-talk lower than 25 % over a 5 cm long bundle. The fibre bundle loss ranged from 0.12 to 1.92 dB/cm at a wavelength of 10.6 μm. Such high loss is likely to be due to the multiple extrusion processes [12].

A flexible fibre bundle, made from silver halide crystal fibres, was developed by Rave et al. [97]. The fibre bundles had from 30 to 100 individual fibres. The length and the OD of the fibre bundle were 2 m and 1 mm, respectively. The fibre bundles with 36 and 100 elements showed loss of 0.5 dB/cm and 0.7 dB/cm, respectively [97].

Lavi et al. [98] fabricated AgClBr fibre bundles consisting of 100 elements. The fibre bundles had OD between 0.7 and 2 mm. The fibre bundle losses were found to be 2.3 and 9.4 dB/m for the larger and smaller fibre bundles, respectively. While successful transmission of a thermal image of a human hand was demonstrated using a 1 metre long fibre bundle (2 mm OD), the fibre bundle had a low spatial resolution [98].

The same group later reduced the loss of these silver halide fibres down to 0.4 dB/m and 2.3 dB/m at 10.6 μm for 2-3 metres long bundles with 0.7 mm and 2.2 mm OD, respectively [13], but again the bundle had low spatial resolution (100 pixels).

As it is possible to notice from these attempts, silver halide crystalline fibre bundles present limitations such as high losses, short lengths and low spatial resolution. These are probably due to the difficulties in the fabrication method of crystalline fibre bundles. In fact, the multiple extrusion method causes nonuniformities in

the fibre bundle. Moreover, bundles made of silver halide crystal suffer from high inter-core crosstalk due to the low index contrast of the fibres.

3.3.2   Hollow core fibre bundles

Gopal et al. [14] presented a fibre bundle with up to 900 individual fibres, each one coated with Ag/AgI. The bundle was however rigid due to the large required size of each hollow core, and only 2.5 cm in length; it had loss of 9.7 dB/m at a wavelength of 10.6 μm [14].

Gal et al. [99] developed fibre bundles consisting of 675 - 900 capillaries coated with Ag/AgI layers with ODs between 3 and 4 mm. The fibre bundles were 30 cm long. The fibre bundle attenuation was found to be 0.48 dB/cm at 10.6 μm [99].

Matsuura et al. [100] developed a flexible fibre bundle consisting of 127 hollow core fibres coated with silver and cyclic olefine polymer (COP) coating. The fibre bundle was 480 mm long with an OD of 6 mm. The transmission window of this fibre bundle was between 2 and 12 μm wavelength. The fibre loss was approximately 7 dB/m at 10 μm wavelength. Although they performed thermal images at as low temperatures as the human body, the fibre bundle presented low spatial resolution [100].

A longer fibre bundle (90 cm), made of 245 hollow core borosilicate fibres has been also recently developed by Kobayashi et al. [15]. It exhibited a high transmission loss of the order of 14 dB/m between 3 and 4 μm in wavelength. They performed thermal imaging of objects at a temperature of 32 °C through a 30 cm long bundle [15].

As can be seen, also hollow core fibre bundles show limitations in length and number of pixels. In this case, these limitations are due to the difficulties in drawing hollow core fibres. As I will explain in Chapter 6, hollow core fibres need to be pressurised during the fibre drawing to contrast the effect of the surface tension which tends to collapse the hollow fibre.

3.3.3 Chalcogenide fibre bundles

Several chalcogenide fibre bundles have been developed in the past. The use of chalcogenide glass to fabricate a solid core fibre bundle can minimise the aforementioned drawbacks which are present for hollow core and crystalline fibre bundles. This is because solid core fibres are much easier to fabricate compared to hollow core fibres, as I will explain in Chapter 6, and also chalcogenide fibre bundles can be developed using a drawing tower allowing one to fabricate long bundles. Moreover, chalcogenide glass, which has a high refractive index, can be combined with low refractive index materials as polymer in order to have a bundle with high index contrast fibres. This minimises the inter-core crosstalk.

In the 1985, Saito et al. [16] fabricated a 1.3 m long fibre bundle, consisting of 200 AsS core and FEP cladding fibres using the stack and draw approach. This bundle had a 2.2 mm OD and each core was 90 μm in diameter. Although this excellent work presented losses as low as 0.6 dB/m at 3.3 and 4.8 μm, it offered a limited spatial resolution due to the low number of pixels. A few years later, Nishii et al. [17] developed a fibre bundle with a higher spatial resolution using the coil winding method. In particular, this 1 metre long bundle, consisted of 8400 AsS core and Teflon cladding fibres and it was transparent across the wavelength range between 1 and 7 μm. Each core was 65 μm in diameter. The cross section of this fibre bundle was rectangular (5.3 x 7.8 mm) and to make it flexible, only the fibre ends were cemented together. This fibre bundle was efficient for temperatures as low as 25 °C [17]. More recently, in 2015, Zhang et al. [18] obtained fibre bundles with the highest number of pixels for the mid-IR spectral range using the stack and draw technique. In fact, the bundles had 810000 As_2S_3 glass cores and a polyetherimide (PEI) polymer cladding, and each core has a diameter of 9 μm. The obtained fibre bundles were only 5 and 20 cm long and their cross section was of 110 mm^2. The high index contrast between the core and cladding materials enabled a low cross-talk of 2.5 % over a 5 cm long fibre bundle. In order to give mechanical flexibility to an otherwise fairly rigid bundle, they dissolved the PEI polymer in a solvent; this however resulted in increased cross-talk between adjacent fibres [18]. In 2017, Chenard et al. [19] developed a 2 m long fibre bundle made of 4000 As_2S_3 core/cladding fibres using the stack and draw technique. The fibre bundle was 2.2 x 2.2 mm in dimension and each core had a 34 μm diameter. In particular, the fibre bundle had a low NA of 0.3. For this reason they added a buffer

layer around each fibre of Polyethersulfone (PES) polymer to decrease the cross-talk. Their attempt presented some non-uniformities. In the same year, Qi et al. [20] fabricated fibre bundles with high index contrast based on 200000 GeAsSeTe glass cores and PEI polymer cladding. These bundles had an OD of 4 mm and cores with 15 μm diameter. They chose GeAsSeTe glass as the core material to extend the transmission of the fibre bundle to wavelengths where objects at a low temperature, such as the human body, have the maximum IR emission. Although they have obtained a high number of pixels, the high transmission loss of 60 dB/m at 10 μm wavelength only allowed them to perform a thermal image of a human hand through a 5 cm long bundle [20]. Over that length the inter-pixel cross-talk was around 1 %.

Arguably, the closest technology yet reported that would be able to realise flexible low loss bundles is that employing chalcogenide glasses. Table 3.2 reports the main properties of chalcogenide fibre bundles presented above.

While multiple approaches have been proposed, achieving simultaneously good performance in terms of lengths, loss, mechanical flexibility, coherence and inter-core cross-talk is a generally challenging task. For this reason, no commercial mid-IR fibre bundle is available. For example, Zhang et al. [18] and Qi et al. [20] obtained a high spatial resolution, but the bundles were unusable for real applications due to their 20 and 5 cm lengths. Moreover, as shown in the work of Nishii et al. [17], and as mentioned in Chapter 2, the coil winding method limits the reduction of the pixels size; further reduction of the pixel size is useful to make a compact fibre bundle. This can be achieved through the stack and draw technique, where bundles with small chalcogenide glass cores as 9 μm, have been demonstrated. In order to make a mid-IR fibre bundle commercially attractive, it should have the combination of low loss, high number of pixels, low cross-talk, length greater than 1 m, mechanical flexibility and compactness. One of the aims of this work was to combine the good properties of the chalcogenide fibre bundles reported in literature in order to develop a coherent fibre bundle with a broad transmission band in the mid-IR (3-12 μm), which is compact, mechanically flexible and that allows thermal imaging of objects at temperatures down to those of the human body. The bundle was initially optimised to transmit radiation between 3 and 5.5 μm wavelengths. This is compatible with commercial thermal cameras based on cooled InSb detectors, which have the highest sensitivity in this

	Fabrication method	Core/clad material	OD [mm]	Core diameter [μm]	Length [m]	Pixel number	Cross-talk [%]	Loss [dB/m]
Saito et al. [16]	Stack and draw	As_2S_3/FEP	2.2	90	1.3	100	-	0.6 at 3.3 and 4.8 μm
Nishii et al. [17]	Coil winding method	As_2S_3/Teflon	5.3 x 7.8	65	1	8400	-	Not measured
Zhang et al. [18]	Stack and draw	As_2S_3/PEI	11	9	0.05 and 0.2	810000	2.5	Not measured
Chenard et al. [19]	Stack and draw	As_2S_3/As_2S_3	2.2 x 2.2	34	2	4000	-	Not measured
Qi et al. [20]	Stack and draw	GeAsSeTe/PEI	4	15	0.05 and 0.2	200000	1	Not measured

TABLE 3.2: Comparison between mid-IR chalcogenide fibre bundles [16–20].

spectral range [78]. To image bodies at a temperature close to the human body, as shown in Chapter 4, a core glass able to transmit at even longer wavelengths was chosen. This opens up the potential to optimise the bundle for future operation with cheaper microbolometric cameras operating in the 8 - 12 μm spectral range.

3.4 Conclusion

In this chapter, thermal imaging, blackbody radiation and mid-IR transparent materials have been discussed. In addition, the state of the art of fibre bundles transparent in the mid-IR spectral range have been presented. In the following chapter, the choice of the materials and fabrication technique to develop a flexible and coherent mid-IR fibre bundle which is transparent between 3 and 12 μm and with a low cross-talk are reported.

Chapter 4

Fibre bundle fabrication

In this chapter, the fabrication of flexible coherent mid-IR fibre bundles for thermal imaging is reported. The fibre bundle materials choice and characterisation is presented. The fibre bundles consist of 1200 $Ge_{30}As_{13}Se_{32}Te_{25}$ glass cores embedded in a FEP polymer cladding. The high index contrast between the chalcogenide glass and the polymer cladding helps to minimize the inter-pixel cross-talk, while the low Young's modulus of the polymer cladding gives the bundle good flexibility despite its millimitre scale OD. In order to characterise the fibre bundles, their ends have been polished. The polishing technique, which was developed to polish several fibre bundle sections simultaneously, is described.

4.1   Fibre bundle materials

The choice of core and cladding materials plays an important role in the development of a bundle that is mechanically flexible and possesses good thermal imaging properties. The core material must be transparent in the mid-IR spectral region, while for the cladding, low Young's modulus materials like polymers allow improved robustness and flexibility as compared to an all-glass structure. As reported in the works of Zhang et al. [18] and Qi et al. [20] (Chapter 3), a high index contrast between the core and cladding elements in the fibre bundle helps to minimise the cross-talk. Since this project started few years before I joined the group, some choices and experiments were made by a senior member of my group. In particular, the bundle materials were chosen by Dr Joris Lousteau. In

the first part of my PhD, I assisted Dr Joris Lousteau, in order to learn the bundle fabrication process before taking the leadership of the project.

4.1.1   Core material

As mentioned in Chapter 3, chalcogenide glass was considered as the best material to fabricate mid-IR fibre bundles. In this work, for the core material, commercially available Vitron IG3 chalcogenide glass was selected [93] because of its optical transparency between 3 and 12 μm and its high refractive index of 2.81 at 3 μm wavelength (Figure 4.1a). The glass is made of $Ge_{30}As_{13}Se_{32}Te_{25}$ and its properties are listed in Table 4.1.

Glass properties	Vitron IG3
Glass transition temperature [°C]	275
Softening point [°C]	360
Young's Modulus [GPa]	22
Refractive index (n)	2.81
Transmission range [μm]	3 - 12

TABLE 4.1: Vitron IG3 chalcogenide glass properties provided by Vitron [93].

The subscripts in the glass composition represent the concentration of each component in mol%. The Vitron IG3 glass transition temperature and softening point are 275 °C and 360 °C, respectively [93].

To measure the glass loss, my colleague Dr Joris Lousteau and I fabricated an unclad fibre with a diameter of 240 μm, on which I performed a cut-back measurement using a FTIR spectrometer. As a source, I used a Thorlabs SLS202L Stabilized Tungsten light source [101], and the fibre transmission within 2.6 and 5.4 μm was measured with an ARCoptix FT-IR rocket spectrometer [102]. The spectrometer has a MCT detector and it operates in a wavelength range between 2 and 6 μm [102]. The tungsten light source emits an infrared radiation similar to a blackbody at 1900 K and therefore its emission covers the spectral range from 450 to 5400 nm [101] as shown in Figure 4.2.

The input and the output ends of the fibre were connected to the tungsten light source and the ARCoptix FT-IR rocket spectrometer, respectively, by using bare fibre adaptors with FC/PC connectors. 39 transmission spectra were measured by cutting the fibre every 10 cm. To extend the glass loss measurement to longer wavelengths (5.4 - 12 μm) another cut-back measurement using a more conventional
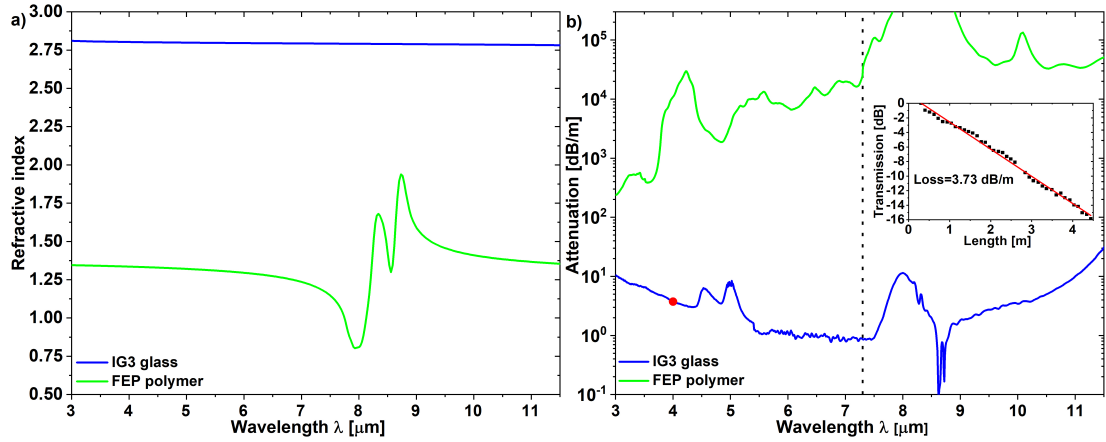
FIGURE 4.1: a) Refractive index of Vitron IG3 chalcogenide glass provided by Vitron [93] blue curve and of the FEP polymer (green curve). b) The blue curve represents Vitron IG3 glass loss measured on an uncladded fibre of 240 μm of diameter between 3 and 5.4 μm wavelength combined with the loss measured on a fibre of 700 μm between 5.4 and 11.5 μm. The inset shows the fibre transmission in dB at 4 μm in wavelength measured at different fibre lengths (cut-back). The green curve represents the FEP polymer loss measured on a sample 0.86 mm thick for wavelengths between 3 and 7.3 μm and on a sample 0.05 mm thick for wavelengths between 7.3 and 11.5 μm.
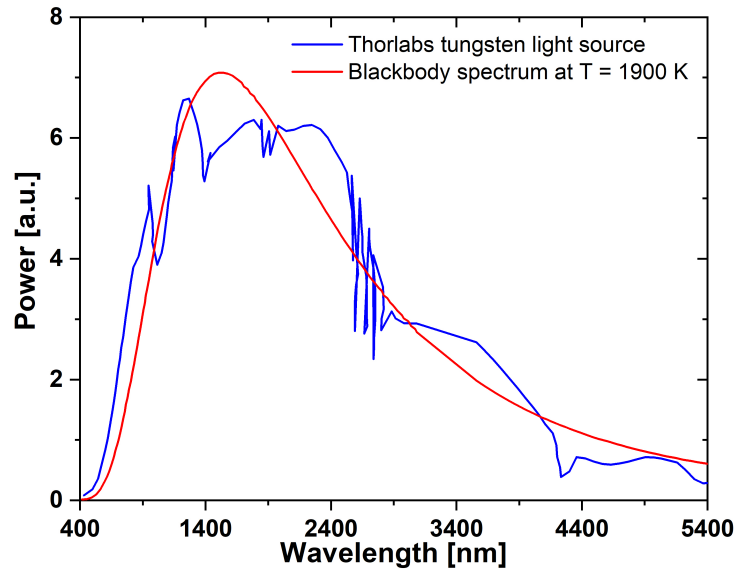
FIGURE 4.2: Spectral response of the Thorlabs SLS202L Stabilized Tungsten Light Source (red curve) compared with spectral radiance of a blackbody at the temperature T = 1900 K (blue curve). Reproduced from [101].

Varian 670 FTIR spectrometer was performed by my colleague Dr Ali Masoudi. To confirm that the loss measurement was not a function of the fibre diameter, a different fibre, made of the same IG3 glass core, but with a FEP polymer cladding was also used. The core diameter was even larger (700 μm), to minimise the fraction of modal power in the cladding. The glass loss measurements of the two different fibre samples were comparable at 5.4 μm (1.59 dB/m for the fibre with 240 μm core diameter and 1.24 dB/m for the fibre with 700 μm core diameter). Figure 4.1b shows the combined measured glass attenuation curve, while the inset shows the cut-back measurement at 4 μm wavelength and its linear fit with a coefficient of determination R^2 of 0.9939. In the 3 - 5 μm wavelength range the IG3 loss is between 3 and 10.4 dB/m. Between 5.5 and 7.5 μm the IG3 glass has loss between 0.84 and 1.25 dB/m. Beyond 11 μm the IG3 loss increases due to the glass multiphonon absorption. The absorption peaks at 4.52 μm and 7.8 μm are attributed to the Se-H bond, while the peak at 4.95 μm is due to the Ge-H bond [94]. Although the background loss of this commercial glass is already fairly high even before it was structured into a fibre bundle, IG3 glass was considered to be adequate for this initial demonstration, knowing that its loss can be reduced by distillation process in future works. For example, distillation of the glass components allows to reduce impurity-based attenuation [103].

4.1.2 Cladding material

As a cladding material, a fluoropolymer with thermally compatible characteristics such that it would be possible to co-draw the two materials (IG3 and polymer) with a rod-in-tube technique, was selected. To select the most suitable cladding material, just before I started my PhD, my colleague Dr Joris Lousteau performed two drawing tests using an IG3 glass rod and both a perfluoroalkoxy (PFA) and a FEP polymer tube. The IG3-FEP and the IG3-PFA combinations were similar in term of drawing stability showing a low diameter fluctuation. However, the commercial PFA polymer tubes have limited range of dimensions compared to the commercial FEP polymer tubes. For this reason, the FEP polymer was selected as a cladding material. For all the works discussed in this thesis, FEP is used; FEP is a known thermoplastic material with a low Young's modulus (600 MPa) [104], and with processing temperatures of 370 °C [105].

Figure 4.1a shows the FEP polymer refractive index measured by Prof. Petr Janicek with a variable angle spectroscopic ellipsometer J. A. Wollam Co IR-VASE,

which covers the spectral range 840-5500 cm^{-1}. Spectra for angle of incidence of 45°, 50°, 55° and 60° were recorded (by measuring 25 scans, 15 spectra per revolution, with wavenumber step of 8 cm^{-1}). At 3 μm wavelength, the FEP's refractive index was measured to be 1.345. The FEP polymer shows a refractive index change between 8 and 8.75 due to a large absorption peak.

To better support the modelling simulations, which I will show in later sections, I also measured the attenuation of the cladding material. I used a Varian 670 FTIR spectrometer on a 0.86 $\pm$ 0.03 mm thick sample. Since the spectrometer was not capable of measuring the transmission of the FEP sample beyond 7.3 μm due to the high material losses, the loss in the 7.3-12 μm wavelength range was measured on a thinner, 0.05 mm sample. The attenuation of the FEP polymer is shown in Figure 4.1b. In the 3-5 μm wavelength range the loss is between $\sim$250 dB/m and $\sim$30000 dB/m. Between 6 and 7 μm the polymer loss is between $\sim$6500 and $\sim$20000 dB/m. In close proximity of the absorption peak between 7.96 and 8.75 μm, the polymer loss is extremely high. Hence, I was unable to measure the FEP transmission spectrum between 7.96 and 8.75 μm. In the 9-11.5 μm wavelength range the FEP loss is between $\sim$33000 and $\sim$160000 dB/m. The absorption peaks at 4.23 and 5.57 μm are attributed to the -CF$_2$ bond and -CF=CF$_2$ double bond, respectively. The stretching vibration of the C-F bond leads to absorption in the 7.1-10 μm wavelength range [106].

Despite the extremely high loss of the FEP polymer cladding, the simulation results indicated that thanks to the high index contrast with the glass and the resulting large fraction of power in the core for the first few modes (greater than 99.8 %), the total bundle loss would still be dominated by the IG3 glass bulk loss. Therefore it was decided to proceed with the fibre bundle fabrication.

4.2   Fibre bundle fabrication

Following the choice of the fibre bundle materials, the stack and draw technique was chose as fabrication method. As mentioned in Chapter 3, through this method allows a bundle can be obtained in a single draw step of stacked fibres and its coherence (i.e. end-to-end pixel spatial matching) during fabrication. Unlike in the layer winding method [61], where handling small fibres is challenging, with stack and draw method the fibre bundle can be fabricated with arbitrary pixel size, the dimension of which can be decided directly during the draw. To minimise the

number of thermal processes and reduce the possibility of glass crystallisation, the fibre bundle was fabricated through the stack and draw method. Figure 2.9 shows the stack and draw technique steps. The potential drawbacks of this fabrication method are the fact that if the fibres are not well stacked together, some pixels can be dislocated in the final fibre bundle. Also, if the OD of the final fibre bundle is too large, it can be limited in term of flexibility. For this reason, in the stack and draw approach, the choice of number of pixels and their dimension is important. Previous fibre bundle fabrication attempts presented some core dislocations probably due to the fact that the stack of fibre was not compact during the consolidation step. In this work, a rod-in-tube preform made by a FEP polymer tube (Figure 2.9a) of 12 and 14 mm of inner diameter (ID) and OD and an IG3 glass rod (Figure 2.9b) of 12 mm in diameter, respectively, was fabricated. From that preform, approximately 170 metres of Vitron IG3 glass core and FEP polymer cladding fibre (Figure 2.9c) of 300 ± 8 μm of diameter were drawn under dried atmosphere at a speed of 2.2 m/min. The resulting fibre was cut in pieces of 12 cm in length and 1200 pieces were stacked together in a hexagonal Poly Methyl Methacrylate (PMMA) mould as shown in Figure 2.9d. The stack was consolidated in a furnace at temperature T=200 °C for 2 hours and then it was inserted in a FEP polymer tube (Figure 2.9e) with 12 mm and 14 mm ID and OD, respectively. Figures 4.3a and b show the consolidated stack of fibres and the consolidated stack inserted into the FEP polymer tube, respectively.
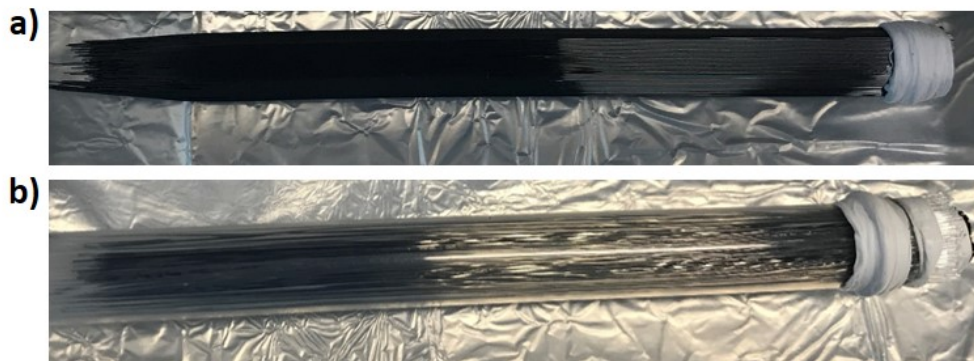
FIGURE 4.3: a) Consolidated stack of IG3-FEP fibres. b) Consolidated stack inserted into a FEP polymer tube.

In the last step, the final preform was placed into the drawing tower furnace under dried atmosphere and then it was drawn into the desired bundle. From the same preform, by changing the drawing speed, two different fibre bundles of 1.1 mm (v_f = 160 mm/min) and 0.675 mm (v_f = 430 mm/min) diameter, each with 1200

fibres were obtained. The overall length of bundles obtained was of ∼4.2 m. This is a reasonable usable length considering that the maximum yield of the bundle is ∼9 m and that part of this length represents the transition between different drawing speeds (so, it has diameter variation along the length). This is a good result considering that the drawable part of the preform is only ∼6 cm because ∼3 cm are needed for the neck down and ∼3 cm are used to hold the preform in the drawing tower. The fibre bundles of 1.1 and 0.675 mm of diameter had cores of 22 and 13 μm in diameter, respectively. These core diameters were chosen to be ∼3 - 8 times the wavelength in order to have a high V-number and then a strong confinement of the modes in the core, aiming to transmit the blackbody radiation in the 3 - 5 μm wavelength range. The obtained fibre bundles showed excellent mechanical flexibility. Figure 4.4 shows that despite its OD of 1.1 mm, even the larger of the two bundles is mechanically flexible, which would certainly not have been possible if Dr Joris Lousteau had chosen a second glass as cladding. For example, Vitron IG3 chalcogenide glass has a Young's modulus of 22 GPa [93] which is much higher than the polymer (600 MPa).
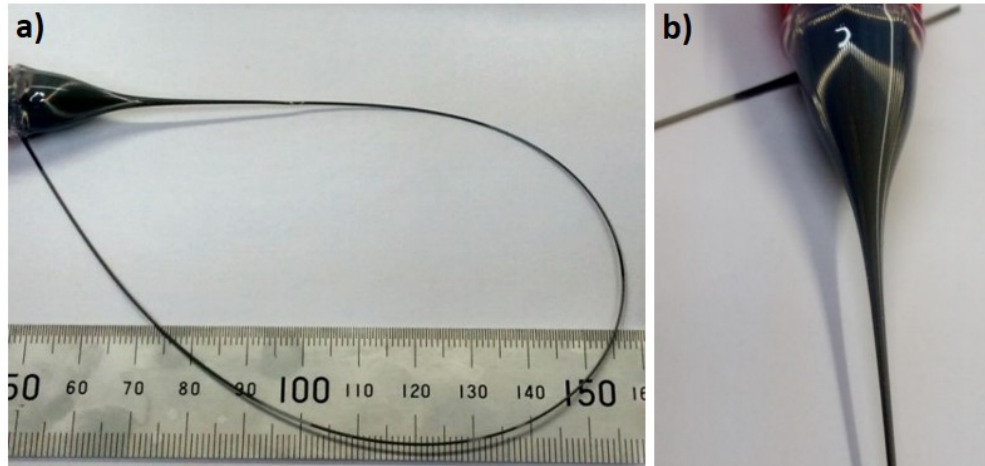
FIGURE 4.4: Flexibility of the larger fibre bundle with an OD of 1.1 mm.

In order to test and characterise the fibre bundles, both of them need to be polished. For this, I have had to develop empirically a recipe.

4.3 Fibre bundle polishing

Both ends of each fibre bundle were polished using a Logitech PM5 polishing machine. The process consists of 2 different steps called lapping and polishing.

Following preliminary tries, where I embedded few bundles inside a hollow stainless steel cylinder with an epoxy (Loctite ecobond F123) (see Figure 4.5) and I noticed that this epoxy was not soluble in either acetone and isopropanol, I decided to design a dedicated mould that could embed several bundles in a polymer and acrylic matrix so that they could be polished simultaneously (up to 14 of them).
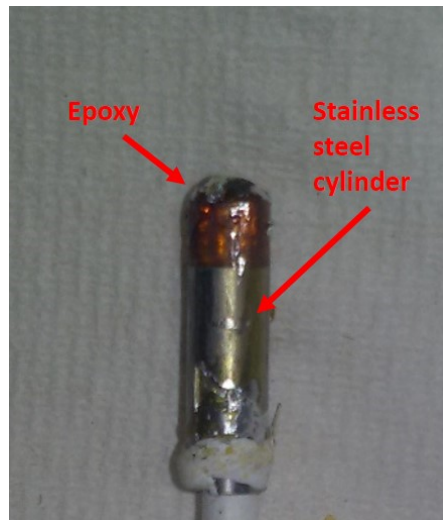
FIGURE 4.5: Fibre bundles embedded inside a hollow stainless steel cylinder with an epoxy.

This led to a reduction of the polishing time. The polymer/acrylic matrix was soluble in acetone. A metal holder, which I designed, was realised in the workshop at the University of Southampton. Two specular stainless steel blocks with an indent in the centre of one edge are placed on a third block of the same material (Figure 4.6a). When the first two blocks are placed next to each other they make a cylindrical hole. Additionally, a cylinder made of PMMA polymer was realised in the workshop of the University of Southampton with the same OD of the holder hole. The cylinder has 14 holes to accommodate the fibre bundles ends (Figure 4.6b). Each bundle was bent and both ends were inserted in the PMMA holes. In this way, both bundle ends are polished at the same time and with the same polishing quality. Through this, the fibre bundle is kept straight and then a flat bundle end surface can be obtained. Since the fibre bundle and the holes of the PMMA cylinder have a size mismatch, I used a VLST acrylic (Kemet) to fill the gaps. It was prepared by mixing gently the liquid hardener and the resin powder in a ratio 2:5. The cylindrical hole between the stainless steel was sprayed with a silicone spray and the acrylic was poured inside the hole. Then, I inserted the PMMA cylinder that contains the bundles inside the stainless steel holder hole.

The final result is shown in Figure 4.6c. In this way, the bundles can be moulded with the acrylic. Once the VLST acrylic had hardened (3 hours), the stainless steel blocks were separated and the bundles were ready to be polished (Figure 4.6d). Then, the embedded bundles with the PMMA/acrylic matrix was inserted in the Jig for polishing. The whole assembly was polished using the empirical recipe I developed and which is detailed in the following section. The first step is that of lapping.
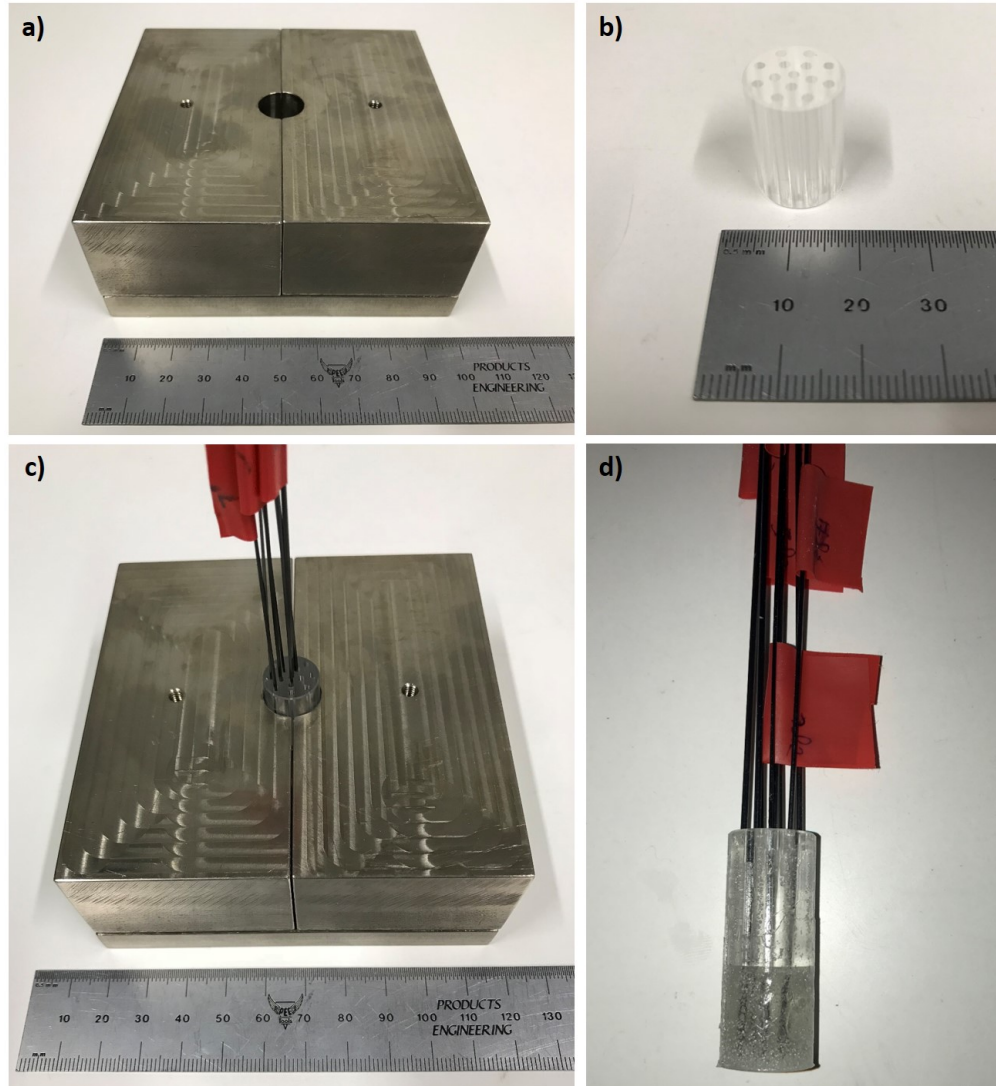
FIGURE 4.6: a) Metal holder to mould the fibre bundles for polishing, b) PMMA cylinder with 14 holes, c) fibre bundle moulding in VLST acrylic by using the metal holder and d) fibre bundles moulded in VLST acrylic.

4.3.1 Lapping

The Logitech PM5 machine was used to perform the bundle lapping. Deionised water/Al_2O_3 powder solutions with different grain sizes of Al_2O_3 powder were used: 9, 3, 1 and 0.25 μm, respectively. Before starting, the plate was wet with deionised water. As the first step, I placed the Jig with the embedded bundles on the cast iron plate. Then, a drop per second of a solution of 9 μm of Al_2O_3 powder was poured onto the cast iron plate. The speed of the cast iron plate was increased slowly up to 35 rpm. Then, after the removal of 100-220 μm of material, the bundle surfaces were free of scratches. The grain size was decreased until the bundles surfaces were shiny and without scratches. After the last step (0.25 μm of Al_2O_3 powder) I changed the cast iron plate with a soft cloth plate to do the polishing step.

4.3.2 Polishing

The polishing step was performed by using the 0.25 μm grain size solution for 20 minutes. At the end of the process, the bundles surfaces appeared flat, shiny and free of scratches. The embedded fibre bundles in the acrylic/polymer matrix were inserted in an acetone bath in order to dissolve the VLST acrylic and the PMMA polymer. Previous attempts performed by me presented scratches and some residues, probably due to the polymer/acrylic matrix, on the bundle surface as shown in the micrographs in Figures 4.7a and 4.7b which I performed by using the Nikon Eclipse 3 x 2 microscope.

Following several optimisations of the polishing process, I have been able to obtain an excellent polishing quality as shown in Figures 4.8a and 4.8b which show the micrographs of the polished bundles of 22 μm and 13 μm of core diameter by using the Nikon Eclipse 3 x 2 microscope. Despite the different rheologies of the fibre bundles materials, the overall structure was maintained during the fabrication process. This indicated that the co-drawing process was well controlled. In a future work, increasing the number of pixels using a higher fibre density will help to minimise these defects.
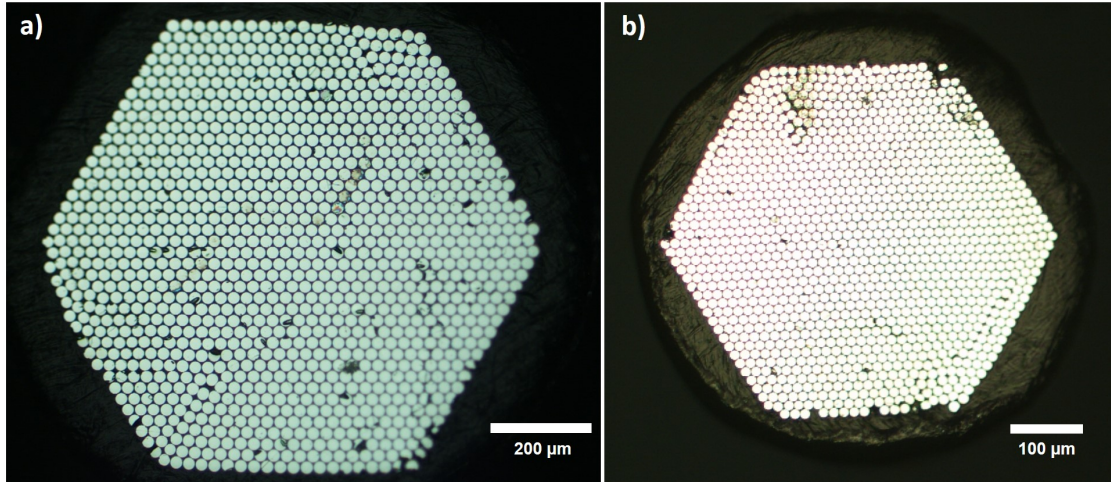
FIGURE 4.7: Micrographs of polished Vitron IG3 glass core and FEP polymer cladding fibre bundle with OD and core diameter of (a) 1.1 mm and 22 μm and (b) 0.675 mm and 13 μm. Both bundles presents scratches and residues on their surfaces.
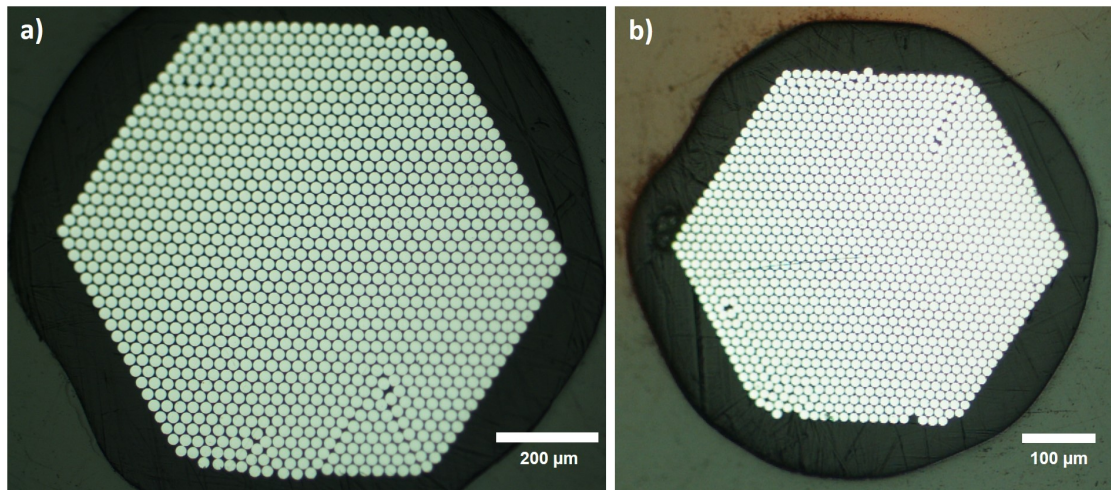
FIGURE 4.8: Micrographs of a polished Vitron IG3 glass core and FEP polymer cladding fibre bundle with OD and core diameter of (a) 1.1 mm and 22 μm and (b) 0.675 mm and 13 μm.

4.4 Conclusion

In this chapter, the fabrication of two coherent mid-IR fibre bundles made of 1200 chalcogenide core and fluoro-polymer fibres using the stack and draw technique was presented. The fibre bundles had an OD of 1.1 mm and 0.675 mm, resulting in pixel sizes of 22 and 13 μm, respectively. Despite the relatively large diameters of the bundles and the use of a fairly fragile glass, they were flexible thanks to the FEP polymer coating which has a low Young modulus. In order to characterise the fibre bundles, the bundle ends had to be polished. In this chapter, I also reported

the development of a recipe to polish the multiple fibre bundle ends.

In the next chapter, the characterisation of the fabricated bundles in terms of loss, thermal imaging and inter-core cross-talk perfomance is presented. In addition to this, a modelling study to extend the fibre bundle efficiency for long wavelength region between 9-11.5 μm, where cheap and simple thermal cameras operate, is presented.

Chapter 5

Fibre bundle characterisation and modelling

Following the fibre bundle fabrication and polishing reported in Chapter 4, in this chapter, the fibre bundles' characterisation, is presented. The attenuation of the fibre bundles was measured by using FTIR spectrometer, with the cut-back method. The fibre bundle imaging performance was tested by using a thermal camera. The capability to produce high contrast and high spatial resolution thermal images of a human hand indicates its excellent imaging potential. Inter-core cross-talk, which leads to image deterioration and blurring, was then evaluated. Also, I performed a modelling study to investigate the change in fraction of power in the core and in the cladding for different core diameters. Finally, I present a modelling study to make the fibre bundle transparent at wavelengths where low-cost thermal cameras operate.

5.1   Fibre bundle attenuation

To assess the fibre bundle imaging performance, it is essential to characterise its loss in the spectral range of interest. In this work, I was mainly interested in the spectral region between 3.6 and 4.9 μm where the InSb thermal camera available for this project operates (see Section 5.2). Measuring a fibre bundle loss is a cumbersome procedure that has not been often undertaken in similar studies. Here, I carried out the loss measurement by using the ARCoptix mid-IR FTIR [102], which has a MCT detector, with the cut-back technique. A Thorlabs SLS202L

tungsten light source (SLS202L) was used as infrared source [101]. The Thorlabs light source and the ARCoptix mid-IR FTIR were connected to the output and to the input of the fibre bundle, respectively, by using FC/PC connectors. Then, the fibre bundle transmission was measured. Then, the bundle was shortened by 20 cm and, its end was re-polished and the fibre bundle transmission was re-measured. This operation was repeated four times, giving me the possibility to infer the fibre bundle attenuation. In order to look at the reproducibility of the fibre bundle attenuation measurement, groups of bundles with the same core diameter were investigated; in the present work I compared the attenuation of two fibre bundles with 22 μm core diameter (labelled bundle 1 and bundle 2 in Table 5.1) and two fibre bundles with 13 μm core diameter (labelled bundle 3 and bundle 4 in Table 5.1).

Fibre bundle label	Core diameter [μm]	Fibre bundle length [cm]
1	22	123.5
2	22	100.5
3	13	101
4	13	95

TABLE 5.1: The fibre bundle label and its corresponding diameter and initial length.

The attenuation of both fibre bundles is plotted in Figures 5.1a and b.
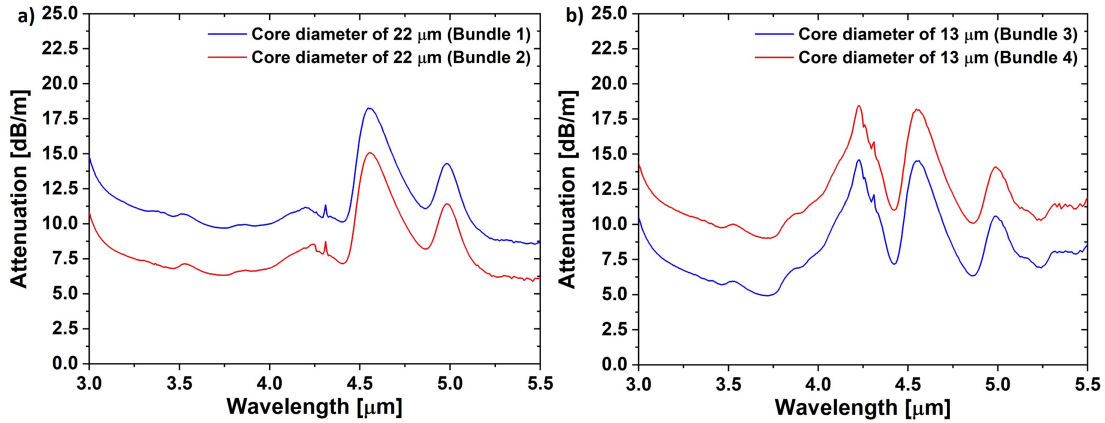
FIGURE 5.1: a) Attenuation of fibre bundle 1 (blue curve) and fibre bundle 2 (red curve) with 22 μm core diameter, b) Attenuation of fibre bundle 3 (blue curve) and fibre bundle 4 (red curve) with 13 μm core diameter.

As shown in these figures, the attenuation of fibre bundles with equal core diameter are not the same. This loss difference is likely due to an error introduced in the loss measurements. In particular, this error was estimated to be $\pm$ 2 dB/m. The most likely explanation for this measurement uncertainty is the presence of residual

scattering from imperfectly polished bundle ends. Also, the coupling efficiency between the input of the fibre bundle and the tungsten light source and between the output of the fibre bundle and the FTIR spectrometer, gives a non-negligible contribution to this error.

In order to evaluate the fibre bundle attenuations, I calculated a FTIR spectrum by averaging spectra of bundles with the same core diameters. Figure 5.2 shows the average attenuations of the fibre bundles of 13 and 22 μm of core diameter and the Vitron IG3 glass loss.
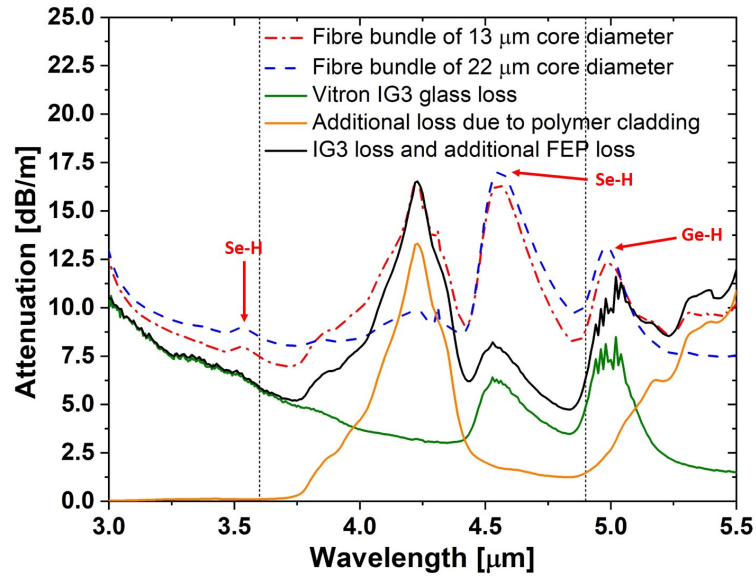
FIGURE 5.2: Average attenuation of fibre bundles with 22 μm (dashed curve) and 13 μm (dashed-dotted curve) core diameters and attenuation of Vitron IG3 chalcogenide glass (green curve). The orange curve represents the additional loss due to the polymer cladding. The black curve represents the expected fibre bundle loss.

From Figure 5.2 it is noticeable that the attenuation of the two fibre bundles are generally comparable although some notable differences can be observed. The attenuation of the 22 μm core diameter bundle is between 8 and 12 dB/m in the wavelength range from 3 to 4.5 μm. For the same wavelength range, the attenuation of the fibre bundle of 13 μm core diameter is between 7.5 and 17 dB/m. Both fibre bundles have two absorption peaks at 3.53 and 4.52 μm due to the Se-H bonds. The absorption peak at 4.95 μm is due to the Ge-H bonds of the Vitron IG3 glass [94]. The curves also show an additional peak at 4.23 μm, which is not visible in the glass loss curve shown in green. This is due to the -CF$_2$ bond in the FEP polymer [106] (see Figure 4.1b). Due to light absorption in the very lossy FEP polymer cladding, the loss of both bundles is higher than that of the bulk

glass. Since reducing the core diameter and increasing the wavelength increases the fraction of power guided in the lossy cladding, this peak is more accentuated in the smaller fibre bundle with 13 μm core diameter. For both fibre bundles the loss differential with the bulk glass increases with the wavelength. The losses of the 13 μm fibre bundle are lower than that of the 22 μm bundle at some wavelengths (between 3 and 3.6 μm, and also between 4.5 and 5.2 μm), possibly due to the measurements errors I have mentioned above. To understand the origin of the various loss contributions, I have attempted to estimate the fraction of loss arising from absorption in the polymer cladding. Here I focus on the fibre bundle with 13 μm diameter cores, for simplicity. In short, first I estimated the fraction of power in the cladding seen by an average ensemble of modes excited in the experiment, using the method explained in Section 5.4.3. From this, I calculated the expected additional loss caused by the FEP polymer, shown by the orange curve in Figure 5.2. By adding this amount to the glass bulk loss (green curve), I obtained the expected fibre bundle loss shown by the black curve. The measured and calculated loss are identical at the polymer loss peak of 4.23 μm, where I fitted my data, but also agree well in the 5-5.5 μm wavelength range. The difference between the measured and calculated loss in the 3-4 μm spectral range is attributed to some scattering at the core/clad interface. At 4.52 μm, in correspondence with the Se-H bond absorption, I see the maximum discrepancy, which likely indicates that additional Se-H bonds have been formed during fibre drawing. While these overall values of loss are still fairly high (generally better than some other reported works [14, 15] but worse than other [16]), they are still low enough for the delivery of thermal images through a metre long fibre bundle.

5.2 Thermal imaging

Next, I performed a qualitative assessment of the thermal imaging properties of the polished fibre bundles, using a Xenics Onca MWIR 320 thermal camera consisting of a cooled InSb detector (1-5.5 μm). The thermal camera, which has a spatial resolution of 320 x 256 pixels, operates between 3.6 and 4.9 μm due to the presence of a spectral filter. This filter, which is positioned inside the thermal camera, reduces the noise of the InSb detector [107]. Its transmission spectrum is shown in Figure 5.3a [108].
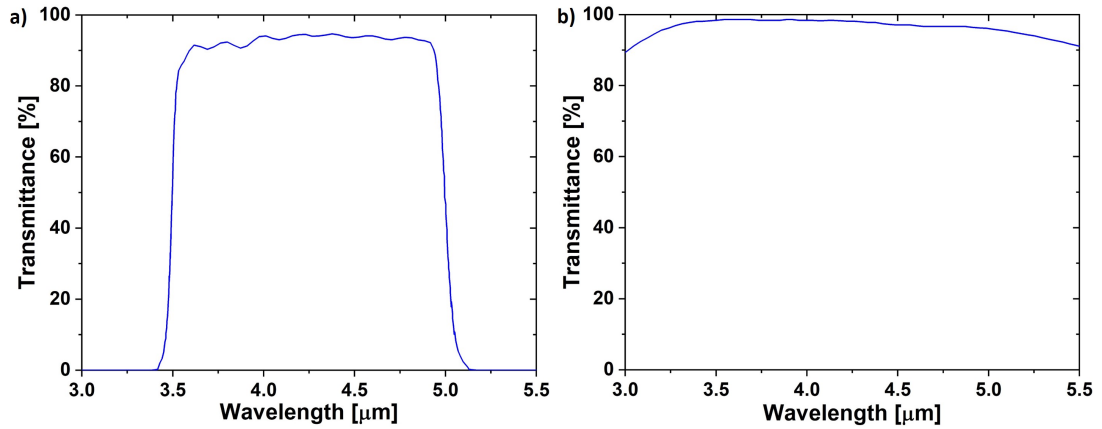
FIGURE 5.3: a) Transmission spectrum wavelength filter [108]. b) Transmission spectrum Asio Microscopic objective lens [109].

The Asio Microscopic Objective camera lens with a magnification of 1 X, was used to perform thermal imaging [109]. This lens has a focal length equal to 50 mm and allows close inspection of small components and its transmission spectrum is displayed in Figure 5.3b.

A square ceramic heating element of 20 X 20 mm in dimension, shown in the inset of Figure 5.7a, was used as an infrared radiation emitter. A fibre bundle with a core diameter of 22 μm and length of 1.15 m was used to transmit the infrared radiation emitted by the ceramic heating element. Two Thorlabs chalcogenide lenses, made of Sb, Ge, and Se (Black Diamond-2), were used [110]. The transmission spectrum of the Black Diamond-2 lens is shown in Figure 5.4a.
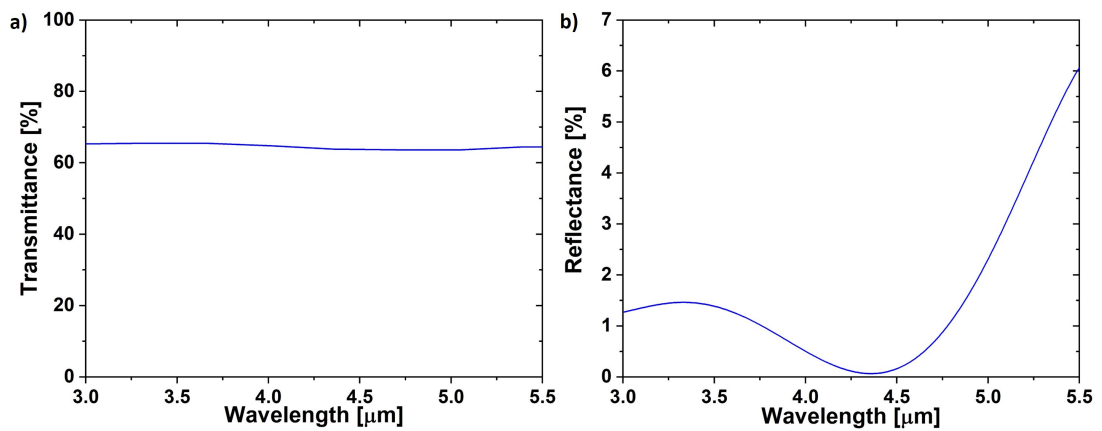
FIGURE 5.4: a) Transmission spectrum of Black Diamond-2 glass measured on a sample 5 mm thick and b) antireflection coating between 3 and 5 μm wavelength on the Black Diamond-2 lens [110].

These chalcogenide lenses have an antireflection coating between 3 and 5 μm in wavelength [110], as shown in Figure 5.4b. The first lens, with a numerical aperture and focal length of 0.86 and 1.873 mm, respectively, was used to focus the ceramic heating element onto the input surface of the fibre bundle. The second lens with a numerical aperture and focal length of 0.56 and 4 mm, respectively, was used to focus the image from the output surface of the fibre bundle onto the detector of the thermal camera (7.68 X 9.6 mm). The reason for using a lens with a larger numerical aperture at the input of the bundle was to collect more infrared light emitted from an object. A schematic of the thermal imaging experiment is shown in Figure 5.5.
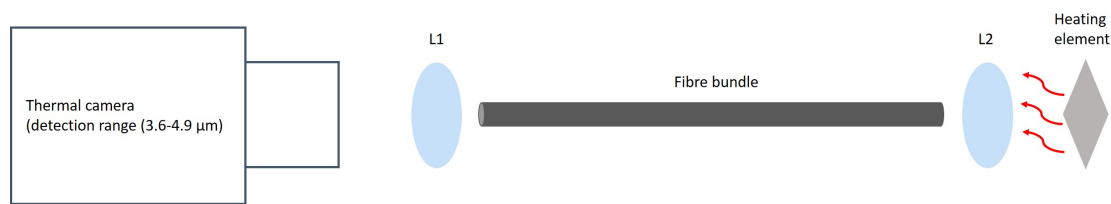
FIGURE 5.5: Schematic of the experimental setup for thermal imaging.

The picture of the experimental setup for thermal imaging is shown in Figure 5.6.
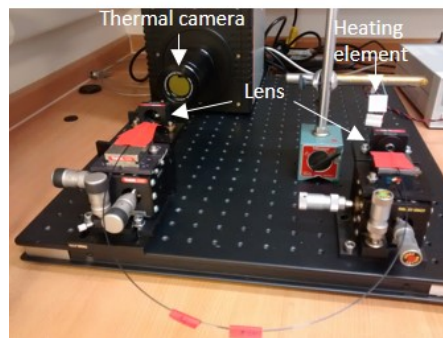
FIGURE 5.6: Experimental setup for thermal imaging assessment through a 1.15 m long fibre bundle by using a heating element as infrared source and a thermal camera to detect the infrared radiation.

5.2.1 High temperature object imaging

The temperature of the heating element was calibrated using a resistive temperature sensor placed onto its surface. Thermal images of the ceramic heating element at temperatures equal to 115 and 80 °C were transmitted through 1.15 m of the

largest bundle (1.1 mm OD) to the thermal camera. The bundle was arranged to form a 'u' shape, with a radius of curvature of 15 cm, to test its performance in presence of bending. These images are shown in Figures 5.7a and b, respectively, showing that the contours of the ceramic heating element at 115 °C are sharp and well defined.
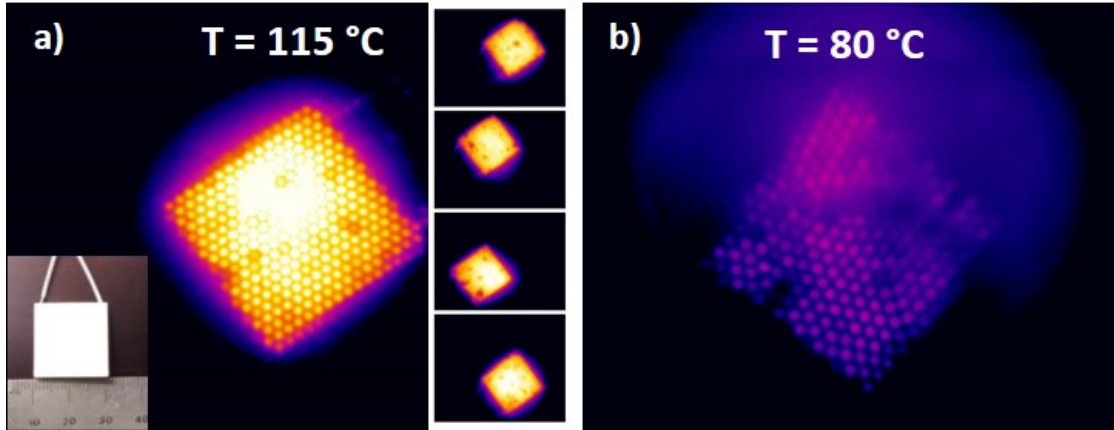
FIGURE 5.7: Thermal image of a ceramic heating element at temperature (a) T=115 °C and (b) T=80 °C, through a fibre bundle 1.15 m long (1.1 mm OD) performed by using the Xenics Onca MWIR 320 thermal camera. The insets of (a) shows a sequence of thermal images of the heating element, produced by changing the position of the input of the fibre bundle through the translation stage.

It is clear that all pixels apart from few scattered ones transmit the same amount of light and therefore appear at a very similar temperature. On the bottom right of Figure 5.7a a sequence of thermal images are displayed of the heating element at 115 °C, which I produced by changing the position of the input of the fibre bundle through the translation stage. Again, sharp edges can be seen. At lower temperatures, thermal imaging becomes more problematic because, due to the fibre bundle loss, an insufficient amount of radiation hits the detector. In fact, for a heating element at T=80 °C (and the same 1.15 m of bundle), the image is less sharp (Figure 5.7b).

5.2.2 Low temperature object imaging

To prove that lower temperature objects can be still imaged if one reduces the bundle length (and thus its loss), I shortened the bundle to 62.5 cm and recorded thermal images of a human hand, as shown in Figure 5.8.
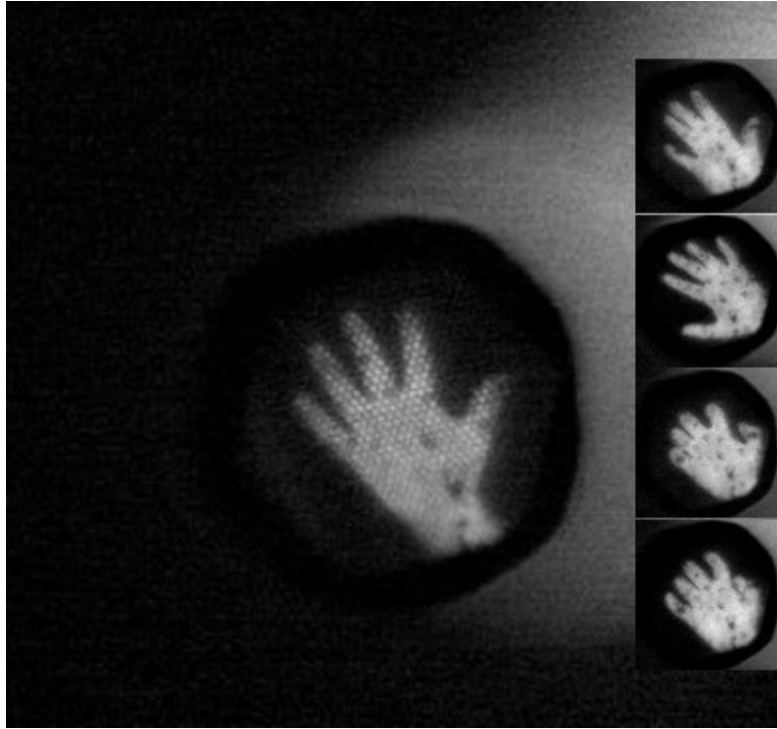
FIGURE 5.8: Thermal image of a human hand through a fibre bundle 62.5 cm long (1.1 mm OD) performed by using the Xenics Onca MWIR 320 thermal camera. The insets show a sequence of thermal images obtained by moving the hand.

As can be seen, the hand is clearly visible and all the fingers clearly distinguishable. Also in this case, the pixels are almost at the same temperature. The inset of Figure 5.8 shows a sequence of thermal images obtained by moving the hand. The thermal images of Figures 5.7 and 5.8 have been both acquired using an integration time of 1.2 ms. Since colder objects, such as the human body, are at a temperature closer to the room temperature, the thermal images appear noisier. To obtain a sharper image of the hand I applied a background subtraction. Figures 5.7 and 5.8 provide a proof of the full coherence of the fabricated fibre bundle.

5.3   Inter-core cross-talk evaluation

The sharp contours in the thermal images above already indicate that over these lengths the inter-pixel cross-talk in the fibre bundle is low. A further qualitative experiment was performed by me using a metal plate with inscribed letters. This was placed between the input of the 62.5 cm long fibre bundle and the ceramic heating element at 115 °C, to evaluate the presence and the effect of cross-talk.

Figure 5.9 shows that the image propagating through the fibre bundle and reaching the thermal camera has sharp contours, with no evident inter-core cross-talk.
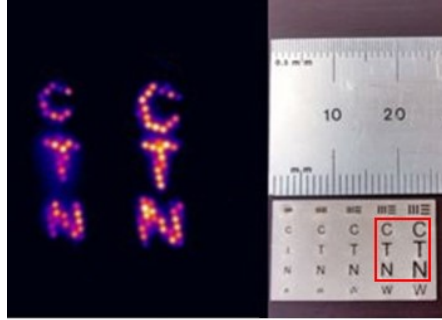
FIGURE 5.9: Thermal image through a fibre bundle 62.5 cm long (1.1 mm OD) by placing a metal target with inscribed letters between the input of the fibre bundle and the ceramic heating element at temperature T=115 °C.

I attribute this excellent performance to the initial choice of a high index contrast between the Vitron IG3 glass core and the FEP polymer cladding, which helps to confine the power inside each pixel. Some beneficial contribution might also be played by the high cladding loss, which severely attenuates the highest order modes in each pixel that would otherwise be the main source of cross-talk. Such an imaging performance would not be possible with fibre bundles with a lower numerical aperture such as those fabricated, for example, using silver halide crystalline fibres or all glass AsS core-AsS cladding fibres. In order to estimate the cross-talk more quantitatively, I excited a single pixel of the 62.5 cm long fibre bundle using a mid-IR incandescent lamp. An iris was used to block the infrared radiation outside a small spot and prevent it from reaching pixels other than a randomly selected one in isolation, or the same pixel with its 6 surrounding neighbours (inset of Figure 5.10). From the images I extracted cross-sectional intensity profiles along selected direction, as shown in Figure 5.10. The green curve and the blue curve represent the intensity profile when a single pixel and when 7 pixels are excited, respectively.

From this graph it is clear that when the light is focused in a single pixel the level of cross-talk into the adjacent cores is extremely low. I used the 7 pixel trace to identify the position of the neighbouring pixels (1st and 2nd pixels), which were then used to calculate the cross-talk. The cross-talk was calculated on the single pixel excitation curve (green) as the ratio between the integrated cross-sectional intensity of one surrounding core to the integrated cross-sectional intensity for the excited core. In order to obtain a more reliable measurement, I averaged the
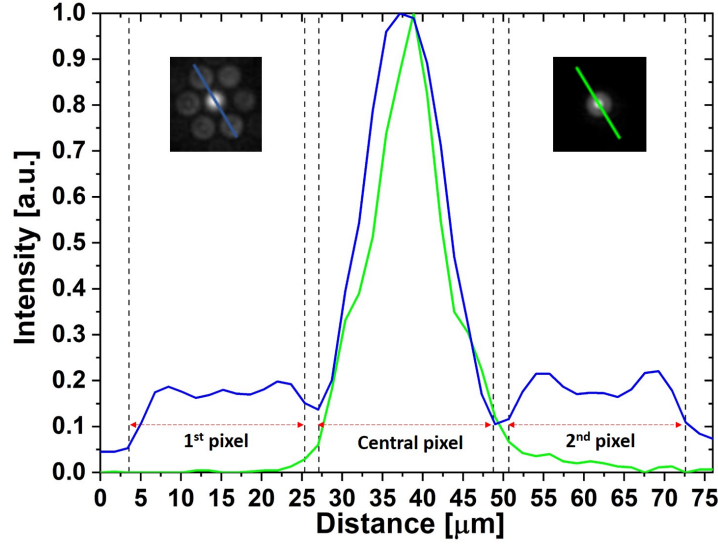
FIGURE 5.10: Intensity distribution at the output of the fibre bundle 62.5 cm long (1.1 mm OD) by exciting several cores (blue curve) and a single core (green curve). Inset shows perpendicular cut of single pixel excited fibre (right upper corner - green) and excitation of single pixel with 6 nearest neighbours (left upper corner - blue).

cross-talks obtained for the 1st and 2nd pixel. Since the cross-talk measurement was performed on a 62.5 cm long bundle, I scaled the cross-talk measurement for a metre long bundle considering that the inter-core cross-talk increases proportionally with the bundle length due to the high numerical aperture. The measured cross-talk was estimated to be around -13.7 dB.

5.4 Modelling study

Following the characterisation of the fibre bundles, I performed a modelling study in the 3-5 μm wavelength range where the fibre bundles transmit. Since in this spectral range infrared cameras are expensive, I also performed a modelling optimisation study to shift the operational wavelength of the fibre bundle to longer wavelengths (10-11.5 μm) where less expensive microbolometer cameras operate.

5.4.1 Loss study in the short wavelength region (3-5 μm)

As shown in the fibre bundle loss measurements, the core diameter is critical for the performance of the fibre bundle. In order to investigate the effect of the core

diameter on the fibre bundle loss between 3 and 5 μm in wavelength, I performed a modelling study by changing the core diameter. Due to the high NA of the fibres employed in the fibre bundle, the fibres are highly multimoded. Since it is difficult to simulate the fibre bundle loss due to the presence of an ensemble of several modes, only the fundamental mode has been studied here. In particular, I simulated the fraction of modal power in the core and the loss of the fundamental mode for different core diameters. In Section 5.4.3 I propose a way to extend the results to many guided modes.

5.4.1.1 Fraction of modal power in the core and in the cladding

As already explained, to minimise the cross-talk between cores in the fibre bundle and to confine the infrared radiation in the core of each pixel of the fibre bundle, the fibre bundle materials were properly chosen in order to get a high refractive index contrast. Since the cladding material is very lossy in the mid-IR, a good confinement of the infrared radiation in the core helps to decrease the overall fibre bundle loss. The fraction of power in the cladding and in the core has been simulated in Comsol between 3 and 5 μm for different core diameters of 13, 22, 40, 80 and 100 μm. The simulation results are shown in Figures 5.11a and b. It is possible to notice that the fraction of power in the cladding increases as the core diameter decreases and as the wavelength increases. In contrast, the fraction of power in the core decreases as the core diameter increases and as the wavelength increases. For a core diameter of 13 μm, the fraction of power of the fundamental mode in the core is higher than 99.955 % at 5 μm wavelength. A core diameter of 22 μm has a fraction of power in the core higher than 99.99 % between 3 and 5 μm.

5.4.1.2 Fundamental mode loss vs wavelength for different core diameters

The transmission loss of the fundamental mode of an IG3 glass core and FEP polymer cladding fibre was simulated in Comsol between 3 and 5 μm wavelength for the same selected core diameters of 13, 22, 40, 80 and 100 μm. The motivation of this study was to understand the effect of the core diameter on the fibre loss because of the high cladding polymer loss and because of the strong polymer absorption peak at 4.23 μm peak due to the -CF$_2$ bond. Figure 5.12 shows the
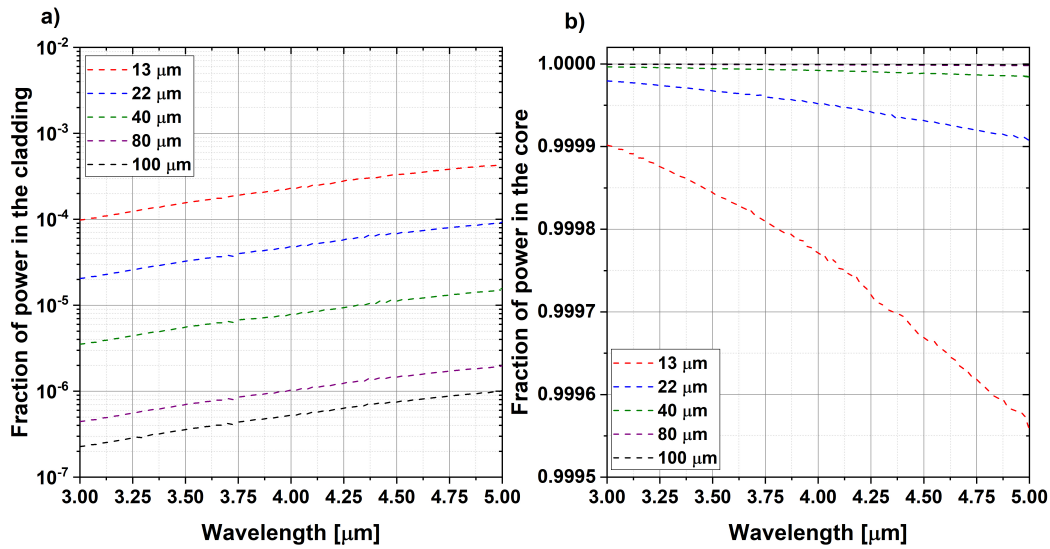
FIGURE 5.11: a) Fraction of power in the cladding of the fundamental mode and b) fraction of power in the core of the fundamental mode for core diameter of 13 (red curve), 22 (blue curve), 40 (green curve), 80 (purple curve) and 100 μm (black curve).

simulated loss of the fundamental mode for core diameters of 13, 22, 40, 80 and 100 μm, as well as the Vitron IG3 glass loss.
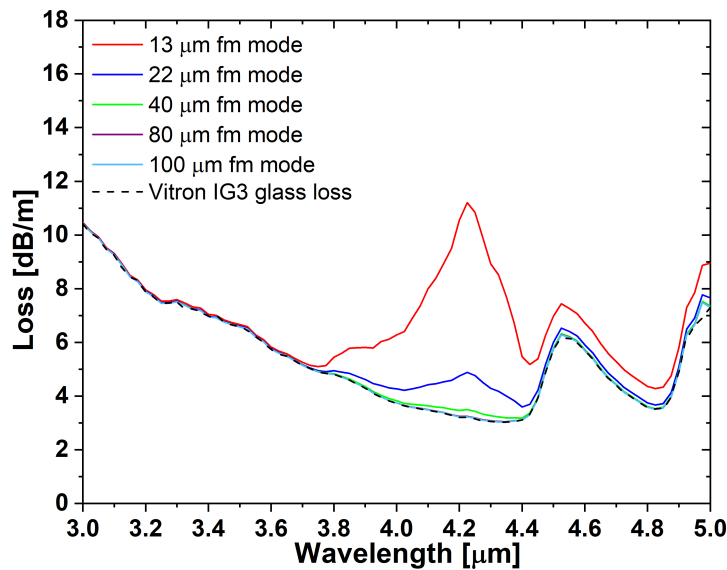
FIGURE 5.12: Simulated attenuation for the fundamental mode for core diameters of 13 (solid red curve), 22 (solid blue curve), 40 (solid green curve), 80 (solid purple curve) and 100 μm (solid light blue curve). The dashed black curve represents the IG3 glass loss.

As can be seen, for a fibre with a core diameter of 13 μm, despite the low fraction

of power in the cladding, the fundamental mode loss presents a strong absorption peak at 4.23 μm. This peak is smaller for a fibre with a core diameter of 22 μm. Fibres with cores of 40, 80 and 100 μm in diameter have the fundamental mode losses which are close to the Vitron IG3 glass loss. This indicates that decreasing fraction of power in the cladding, allows one to obtain a fibre loss close to the core material loss. Since the FEP polymer cladding has high transmission loss, it would be better to increase the core diameter in order to minimise the amount of power in the cladding. Also in the fibre bundle loss measurement, the fibre bundle with smaller core diameter (13 μm) shows a higher absorption peak at 4.23 μm than the fibre bundle of 22 μm of core diameter. This confirms that also a small amount of fraction of power in the cladding makes the difference in presence of very high cladding loss as at 4.23 μm. Since the fibres of the bundle are highly multimode, it is difficult to predict the fibre bundle loss due to an ensemble of propagation modes by using Comsol. In fact, in order to estimate the fibre bundle loss due to the combination of several optical modes, I used the method detailed in Section 5.4.3.

5.4.2 Loss study in the long wavelength region (9-11.5 μm)

Having fabricated a bundle for operation with a 3-5 μm cooled-sensor camera, I conducted a modelling exercise to understand how such a bundle would need to scale in order to operate in the 9-11.5 μm region, where less expensive microbolometric thermal cameras operate. In particular, I studied the fraction of power in the core and in the cladding, and the fundamental mode loss.

5.4.2.1 Fraction of modal power in the core

The fraction of power in the cladding and in the core has been simulated for core diameters of 13, 22, 40, 80 and 100 μm between 9 and 11.5 μm wavelength (Figures 5.13a and b).

As it is possible to see, fibres with a core larger than 40 μm have a fraction of power in the core larger than 99.96 %. Since the polymer loss in the 9-11.5 μm wavelength range are higher than the 3-5 μm spectral range, it would seem preferable to use fibres with a core larger than 40 μm in diameter.
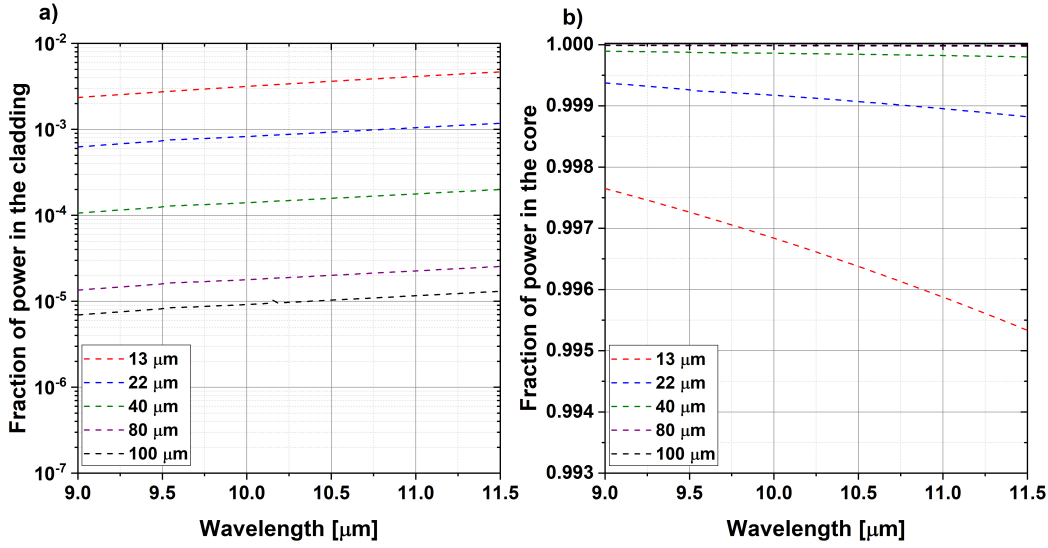
FIGURE 5.13: a) Fraction of power in the cladding of the fundamental mode and b) fraction of power in the core of the fundamental mode for core diameter of 13 (red curve), 22 (blue curve), 40 (green curve), 80 (purple curve) and 100 μm (black curve).

5.4.2.2 Fundamental mode loss vs wavelength for different core diameters

The fundamental mode loss has been simulated for cores diameter of 13, 22, 40, 80 and 100 μm between 10 and 11.5 μm wavelength (Figure 5.14). The graph shows that fibres with core diameter of 13 and 22 μm, have extremely high fundamental mode loss. Instead, fibres with core diameters larger than 80 μm have fundamental mode loss close to the Vitron IG3 glass loss.

5.4.3 Bundle design consideration for 9-11.5 μm wavelength operation

Since the fibres used in the fibre bundle are multimoded, I used the following method to calculate the fibre loss due to an ensemble of optical modes. In particular, here I highlight a procedure to estimate the overlap of a single mode or an ensemble of modes with the cladding of each individual pixel, which can then be used to predict how the performance of this family of bundles scales with wavelength and pixel size. As an illustrative example, I use the 13 μm pixel fibre bundle discussed above. I start by determining from experimental measurements the fraction of power in the cladding (ηClad) that would be responsible for the measured
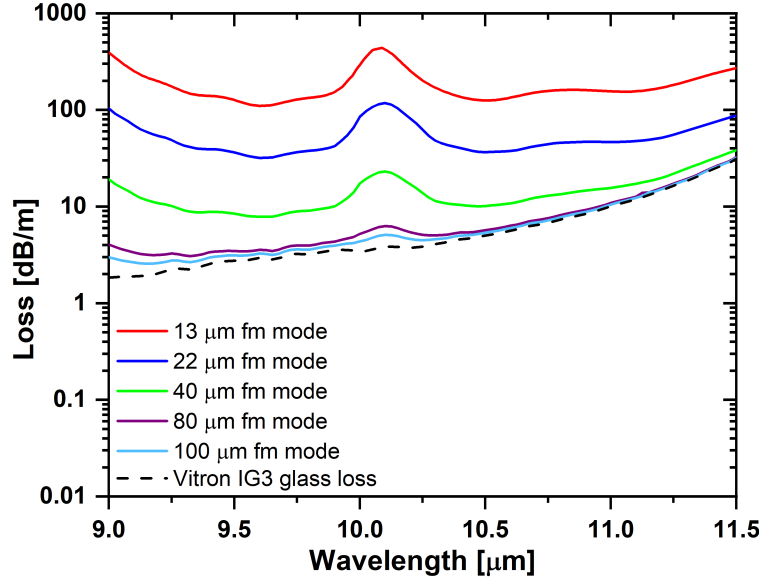
FIGURE 5.14: Simulated attenuation of the fundamental mode for core diameters of 13 (solid red curve), 22 (solid blue curve), 40 (solid green curve), 80 (solid purple curve) and 100 μm (solid light blue curve). The dashed black curve represents the IG3 glass loss.

loss. To do so, I subtract the loss of the bulk glass from the measured loss of the bundle, to obtain the additional loss caused by the bundle fabrication. By dividing this amount by the FEP polymer loss across the wavelength range, I obtain ηClad. This is shown in Figure 5.15 (green curve). Here there are three components: a) one that decreases with wavelength at 3 to 4 μm, which I attribute to additional scattering at the core/clad interface. This becomes negligible at longer wavelengths; b) two peaks at 3.53 and 4.52 μm that are due to chemical interactions between the glass and the polymer that cause additional absorption peaks; and c) a wavelength increasing contribution that is due to an increased power overlap of the optical mode with the lossy polymer at longer wavelengths. Multiplying this overlap by the known loss of the polymer produces the additional loss due to the polymer. In order to extrapolate this latter contribution to wavelengths outside the measurement range of our instrument, I used the following procedure. For large V-number fibres like those in this work, an asymptotic analytical expression exists for ηClad [111]:

$$\eta_{Clad} \approx \frac{u^2}{V^3} \tag{5.1}$$
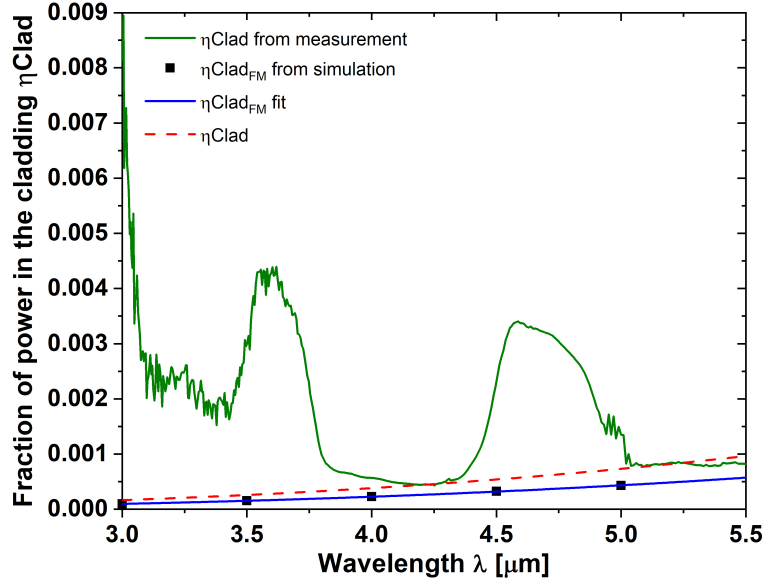
FIGURE 5.15: Fraction of power in the cladding of the bundle of 13 μm calculated from measurement (green curve). Fraction of power in the cladding of the fundamental mode simulated on a fibre with core of 13 μm (black squares) and its fit (blue curve). Estimated fraction of power in the cladding (dashed red curve).

where u represents the normalised transverse wave vector in the core. From this, the dependence of the cladding overlap on the wavelength λ can be expressed as:

$$\eta_{Clad} = k_1 \lambda^3 e^{k_2 \lambda} \tag{5.2}$$

where k_1 is a constant which depends on the excited modes and $k_2 = 2/(2\pi\rho NA)$ only depends on the fibre's known structural parameters such as the core radius ρ and the NA [111]. The validity of Equation 5.2 was verified through modelling, as follows. Since the fibre bundle can be seen as an array of optical fibres with low/negligible cross-talk between them (as shown above), I modelled a single fibre made of an IG3 glass core and FEP cladding using FEM simulations in Comsol Multiphysics. The complex refractive index of the glass and of the polymer shown in Figure 4.1 were used, and a PML was employed to avoid reflections from the outer boundaries [69]. The core diameter was set to 13 μm. The fraction of power in the cladding of the fundamental mode (ηClad_{FM}) was simulated at wavelengths between 3 and 10 μm. For the fundamental mode, this equation was found to agree fairly well with the simulated ηClad_{FM}, with small differences likely arising from the approximate nature of Equation 5.1. I further observed that if I used k_1 as

free parameter in the fit of the simulation values with the Equation 5.2 in the 3-11.5 μm spectral range, the agreement between formula and simulations improved. The simulated ηClad_{FM} (black squares) and its fit with Equation 5.2 are shown in Figure 5.15 between 3 and 5.5 μm (blue curve). Since these fibre bundles are heavily multimoded, in practice the IR radiation from the object to be imaged excites a combination of modes. The average ensemble of the excited modes has a larger overlap with the polymer than just the fundamental mode. From the value of the experimentally extracted fractional power in the polymer (green curve) at 4.23 μm, the position of the main polymer peak observed in Figure 4.1, I calculated the value of the constant k_1 by using Equation 5.2. The calculated constant k_1 takes into account the average ensemble of the excited modes of our bundle. I then estimated the spectral behaviour of the fraction of power in the cladding for a fibre with a core of 13 μm, and this is shown in Figure 5.15 (dashed red curve). Next, I applied the same method to a fibre with a core diameter of 22 μm, for which I also had experimental results (see Figure 4.1). As one would expect, enlarging the core causes a lower cladding overlap due to the ensemble of modes, which explains why the larger bundle was found to have overall lower loss. Since this semi-empirical method showed a good agreement between the measurements and the simulations for cores of 13 and 22 μm, I then also used it to predict the behaviour of bundles with larger pixel dimensions. The cladding overlap due to the average ensemble of excited modes cannot be calculated accurately for the larger core sizes as it depends on the number of guided modes, on the individual modal excitation at launch, on the intermodal mode coupling and external perturbation, etc. Nonetheless, from Equation 5.1 it is possible to derive the dependence of the overall fraction of power in the cladding due to the excitation of several modes as a function of the core radius [111]:

$$\sum \eta_{Clad} = \frac{k_3 e^{-\frac{k_4}{\rho}}}{\rho^3} \tag{5.3}$$

where k_3 is a constant which depends on the excited modes and k_4 is expressed as:

$$k_4 = \frac{2\lambda}{2\pi NA} \tag{5.4}$$

I then estimated the dependence of the overall fraction of power in the cladding on the core diameter, by fitting the overlap extracted from measurements for cores of

13 and 22 μm with Equation 5.3. With this estimated overlap I could then produce the various curves in Figure 5.16 for different core diameters (13, 22, 40, 80 and 100 μm). For all these cases, the dashed curves of Figure 5.16 represent the simulated attenuation of the fundamental mode only, while the solid curves represent the estimated attenuation of an ensemble of several modes. Note that this is a big approximation, given that the number of excited modes might also change from bundle to bundle and that there was a non-negligible experimental error in the measurements, and it should be therefore only considered as general guidance only. However, theory predicts that the overall fraction of power in the cladding should become decreasingly smaller with increasing pixel size. I therefore believe that the general conclusions shown in Figure 5.16 are to a first order approximation correct. A grey hashed bar was placed in the spectral range region where the FEP polymer losses were too high to be measured (7.96-8.75 μm wavelength).
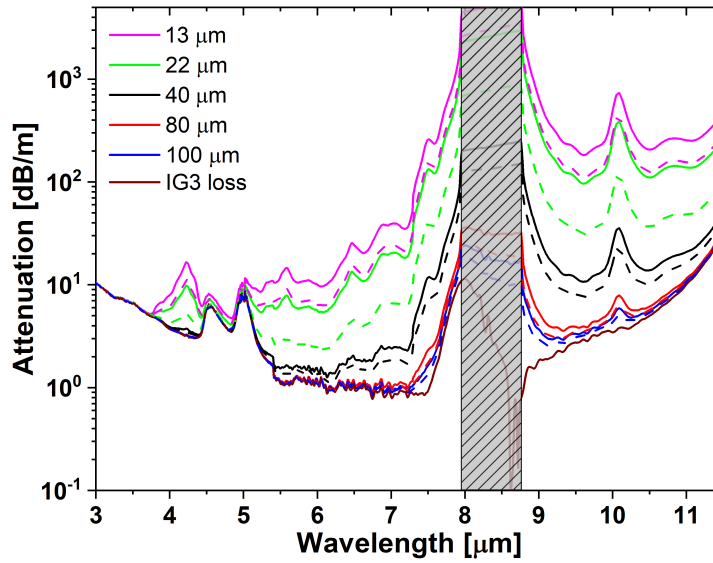
FIGURE 5.16: Attenuation calculated by using the procedure explained in the Appendix for core diameters of 13 (solid magenta curve), 22 (solid green curve), 40 (solid black curve), 80 (solid red curve) and 100 μm (solid blue curve). The dashed curves represent the simulated attenuation for the fundamental mode. The brown curve represents the IG3 glass loss. The grey hashed bar represents the spectral region where the FEP polymer were too high to be measured.

Between 9 and 11.5 μm, the fibre bundles with 13 and 22 μm pixel diameter have impractically high losses approaching 100 dB/m, indicating that in order to scale with the wavelength, the core diameter should be larger. A fibre bundle of 40 μm has losses between 10.7 and 35.5 dB/m from 9 to 11.5 μm, with a minimum at 9.64 μm. In the same wavelength range, bundles with 80 μm and 100 μm core,

would have more reasonable losses of 3.6 to 11.5 dB/m and 2.9 to 10.7 dB/m, respectively. This is not so much higher than the bulk loss of the glass (shown in brown in Figure 5.16), despite the extremely high loss of the FEP polymer at these wavelengths. From this, I can conclude that in order to achieve a reasonable loss for thermal imaging in the long wavelength IR region, bundles with pixel sizes of the order of 80 μm, or above should be used. Using such large pixels would have the obvious disadvantage of increasing the overall diameter of the bundle, which might compromise its flexibility. One workaround could be that of allowing individual fibres or subsets of the total bundle to be independent and only attaching them at the bundle extremities to form a coherent imaging system.

5.5 Conclusion

In this chapter, the loss measurement, the thermal imaging performance and the inter-core cross-talk measurement of the fibre bundles have been presented. Using the larger of the fabricated bundles, sharp edged thermal images of objects at temperatures down to 80 °C were obtained through a bent bundle which was 1.15 m long. A thermal image of a human hand was also performed through a shorter bundle of 62.5 cm. An inter-pixel cross-talk as low as -13.7 dB/m was measured, which was sufficient to avoid degradation of the thermal imaging quality, and stemmed from the high index contrast between the glass core and polymer cladding. This result can be improved further in future works by increasing the lengths over which thermal imaging of room temperature object can be performed. To do so, one would need to decrease the fibre bundle loss, by either changing or purifying the core material, or by further enlarging the pixel size to reduce the interaction of the modes with the lossy polymer cladding. To capture endoscopic thermal images using lower cost and simpler, long wavelength IR microbolometric thermal cameras, my modelling study indicates that considerably largely pixel dimensions, of the order of 80 μm, would be needed in order to minimise the fraction of modal power in the cladding, which is extremely lossy at those wavelengths.

Chapter 6

HC-ARFs and mid-Infrared laser delivery

In this chapter, the background on mid-IR laser delivery for CO and CO_2 laser transmission and the theory of HC-ARFs is presented. In addition, validations of the FEM models to simulate both straight waveguide and bending losses of HC-ARFs are reported.

6.1 Mid-IR beam delivery

The mid-IR spectral region (between ∼3 and 12 μm) is of growing importance to a range of applications. This is in part motivated by the presence of the fundamental absorption features of important molecules in this wavelength range and also several atmospheric transmission windows. These applications have been driving forward optical source and detector development and now a range of laser sources, e.g. QCLs, gas lasers etc. are commercially available.

Today, CO and CO_2 lasers are the most extensively deployed mid-IR laser sources and they are often used in medical, industrial and military applications [1, 2]. Key operation wavelengths for these lasers are 5.4 and 10.6 μm, respectively. In medicine, laser radiation emitted from CO and CO_2 lasers is widely used for skin ablation, gingival and teeth treatment, heart revascularization, diagnosis and treatment of cancer [1]. These lasers are also employed in industrial applications for material processing, such as glass and metal cutting, welding and inscribing [2].

The main limitation for these applications is that a flexible and compact transmitting medium, which maintains good laser beam quality (Gaussian beam) and enables remote access into inaccessible areas, is still needed. A system of articulated arms, as shown in Figure 6.1 [26], enables delivery of CO_2 laser radiation with a good beam quality.

This instrument, which comprises of a series of arms and mirrors, has limited
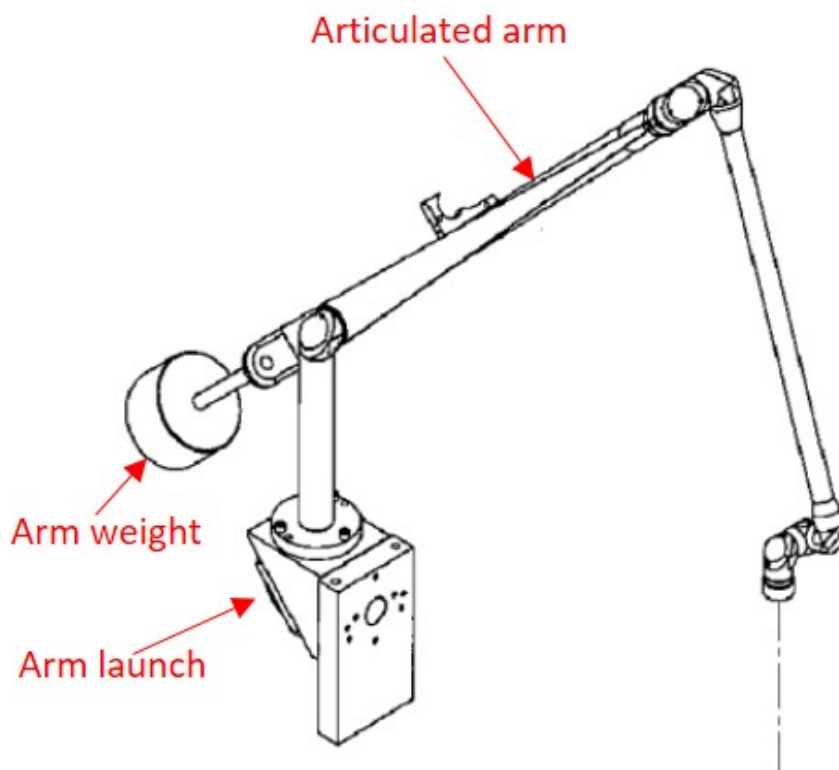
FIGURE 6.1: Articulated arms for CO_2 laser radiation. Reproduced from [112].

operability in inaccessible points (i.e. endoscopy) due to its large dimensions. Optical fibres could provide an ideal alternative solution for flexible delivery of mid-IR light. The key advantages offered by optical fibres for these applications are the compactness, mechanical flexibility and the fibre length; these factors combined can enable access to inaccessible points. This is very useful for surgery, material processing and military applications, where a compact and flexible transmitting medium is needed. Considering possible optical fibres, those with solid core are not suitable for laser delivery in the mid-IR because of the material heating and melting, and non-linearities of the fibre material. Omniguide, which is a commercially available hollow core Bragg fibre for the transmission of CO_2 laser radiation [24], is a possible solution but it is not single mode due to its large core diameter

[25]. This deteriorates the output beam quality. Here, I study an alternative with a Gaussian beam, low loss and low non-linearities.

In the near-IR silica-based optical fibres provide outstanding performance for a host of applications, but beyond $\sim$2.3 μm, the silica attenuation sharply increases and these more 'conventional' fibres are no longer an option for beam delivery. In the last few decades, there has been significant effort to design and fabricate mid-IR fibres and both solid and hollow core fibres have been demonstrated as transmitting media for mid-IR laser radiation, such as CO and CO_2 lasers. In the next sections, these reported mid-IR fibres are reviewed and design choices for the fibres reported in this thesis are explained.

6.2   Mid-IR Optical fibres

As explained in the previous section, while silica is an excellent optical material for the near-IR, above 4.5 μm it has attenuation higher than 3000 dB/m and this generally increases even further towards longer wavelengths. Many optical fibres have been fabricated which explore alternative mid-IR materials and these fibres can first be broadly categorised as solid core or hollow core fibres.

Reported solid core fibres for the mid-IR are based on the mid-IR transmitting materials discussed in Chapter 3. These includes glasses such as fluorides, tellurite and chalcogenides and crystalline structures. Low transmission losses, such as 0.7 dB/km at 2.6 μm [113], 0.05 dB/m at 2 μm [31] and 0.014 dB/m for 4.8 μm [114] have been reported for fluoride, tellurite and chalcogenide glass fibres, respectively. However, the bulk properties of these materials struggle to compete with the performance of silica in the near-IR and these fibres suffer from issues such as mechanical and chemical stability and it is challenging to produce long, uniform fibre lengths. Furthermore, solid core fibres made from low temperature glasses such as tellurite and chalcogenide have limited power delivery performance as heating of the fibre can lead to the melting of the fibre material [21, 27]. This necessitates that these solid core fibres for mid-IR high power laser transmission need to be cooled with a gas or water flow to avoid the material heating and melting [115]. Finally, materials such as chalcogenide have a relatively high non-linear coefficient (1000 times higher than silica) [28] and this means that laser transmission in these fibres can suffer from unwanted non-linear effects. The maximum

CO and CO_2 laser power transmitted through solid core fibres is 85 and 225 W, respectively [115, 116].

Hollow core fibres (HCFs) offer an exciting alternative and in recent years many different designs, based on different guidance mechanisms, have been reported [117, 118]. These include hollow dielectric waveguides [119], hollow Bragg waveguides [120], hollow core metallic waveguides [121], photonic bandgap fibres (PBGFs) [122] and hollow core antiresonant fibres (HC-ARFs) [123].

The propagation of light through a hollow core waveguide made of a metallic or a dielectric tubular surround has been theoretically studied in 1964 by Marcatili for telecommunication applications [119]. In this study, it was found that in order to achieve low propagation loss, the core radius should be much larger than the wavelength [119]. Since HCFs consisting of a glass capillary guide light thanks to the total external reflection of the light, they are leaky. This is because at each bounce a fraction of light is refracted and lost, hence the modes are leaky, limiting the achievable loss [124]. For this reason, more complex HCFs, as hollow Bragg waveguides [120], hollow core metallic waveguides [121], PBGFs [122] and HC-ARFs [123] have been studied to try to minimise the light leakage.

Bragg reflection waveguides, which were proposed in 1976 by Yeh et al. [120], consist of a hollow core surrounded by periodic alternating cladding layers of high and low refractive index material. In this way, the leakage loss is reduced thanks to Bragg reflection [120]. Temelkuran et al. [24] developed a hollow core flexible Bragg fibre (known as Omniguide) consisting of several alternating layers of a high refractive index material and a low refractive index material (Figure 6.2a). The high refractive index material was As_2Se_3, and the low refractive index material was PES polymer [24]. They obtained losses as low as 0.95 dB/m at a wavelength of 10.6 μm [24]. Despite commercial success, these fibres have large core diameters (e.g., 750 μm) and large ODs (e.g., 1.2 mm). The large core diameter leads to high bending loss and to the excitation of high order modes and this deteriorates the output beam quality.

Hollow core metallic waveguides consist of a HCF where the inner part of the capillary is coated with a metallic layer to improve the confinement. The first rectangular hollow core metallic waveguide, made using aluminium sheets, were developed in 1980 to transmit CO_2 laser radiation [121]. The resulting waveguide was 1.2 m long and heavily multimoded [121]. In general, metal-coated HCFs
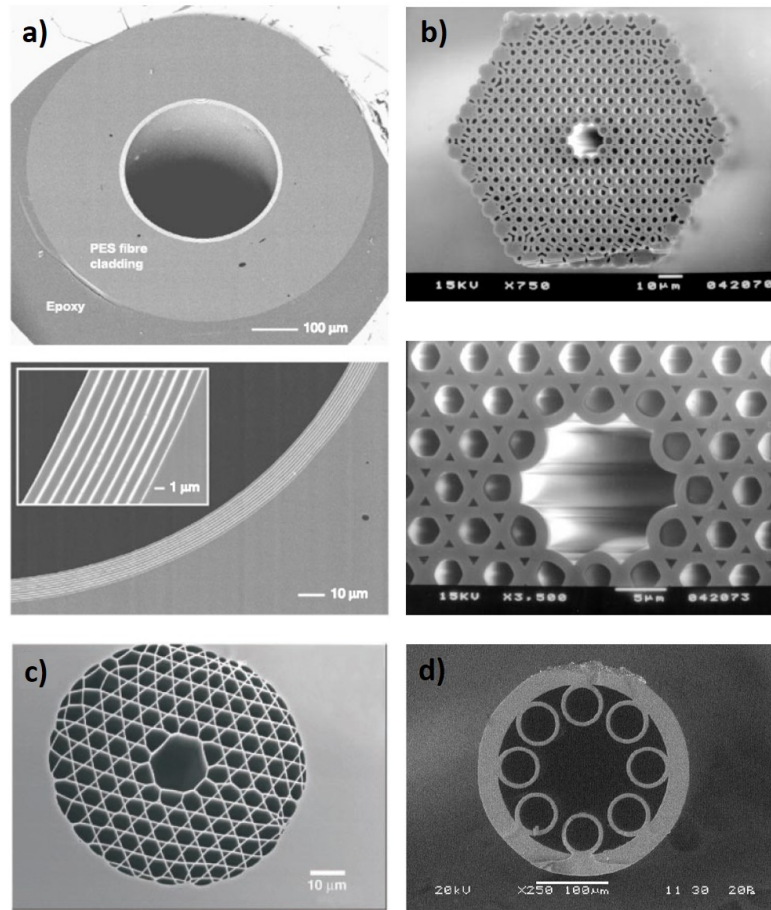
FIGURE 6.2: a) Omniguide fibre [24], b) microstructured PBGF [124], c) Kagome antiresonant fibre [129] and d) HC-ARF [30]

present large core dimensions leading to highly multimoded fibre which deteriorates the output beam quality [125].

Alternative candidate fibres have been enabled by the development of hollow core microstructured fibres (HC-MOFs) [30, 117, 124]. In these fibres, low loss transmission is enabled in a hollow core by a carefully designed cladding structure which can be made up of a few to several hundred air holes. These air holes are defined by a single material, usually silica, but soft-glass and polymer HC-MOFs have also been reported. Microstructured HC-PBGFs based on this idea were fabricated for the first time at the University of Bath in 1999 [124] (Figure 6.2b); these fibres confine light inside the air core, at a certain frequency and propagation constant, thanks to the optical bandgap effect created by the 2D periodic holey cladding structure (periodic layers) [126]. The number of air hole layers in a PBGF is important in reducing confinement loss and therefore these fibres typically have several hundred holes in the microstructured cladding. In a PBGF, confinement

loss can be reduced to be essentially negligible by increasing the numbers of ring of holes surrounding the core [127]. Optically, these fibres present a narrow low loss transmission band and are very robust to bending [117]. HC-MOFs have very low overlap between the core guided light and the cladding structure and this is very interesting for their applications as mid-IR fibres as even a silica-based HC-MOF can provide low loss guidance well beyond the conventional transmission window for silica. Wheeler et al. [128] fabricated a silica HC-PBGF which allowed mid-IR transmission between 3.1 and 3.7 μm. This fibre had an overlap between the guided mode and the cladding structure lower than 0.3 % and had a minimum loss of 0.13 dB/m at 3.3 μm (0.05 dB/m post purging).

From 2002 onwards [129] an alternative type of HC-MOF has also been developed. These fibres trap light in an air core via antiresonance rather than a PBG and they are often referred to as HC-ARFs (Figure 6.2c). A wide range of holey structured cladding designs can be used to create a HC-ARF. One of simplest, and most commonly reported HC-ARF consists of a hollow core surrounded by circular cladding tubes of a certain thickness (Figure 6.2d) [30]. The thickness of these membranes is critical in defining the wavelength ranges in which a HC-ARF transmits light with low attenuation and low loss transmission across several, broad wavelength ranges is possible [126]. Furthermore, through careful design, HC-ARFs can allow effectively single mode guidance and depending on the internal structure they can have low straight waveguide and bending loss [117]. Pryamikov et al. [130] reported the first mid-IR HC-ARF made of silica glass consisting of 8 touching cladding tubes. This work demonstrated that such fibre structure allows to obtain transmission loss lower than 0.1 dB/m at ~3.7 μm. Few years later, Kolyadin et al. [30] fabricated a silica HC-ARF, consisting of 8 non-touching cladding tubes. This fibre transmitted between 2.5 and 7.9 μm with a minimum loss of 50 dB/km at 3.39 μm. Due to the high silica glass bulk absorption beyond 4.5 μm, this HC-ARF shown loss of the order of 30 and 50 dB/m at 5.8 and 7.6 μm, respectively. This attempt showed that these HC-ARFs have huge potential in the mid-IR spectral range.

One of the aims of this work, as will be shown in later sections, is to develop a transmitting medium for CO and CO_2 laser delivery and HC-MOFs are attractive for this application. Since these lasers emit at 5.4 and 10.6 μm, where silica HC-MOFs present high loss [30], there is a need to use mid-IR glasses such as chalcogenide, tellurite and fluoride, which have inferior mechanical properties than silica

glass. HC-PBGFs are very difficult to fabricate with mid-IR glasses [131] because of the complex cladding structure, where, in order to broaden the bandgap, the glass structure should be as thin as possible [117]; making thin glass structures with mid-IR glasses as chalcogenide and tellurite is extremely challenging, largely due the steep viscosity-temperature curve for these soft-glasses. However, for HC-ARFs, due to the different guidance mechanism, the cladding structure required for low loss transmission can contain significantly reduced elements, which have thicker membranes. This potentially simplifies the fabrication procedure and also is more amenable for making fibres from the mid-IR transmitting glasses considered above.

Furthermore, HC-ARFs have even lower light-glass overlap than HC-PBGFs, down to 5×10^{-5} for specific designs [117]. Such a low glass overlap opens up a host of interesting fibre properties, including low non-linearity, high damage threshold and the potential for ultra-low loss [117] and for light transmission at wavelengths even further beyond the transmission window of a given material. The optical properties of HC-ARFs such as the modal purity, multiple, broad transmission windows and the simpler structure than PBGFs seem to make HC-ARFs the best option for mid-IR spectral range applications, such as laser delivery. Whilst silica is the material of choice for near-IR applications for its excellent transmission, silica HC-ARFs can only provide guidance with practically low optical loss up to $\sim$4.5 μm [29, 30]. For longer wavelengths, soft-glasses represent a solution to extend the transmission beyond $\sim$4.5 μm.

Considering these reasons, in this thesis, one of the key goals was the fabrication of HC-ARFs for mid-IR light transmission and in Chapters 7 and 8 detailed experimental results on the fabrication of tellurite and chalcogenide HC-ARFs are presented. In the next sections, antiresonant guidance is first explained in detail and then reported HC-ARFs fabricated from soft-glasses are reviewed.

6.3 Antiresonance guidance

HC-ARFs guide light thanks the mechanism of the antiresonance. In particular, the core of HC-ARFs is surrounded by solid thin membranes with a refractive index n_2, which are highly reflective in some wavelength regions if they are dimensioned with a certain thickness d [126]. Thanks to these reflective membranes, HC-ARFs

can confine light in the core region. The membranes of these fibres act as a Fabry-Perot resonators [126]. By considering a thin solid membrane with a thickness d as shown in Figure 6.3 and with a refractive index n_2 which is higher than the refractive index of its surroundings (n_1), an incident ray to the membrane wall with an angle θ can be refracted and transmitted in the membrane with an angle α. The transmission coefficient T of the membrane is related to the reflectivity R and the phase difference between two transmitted rays δ, which is defined as [132]

$$\delta = \frac{2\pi}{\lambda} n_2 cos(\alpha) d \tag{6.1}$$

The transmission coefficient T is defined as

$$T = \frac{(1-R)^2}{(1-R)^2 + 4Rsin^2(\delta)} \tag{6.2}$$

and it is maximum when

$$\delta = m\pi \tag{6.3}$$

and where m is an integer [132]. For a very small incident angle θ (close to 0°),
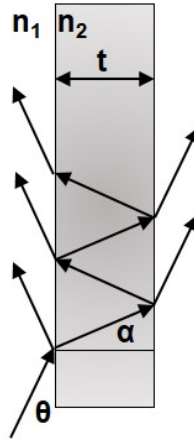
FIGURE 6.3: Propagation constant and transverse wavevector in the air core and in the glass layer of a HC-ARF.

the refracted angle α can be expressed as

$$sin\alpha = \frac{n_1}{n_2}, \tag{6.4}$$

By using Equations 6.1, 6.3 and 6.4, the wavelengths at which the resonance occurs (λ_m) can be calculated as

$$\lambda_m = \frac{2d}{m}\sqrt{n_2^2 - n_1^2} \tag{6.5}$$

At the wavelengths that satisfy the resonance condition, the transmission T through the membrane is maximised. On the other hand, at wavelengths away from these resonance wavelengths, the membranes are highly reflective and the transmission through the membrane is low [132]. In this case, the membrane is in antiresonance. As mentioned above, HC-ARFs have a hollow core surrounded by thin membranes. Figure 6.4 shows the typical transmission spectrum of a HC-ARF with one high refractive index layer. At the resonance wavelengths, the light propagating through core of the HC-ARF leaks through the cladding and the fibre transmission goes to zero (Figure 6.4) [126]. In contrast, in antiresonance condition, the light is reflected by the membranes and it is confined within the core. This maximises the HC-ARF transmission.
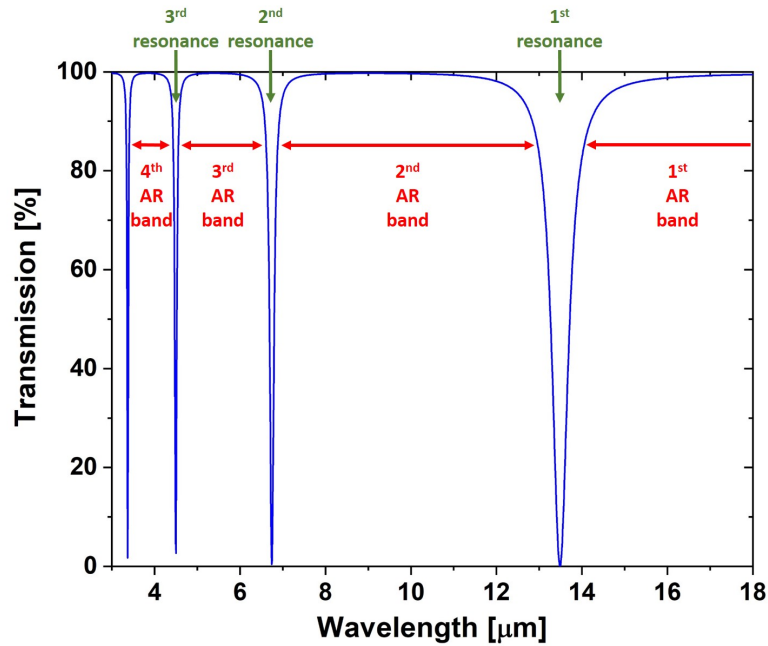
FIGURE 6.4: Typical transmission spectrum of HC-ARFs.

Losses in HC-ARFs can be caused by different contributions. The most important are confinement, scattering, bending and material absorption. Confinement loss is due to light leakage from the core. This contribution depends on the number of antiresonant layers, the shape of the membranes and on the core size. It has been

demonstrated that by increasing the number of antiresonant layers and the core diameter in a HC-ARF, the confinement loss decreases [133]. Figure 6.5 shows simulations of confinement loss in dB as a function of the core radius/wavelength ratio (a/λ) of a Marcatili HCF (inset with blue contour), of a HC-ARF with 1 antiresonant layer or jacketed tubular fibre (inset with red contour) and of a HC-ARF with 2 antiresonant layers (inset with black contour) extrapolated from [133]. As shown in Figure 6.5, a HC-ARF with 1 single layer has loss 35 times
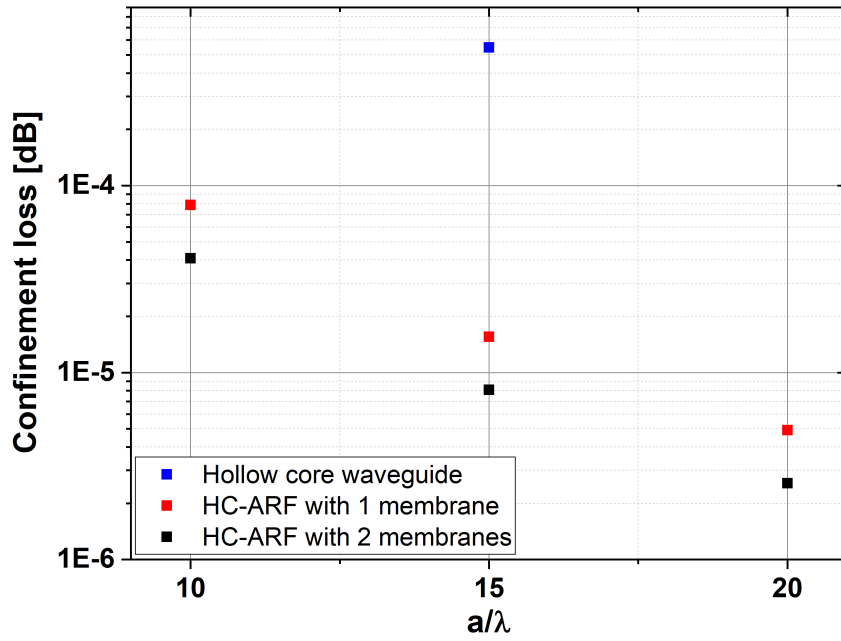
FIGURE 6.5: Simulations of confinement loss in dB as a function of the core radius/wavelength ratio of a Marcatili HCF (squared blue dot), of a HC-ARF with 1 antiresonant layer (squared red dots) and of a HC-ARF with 2 antiresonant layers (squared black dots) extrapolated from [133].

lower than a Marcatili HCF. By adding a second layer in a HC-ARF, it is possible to further reduce the loss by a factor of 2. Moreover, as shown in Figure 6.5, by increasing the core radius, the confinement loss decreases. Since these kind of HC-ARF structures are impossible to fabricate, several alternative solutions to create antiresonant membranes surrounding a hollow core region have been proposed. One of the simplest structures of HC-ARF consists of several cladding capillaries surrounding the core, which are in contact, as shown in Figure 6.6a. Each capillary of this fibre acts as an antiresonant membrane. In this design, the contact points between the capillaries create unwanted resonances that increase the light leakage as demonstrated by Kolyadin et al. [30]. In fact, a HC-ARF structure with non-touching capillaries omits these contact features and their negative impact on the

optical performance as shown in Figure 6.6b and this can decrease the confinement loss across the transmission bands [30]. The gap between each capillary affects the confinement loss [134]. By adding one capillary inside each capillary of a non-touching HC-ARF, it is possible to reduce the confinement loss further [117]. This fibre structure, which is shown in Figure 6.6c, is called a Nested Antiresonant Nodeless fibre (NANF) [117]. The presence of non-uniformities or imperfections
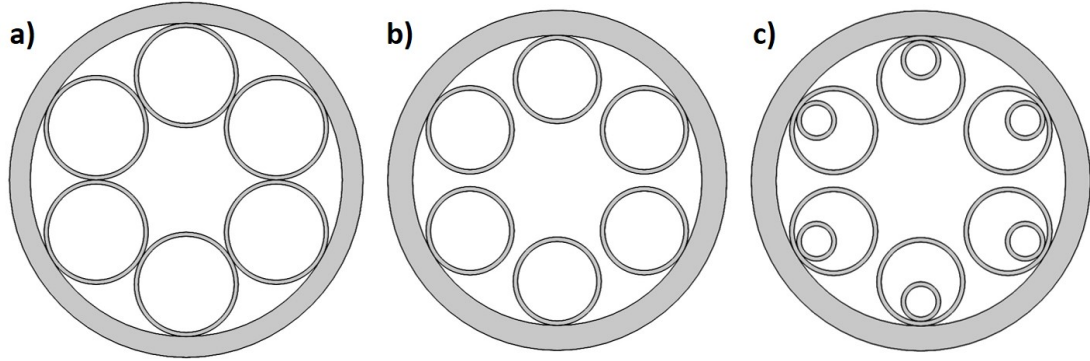
FIGURE 6.6: a) HC-ARF with capillaries in contact, b) HC-ARF with non-touching capillaries and c) Nested Antiresonant Nodeless fibre (NANF).

in HC-ARF structures, due to a non-constant radial thickness of the capillaries and capillaries out of position (capillary dislocation), increases the confinement loss [33, 135]. These problems are more accentuated in HC-ARFs made of mid-IR glasses as tellurite and chalcogenide because they are more difficult to process compared to silica glass due to their steep viscosity-temperature curves. In Chapters 7 and 8, non-uniformity problems encountered during HC-ARF fabrication from tellurite and chalcogenide are disclosed and methods to minimise these imperfections, to decrease the confinement loss of the HC-ARFs, are discussed. Also, in Chapter 8, a modelling study which shows how the uniformity of the membranes and their shape is important to decrease the fibre loss is presented.

Scattering loss in HC-ARFs is due to the roughness of air-glass interface [117]. Since these fibres transmit thanks to antiresonance, the electromagnetic field in the air-glass interface is minimised and the scattering has a lower contribution than the confinement on the fibre loss [117].

Bending loss occurs when the HC-ARF is bent with a certain radius of curvature. The bending loss contribution can be minimised be decreasing the core diameter [117]. This, as mentioned above, increases the confinement loss, so there is a trade-off. The effect of bending in HC-ARFs will be shown in Section 6.3.1.2.

The material absorption influences the overall loss of the HC-ARFs due to the small overlap of the mode with the cladding material [136]. In Chapters 7 and 8,

it will be shown how the material absorption affects loss in a HC-ARF.

In this thesis, only the most dominant loss contributions on the overall HC-ARF loss which are confinement loss, material absorption and bending will be studied. In the next section, the validation of the FEM models to simulate these loss contributions is presented.

6.3.1   HC-ARFs FEM model validation

In this work, in order to understand and evaluate the confinement loss, material absorption contribution and bending loss of HC-ARFs, a FEM approach has been used. In particular, as will be shown in Chapters 7 and 8, modelling was useful to estimate the loss of target HC-ARF designs prior to fabrication and also to simulate the straight waveguide and bending loss of fabricated HC-ARFs. In order to do these simulations with a good accuracy, two validation studies, similar to the study for solid core fibres in Chapter 2, were performed for straight waveguide and bending losses. In the case of straight waveguide loss, the FEM model was verified against analytical results. In the case of bending loss, the FEM model was validated against a published work.

6.3.1.1   Straight waveguide loss validation in HC-ARFs

In order to validate the FEM model of HC-ARFs, which enables simulation of straight waveguide loss, the effective index (n eff) and the confinement loss of a jacketed tubular fibre, which consists of a HCF with a tubular antiresonant layer as shown in the inset of Figure 6.7a, were simulated by using Comsol Multiphysics.

The jacketed tubular fibre had a core radius, r, of 17 μm, a tube 0.7 μm thick and a gap between the tube and the jacket, g, of 10 μm. The simulated effective index and the confinement loss of the jacketed tubular fibre have been compared with the analytical values which my colleague Dr Mohammad Mousavi obtained by using the transfer matrix method (TMM) as described in [137]. Figures 6.7a and b show the effective index and the confinement loss simulated and calculated at 1 μm wavelength by using Comsol Multiphysics and the TMM, respectively. From the graphs, it is possible to notice that a mesh size equal to $\lambda/5$ (hmax =
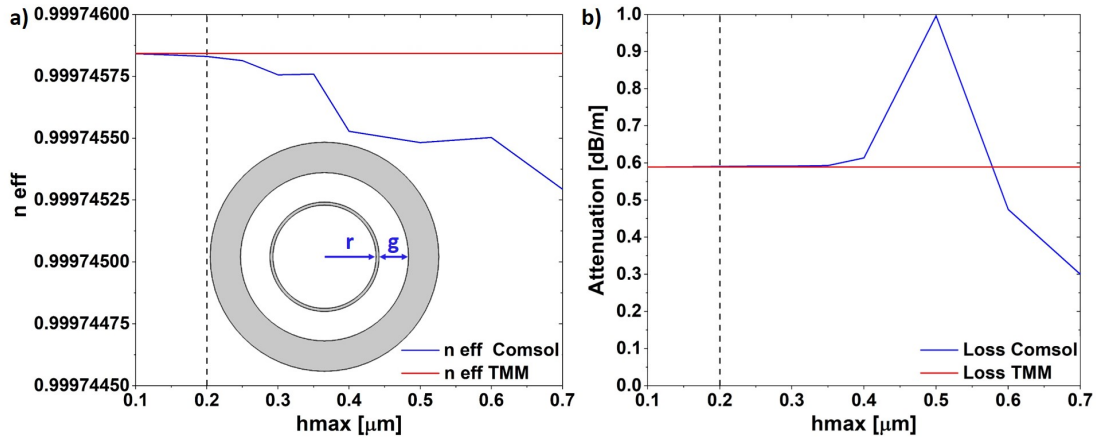
FIGURE 6.7: Validation of a jacketed tubular fibre: a) effective index (n eff) calculated analytically by the transfer matrix method (TMM) [137] (red curve) and effective index (n eff) simulated in Comsol (blue curve); b) Attenuation in dB/m calculated analytically by the transfer matrix method (TMM) [137] (red curve) and attenuation in dB/m simulated in Comsol (blue curve).

0.2 μm) enables accurate simulation results with a good computation time (Figure 6.8).
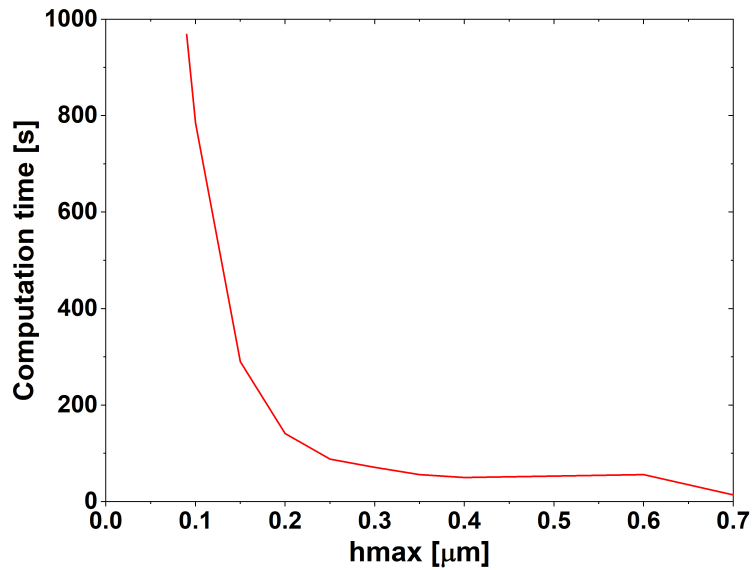
FIGURE 6.8: Simulation time in seconds for a jacketed tubular fibre for different element sizes.

6.3.1.2 Bending loss validation in HC-ARFs

Since a bent optical fibre shows a higher transmission loss compared to a straight fibre [138], the magnitude of bending losses was also studied by using Comsol

Multiphysics. To study the bending loss, the refractive index of the fibre was modified according to the conformal transformation [139] and it is equal to [117]

$$n' = n \cdot e^{\frac{x}{R_{eff}}} \approx n \cdot \left(1 + \frac{x}{R_{eff}}\right) \tag{6.6}$$

where x and R_{eff} are the radial direction of an optical fibre and the effective radius of curvature, respectively. The effective radius of curvature, which takes into account of the elasto-optic effect, is equal to the curvature radius R_c for air/gases and $\sim$1.28 times the curvature radius for glass [140]. Using this conformal transformation, a bent fibre can be considered as a straight fibre with a tilted refractive index [139]. In this way, it is possible to simulate the bending loss using a model for straight fibre loss, but with a tilted refractive index along the fibre radius (radial direction x). In particular, according to Equation 6.6, in order to take into account of the curvature radius in Comsol, the core and cladding refractive indices should be multiplied by $(1+x/R_{eff})$.

In order to validate the Comsol model to study the bending loss of a NANF, the same model applied by Poletti [117] to silica NANFs was developed. The inset of Figure shows the cross-section of the NANF. Core diameters, D, of 30, 40 and 50 μm were investigated at 1.8 μm wavelength. The capillary thickness was 0.55 μm, the distance between the largest capillaries, s, was 2.75 μm and the gap between the inner and outer tube, f, was 0.9 times the core radius. The computational region, which was around 160 μm in diameter, was truncated with a PML. The refractive indices of air and glass were modified according to Equation 6.6. For each core diameter, the curvature radius was changed from 4 to 16 cm by keeping the wavelength constant at 1.8 μm. This conformal transformation did not affect the numerical convergence. However, to produce more accurate results, a mesh size into the core and into the capillaries equal to $\lambda/6$ was chosen. As shown in Figure 6.9, a good agreement with the model of Poletti has been obtained. The small difference in loss between the two models could be attributed to the fact that the mesh was not exactly the same in the two models. For a core diameter of 50 μm, the maximum difference between the two models is of 0.2 dB/m. For a core diameter of 30 μm, the maximum difference between the two models is of 0.0022 dB/m.
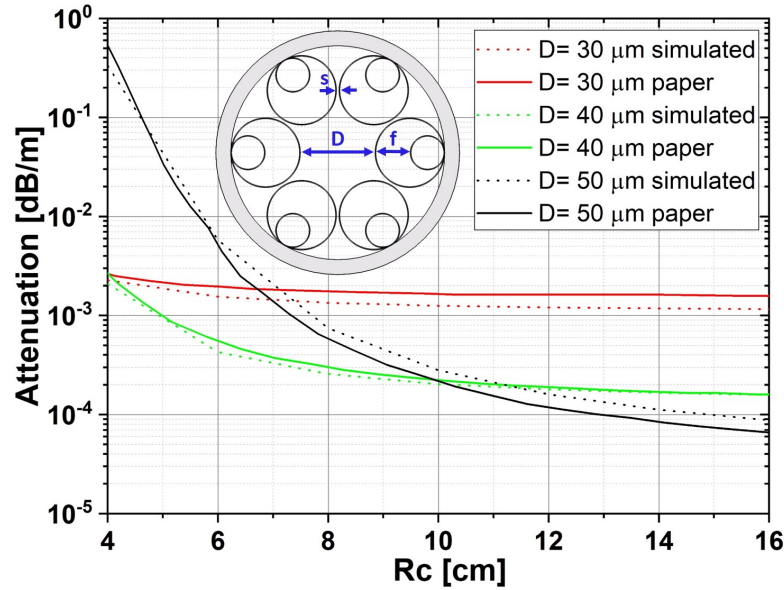
FIGURE 6.9: Bending loss simulation of a nested antiresonant nodeless hollow core fibre (NANF): the solid red, green and black curve represents the attenuation of a fibre with a core radius of 30, 40 and 50 μm at 1.8 μm wavelength for different curvature diameter extrapolated from Poletti [117], while the dashed red, green and black curves represent the attenuation of a fibre with a core diameter of 30, 40 and 50 μm at 1.8 μm wavelength for different curvature radii simulated in Comsol.

6.4   Fabrication of HC-ARF

The fabrication of microstructured fibres is more challenging than solid core fibres. This is because in the case of microstructured fibres, the surface tension promotes the collapsing of the holes during the fibre drawing process [141]. For this reason, pressure can be applied during the drawing process to keep the holes open and to control the hole dimensions, shape and membrane thickness that are achieved in the final fibre. Obtaining long microstructured fibres with a good control of the fibre structure is challenging. The record length in a PBGF with membranes ∼50 nm thick, is 11 km [142]. Obtaining such a long fibre length with constant thickness using soft-glasses is more challenging than silica glass because of crystallisation problems due to multiple heating processes, the steep viscosity curve, and the quality and volume of material available. As will be shown, in state of the art mid-IR HC-ARFs (see next section), it is difficult to get uniform fibre structures. To prevent the capillary collapsing, it is necessary to pressurize the core and the capillaries regions by using a pressurisation system, as will be discussed in Chapter 8.

6.5 Mid-IR soft-glass HC-ARFs

In the last few years several groups have attempted to develop HC-ARFs made of soft-glasses in order to transmit CO and CO_2 laser radiation.

Kosolapov et al. [32] demonstrated a HC-ARF consisting of 8 touching tubes by using $Te_{20}As_{30}Se_{50}$ chalcogenide glass (Figure 6.10a). In particular, they developed a HC-AR preform by stacking 8 capillaries into a jacket tube of $Te_{20}As_{30}Se_{50}$ chalcogenide glass [32]. The preform was drawn into a fibre with 750 μm diameter, with a 380 μm core diameter and capillaries with thickness of 13 μm. During the draw they applied pressure into the capillaries to prevent the capillaries collapsing. In the final fibre some of the capillaries were detached from the jacket tube. Initially, the loss of the fibre was measured by using a FTIR spectrometer and a loss of 13.5 dB/m at a wavelength of 10.6 μm was recorded. However, in this measurement, some of the light was transmitted in the fibre cladding structure. Subsequently, a better measurement was performed by exciting only the air-core with a CO_2 laser (10.6 μm wavelength), obtaining a loss of 11 dB/m [32]. The beam profile at the output of the HC-ARF was investigated by using a thermal camera and it was not circular due to the non-uniformity of the core region, which was due to the detachment of the capillaries from the external jacket tube [32].

Shiryaev et al. [33] developed a HC-ARF made of 8 touching tubes of As_2S_3 chalcogenide glass (Figure 6.10b). In particular, the fibre was fabricated by using the stack and draw approach. HC-ARFs ranging from 700 to 900 μm in OD were reported [33]. During the draw some capillaries dislocations occurred. They changed the pressure applied into the capillaries until they obtained a symmetric structure with capillaries attached to the external jacket tube. The attenuation of the obtained HC-ARFs was measured by using the cut-back technique with a FTIR spectrometer. In order to reduce the cladding tube modes, they applied a coating on the input and output surface of the fibre by using a Gallium-Indium alloy [33]. The fibre had a minimum loss of 3 dB/m at 4.8 μm wavelength. At 5.4 μm the fibre loss was of the order of 4 dB/m [33].

Gattass et al. [34] fabricated a HC-ARF consisting of 8 non-touching tubes made from As_2S_3 chalcogenide glass (Figure 6.10c). They developed the HC-AR preform by extrusion of a As_2S_3 chalcogenide glass billet and obtained a structure with regular capillaries that were well attached to the external jacket tube [34].
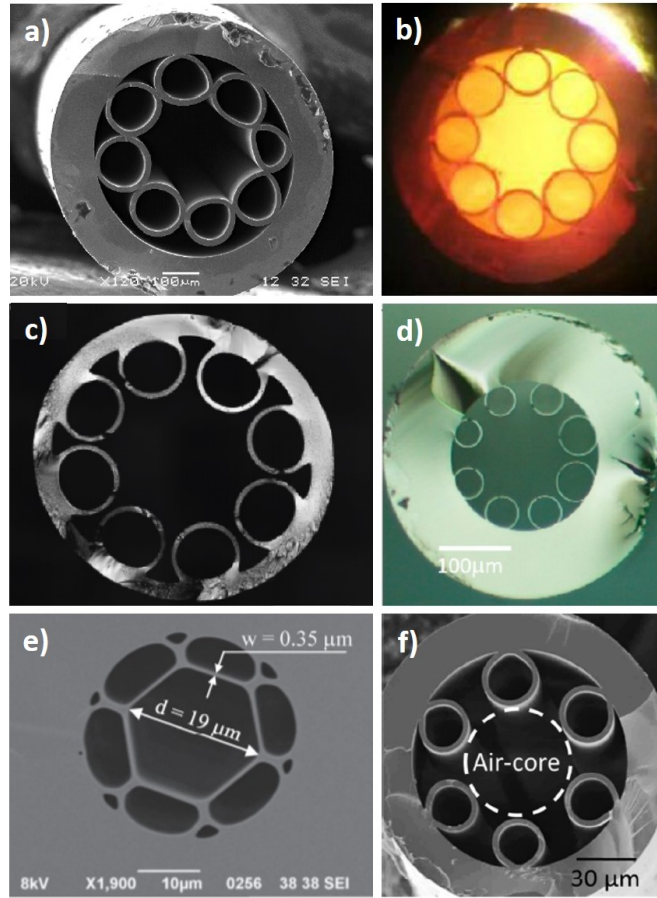
FIGURE 6.10: Mid-IR HC-ARFs reported in literature: a) Kosolapov et al. [32], b) Shiryaev et al. [33], c) Gattass et al. [34], d) Belardi et al. [35], e) Tong et al. [36] and f) Tong et al. [37].

The preform shape was not perfectly circular, instead it was octagonal. A fluoropolymer tube was glued into the core region by using an epoxy. The capillaries of the preform were left open. In this way, during the draw, they applied pressure only in the capillaries by leaving the core region at atmospheric pressure [34]. The pressure into the capillaries was changed until they minimised the gap between each capillary. Although the final fibre was not perfectly symmetric, due to some variation in capillaries thickness and shape, the capillaries were maintained in position during the draw. This represents an advantage compared to the stack and draw approach [34]. The HC-ARF losses were measured by using a FTIR spectrometer. At 5 and 10 μm wavelength they were 2 and 2.1 dB/m, respectively [34]. They also performed a modelling study on an antiresonant fibre structure showing lower loss than the obtained fibre. This could be attributed to imperfections in the fibre geometry and also could be due to the measurement technique which does not only excite the fundamental mode [34].

Belardi et al. [35] fabricated a borosilicate HC-ARF made of 8 non-touching capillaries by using the stack and draw approach (Figure 6.10d). The fibre had a core diameter of 122 μm. The loss of the fibre was of 4 dB/m between 5 and 5.2 μm wavelength [35].

Tong et al. [36] developed a HC-ARF made of tellurite glass (Figure 6.10e). They stacked 6 touching capillaries into a jacket tube obtaining a fibre of 160 μm of OD with a core diameter of 19 μm. A 7 cm long fibre was tested by using a supercontinuum between 500 and 1500 nm. However, the fibre loss has not been measured.

The same group later [37] fabricated a tellurite HC-ARF by stacking 6 non-touching capillaries (Figure 6.10f). The fibre had a core diameter of about 60 μm and a capillary thickness of 2.8 μm. They obtained transmission in a 17 cm long fibre for wavelengths between 2 and 3.9 μm. Again, in this case the fibre loss has not been measured.

A comparison between the losses of Omnigude and HC-ARFs present in literature is shown in Figure 6.11.
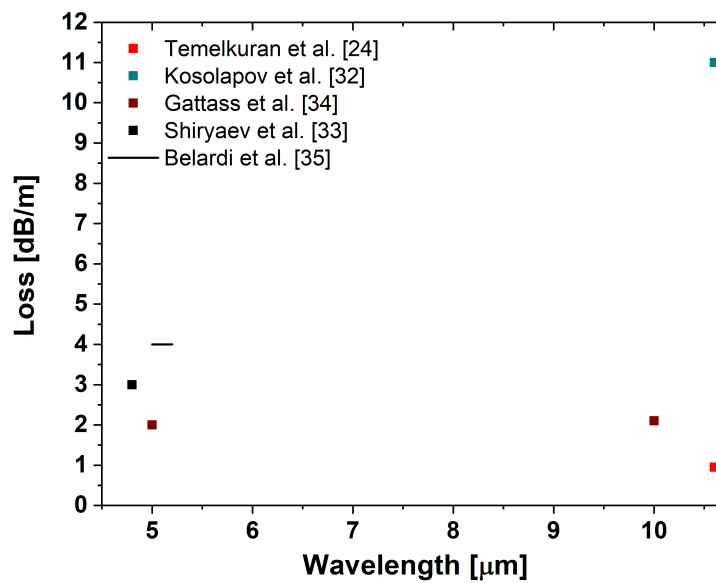
FIGURE 6.11: Comparison between the losses of Omnigude and HC-ARFs reported in the literature.

6.6 Conclusion

In this chapter, the background of HC-ARFs and their potential for CO and CO_2 laser delivery in the mid-IR has been investigated. As shown above, different HC-ARFs made of chalcogenide, tellurite and borosilicate glass for mid-IR transmission have been developed with different fabrication techniques, such as the stack and draw and the extrusion and draw techniques. The latter allowed Gattass et al. [34] to obtain a fibre without capillary dislocations. Despite the losses of these attempts being reasonably high (between 2 and 11 dB/m) due to some irregularities in the fibres, the feasibility of HC-ARFs for mid-IR transmission has been clearly demonstrated. As will be shown in Chapter 7, considerably better loss can be achieved in theory. Modelling suggests that loss of the order of 0.05 dB/m can be achieved in HC-ARFs at 5.4 and 10.6 μm wavelength. In this thesis, I have investigated a different fabrication approach based on extrusion and draw, because enables reduction of capillary dislocations and crystallisation problems in the fabricated fibres.

Chapter 7

HC-AR preform fabrication: materials and methods

In the first part of this chapter, the choice of the materials to develop HC-ARFs for CO and CO_2 laser radiation transmission and target HC-ARFs structures are presented. In the second part of this chapter, the fabrication method of HC-AR preforms made of tellurite and chalcogenide glass is presented. Thanks to improvements in the extrusion process, HC-AR preforms with non-touching uniform capillaries already consolidated to the jacket glass tube are obtained.

7.1   HC-ARF materials

One of the aims of this thesis is to develop HC-ARFs which transmit CO and CO_2 laser radiation (at 5.4 and 10.6 μm, respectively). The selection of the HC-ARF material is a crucial part. In fact, firstly the transmission window of the selected material and secondly its drawability into an optical fibre are the most important properties to look at. In order to transmit with low loss at wavelengths beyond 4.5 μm, soft-glasses must be used. For example, as shown in Section 3.2, tellurite, fluoride and telluride chalcogenide glasses transmit up to $\sim$6 [31], 7.5 [31] and 20 μm [31], respectively. Since only chalcogenide glass covers the CO_2 laser radiation wavelength (10.6 μm), it represents the best option for a HC-ARF for CO_2 laser delivery. The fabrication of chalcogenide HC-ARFs for CO_2 laser delivery has been investigated in this work. Chalcogenide, tellurite and fluoride glasses can be used to develop HC-ARFs for CO laser radiation (5.4 μm). Chalcogenide glass has

drawbacks such as toxicity and high cost. Tellurite glass is not toxic and has better crystallisation resistance than fluoride glass, which is critical for fibre drawing [31]. Also, the chemical durability of fluoride glasses and some chalcogenide glasses is very low [81, 82]. Tellurite glasses can be synthesised in-house in large volumes and do not require a protective atmosphere as opposed to fluoride and chalcogenide glass fabrication. For these reasons, tellurite glass was chosen to fabricate a HC-ARF transparent at a wavelength of 5.4 μm.

To protect the tellurite and chalcogenide HC-ARFs, it was decided to co-draw the glass preform with a FEP polymer tube. The FEP polymer coating gives the fabricated fibres strength, flexibility and protection from the environment. This represents a big practical advantage compared to the mostly uncoated fibres reported in the literature (which are generally very fragile as a result) [32–34, 36, 37].

7.1.1 Tellurite glass for HC-ARFs

The tellurite glass for the development of HC-ARFs transparent at 5.4 μm was chosen for its transmission window and thermal compatibility with the FEP polymer coating, in order to co-draw the glass and the polymer simultaneously. During the course of the PhD I worked with two different tellurite glasses. First, $80TeO_2 10ZnO10Na_2O$ (TZN) glass [143], which was prepared in-house by my colleague Dr Fedia Ben Slimen, was used. This was melted in a gold crucible at 900 °C for 1 hour. After casting the glass in a brass mould, it was annealed at 300 °C for 1 hour. As it will be shown later, due to crystallisation problems, this glass was replaced with a more stable glass. In particular, a tellurite glass composition of $70TeO_2 13ZnO10BaO7K_2O$ (TZBK) developed by Zhou et al. [92] was synthesised in-house by my colleague Dr Jaroslaw Cimek. This glass was melted in a gold crucible at 800 °C for 2 hours. After this time, the glass was poured into preheated brass casting form and inserted in another furnace for annealing from 300 °C to room temperature for 10 hours.

In order to understand the optical properties of these glasses, which are critical for the design and fabrication of tellurite HC-ARFs, they have been characterised. The transmission spectrum of the TZN glass was measured using a Varian 670 FTIR spectrometer on a 1.76 mm thick sample. The internal transmission of the TZN sample was then calculated by removing the Fresnel loss [144]. From the

absorbance of the sample, which can be calculated from the glass transmittance, a normalised absorbance to represent a sample with 10 mm thickness was obtained. From this, the transmission for a TZN sample 10 mm thick was obtained (black curve in Figure 7.1). This normalisation was performed to compare the TZN glass transmission with the transmission of a 10 mm thick sample of silica glass which was extracted from Ref. [145] (Figure 7.1). From this data, TZN shows good transmission up to ∼6.1 μm wavelength. Clearly, this indicates the possibility of developing a HC-ARF made of tellurite that transmits at 5.4 μm and can therefore effectively transmit CO laser light.
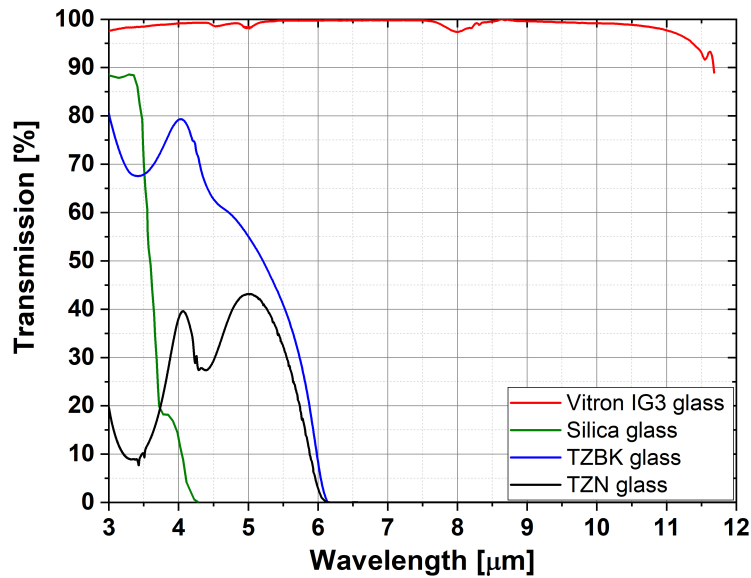
FIGURE 7.1: Transmission of TZN tellurite glass (black curve) (t = 10 mm), of TZBK glass (blue curve) (t = 10 mm), Vitron IG3 chalcogenide glass (red curve) (t = 10 mm) and silica glass (t = 10 mm) (Reproduced from Heraeus [145]).

The internal transmission of TZBK glass was determined using the same spectrometer but using a more precise method to remove the contributions of Fresnel reflection. In the case of TZN, only the Fresnel contributions due to the normal incidence were removed from the measured transmission. In the case of TZBK glass, to obtain a more accurate transmission measurement, a method which allowes removal of the contributions of the Fresnel reflection due to multiple incident angles, was used. The absorbance spectra of two TZBK samples with different thicknesses (3 mm and 15 mm) were measured. The difference between the absorbance spectra was then normalised to represent a 10 mm thick sample. From that, the internal transmission without Fresnel loss was calculated (blue curve in Figure 7.1). As

seen in Figure 7.1, the TZBK glass transmits significantly better than silica from 3.5 to 6.1 μm and has a higher transmission than TZN glass.

The refractive index of the TZN and TZBK glasses, shown as a red curve and a blue curve, respectively, in Figure 7.2, were measured by Prof. Petr Janicek on polished glass samples using a variable angle spectroscopic ellipsometer IR-VASE, J. A. Woollam Co., which covers the wavelength spectral range between 1.8 μm and 20 μm. Spectra for angles of incidence (AOI) of 55°, 60° and 65° were recorded (measuring 25 scans at 15 different compensator positions, with wavenumber steps of 8 cm-1). The backside of the samples were roughened to avoid undesirable reflection.
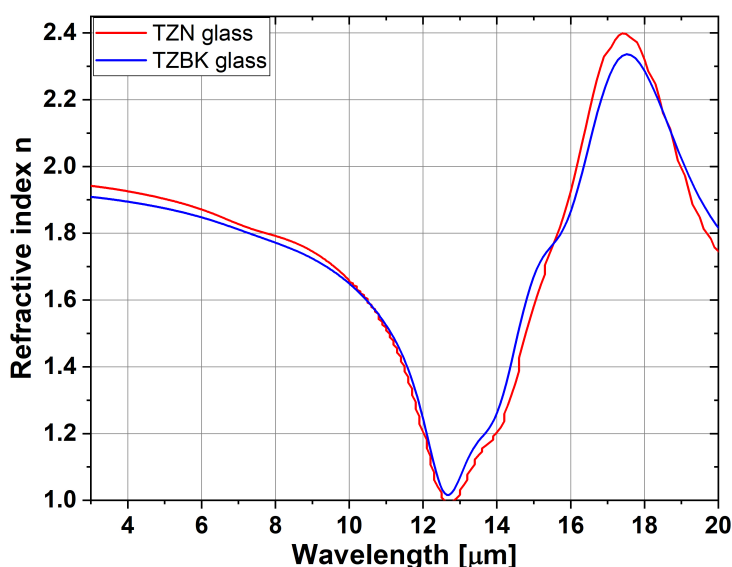
FIGURE 7.2: Refractive index of TZN glass (red curve) and of TZNK glass (blue curve).

Calorimetric measurements were performed by my colleague Dr Jaroslaw Cimek on powdered TZN and TZBK glass samples by using a PerkinElmer Diamond Thermogravimetry/Differential Thermal Analysis (TG/DTA) and they are shown shown as a black curve and red curve, respectively, in Figure 7.3. TZN glass has a glass transition temperature (T_g) of 295.2 °C. From this measurement, a peak of crystallisation was found at a temperature of 422.3 °C (black curve in Figure 7.3). As it will be shown in Chapter 8, this peak of crystallisation led to several difficulties during the first attempts at fabricating TZN tellurite HC-ARFs. In particular, it was found that the extruded preforms presented some defects and
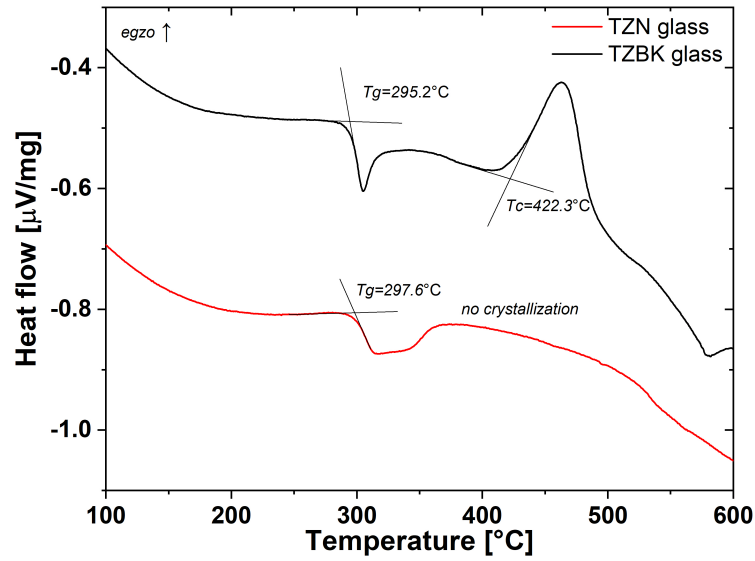
FIGURE 7.3: Differential Thermal Analysis of TZN glass (black curve) and of TZBK glass (red curve).

the fibre drawing was not stable (the capillaries break during the fibre drawing). This was probably due to the presence of crystals in the extruded preform.

TZBK glass shows a glass transition temperature (T_g) is 297.6 °C. The lack of crystallisation peak above the T_g, confirms the high thermal stability of the TZBK glass. The viscosity curve of TZBK glass has been measured by my colleague Dr Jaroslaw Cimek and it is shown as a blue curve in Figure 2.6.

7.1.2 Chalcogenide glass for HC-ARFs

To make chalcogenide HC-ARF, commercial Vitron IG3 glass, which was used as the core material of the fibre bundle (see section 4.1.1), was selected simply because of its transmission up to 12 μm and due to its thermal compatibility with the FEP polymer coating. The transmission of Vitron IG3 glass was calculated from the glass attenuation in Figure 4.1, which was obtained from a cut-back. Since Vitron IG3 chalcogenide glass transmits up to 12 μm in wavelength (red curve in Figure 7.1), it represents the best candidate for a HC-ARF for transmission at 10.6 μm (CO_2 laser).

7.2 Target tellurite HC-ARF design

In this work, the tellurite HC-ARF was designed to have low loss in the wavelength range between 5 and 6 μm, which is compatible, for example, with the delivery of CO laser radiation at 5.4 μm, and useful for material cutting, welding and surgery [1, 2]. Considering the tellurite TZN and TZBK glass refractive indexes (Figure 7.2) and Equation 6.5, a tellurite HC-ARF transmitting in the fundamental or second window would require capillaries with thicknesses below 3 μm, which is challenging at present. For this reason, it was decided to target operation in the third transmission band, which represents a good trade-off between the capillary thickness that can be achieved in the fibre draw and the spectral width of transmission band, which is reduced but still wide, as will be shown later in modelling study. Since the two tellurite glass compositions, TZN and TZBK, have a similar refractive index close to 5.4 μm, as shown in Figure 7.2, the ideal capillary thickness in the target HC-ARF, to design the fibre in antiresonance, is similar for both glasses. So, the target structure was optimised only for TZBK tellurite glass but due to the similar refractive index it works also for TZN glass.

The core diameter was designed to be larger than $\sim$20 times the wavelength in order to decrease the confinement loss of the HC-ARF. For this reason, a core diameter of 125 μm ($\sim$23 times 5.4 μm) was chosen. Since the HC-ARFs reported here consist of soft-glasses, which are more difficult to process into optical fibres compared to silica glass, the lowest number of capillaries in the fibre minimises the HC-ARF non-uniformity during the fabrication process. Also, in a HC-ARF with 6 tubes, the optimum gap between the capillaries, in order to have the lowest confinement loss, is $\sim$3 times larger than HC-ARFs with 8 and 10 tubes [134]. The possibility to have a larger gap between the capillaries makes the fibre fabrication process easier. This is because of the difficulties in the capillary pressurisation during the fibre drawing. As shown in Section 8.1, by reducing the capillary gap, there is a possibility of obtaining a HC-ARF with touching tubes, which as explained in Chapter 6, increases the confinement loss. For these reasons, the tellurite HC-ARF was designed with 6 cladding tubes with membrane thicknesses of 4.4 μm.

The transmission loss of the target tellurite HC-ARF design was studied by using a FEM simulation in Comsol Multiphysics. First, the fibre geometry was reproduced in Comsol. The real part of the refractive index of TZBK glass, as shown in Figure

7.2, was used. The imaginary part of the refractive index of TZBK glass was extrapolated from the FTIR loss measurement (blue curve in Figure 7.1). Since the glass transmission was only measurable below 6.1 μm, the imaginary part of the refractive index beyond 6.1 μm was calculated from the ellipsometry result. The two measurements agree fairly well, although a kink can be seen in the black curve in Figure 8.14 at the switch-over wavelength. To avoid reflections at the boundary of the fibre, a PML was used [69]. Since the ID of the capillaries (g) and the gap between the capillaries (z) are crucial parameters to decrease the confinement loss of the HC-ARF, a modelling study was performed to find the best z/g ratio which gives the lowest fibre loss at 5.4 μm wavelength. To do that, the core diameter and the capillary thickness were kept fixed. In this way, it is possible to understand the effect of the cladding tubes dimension/gap on the fibre loss. As shown in Figure 7.4, the minimum loss of the fibre was for z/g ratio of 0.3. Considering this, the target TZBK fibre was designed with a capillary ID of 73 μm
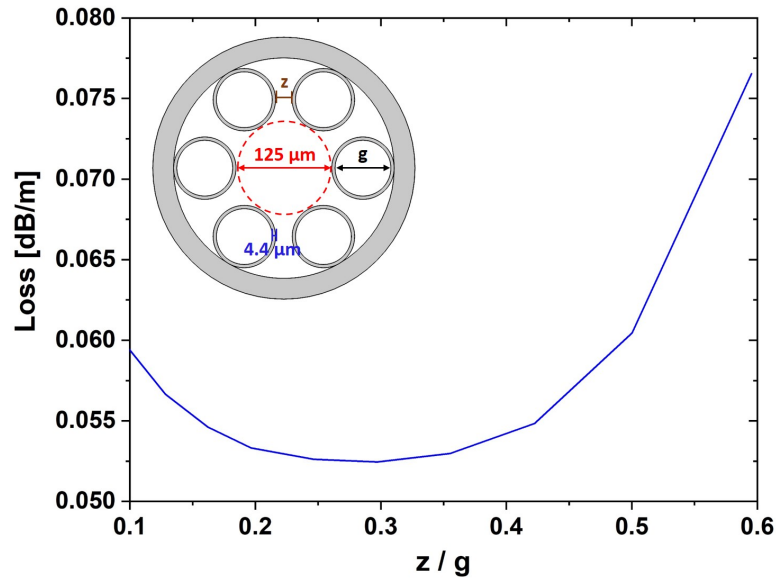
FIGURE 7.4: Simulation of the TZBK tellurite HC-ARF loss at 5.4 μm wavelength for different z/g ratios. The inset shows the design of the target TZBK tellurite HC-ARF.

and a capillary gap of 21.9 μm, as shown in the inset of Figure 7.4. The simulated loss of the target TZBK HC-ARF is shown in Figure 7.5a (solid blue curve). As it is possible to see, the target tellurite HC-ARF has a transmission band between 4.6 and 6.3 μm which represents the third antiresonant window. The graph shows that the target fibre structure has a low transmission loss of 0.05 dB/m at 5.4 μm. The confinement loss of the fibre has also been simulated (dashed green curve). It
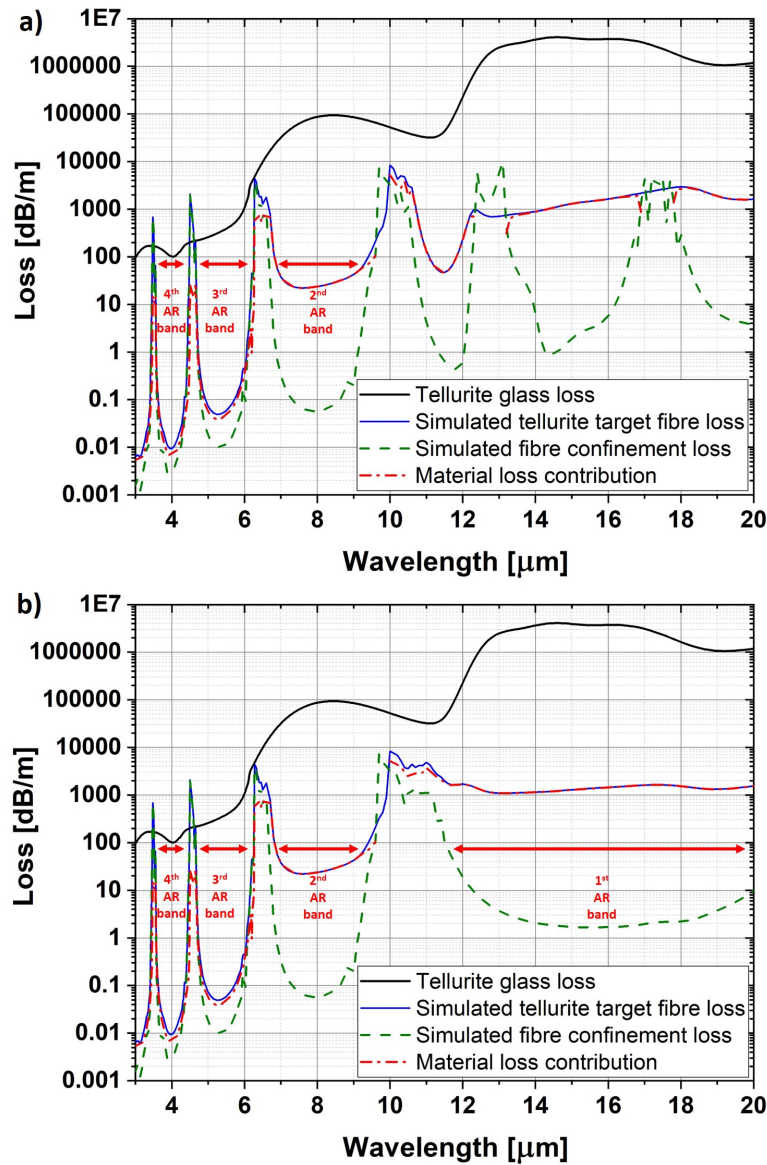
FIGURE 7.5: a) Target TZBK tellurite hollow core antiresonant fibre simulated loss (solid blue curve). The dashed green curve represents the simulated confinement loss of the target TZBK tellurite antiresonant fibre. The dash dotted red curve represents the modelling material loss contribution. The black solid curve represents the tellurite glass loss. b) target TZBK tellurite HC-ARF simulated loss by considering a constant refractive index between 10 and 20 μm.

was found that the confinement loss is 0.01 dB/m at 5.4 μm. Since this value is very low compared to the total simulated fibre loss, this explains that most of the target fibre loss is due to the material loss contribution. In fact, the calculated material loss contribution (dash dotted red curve) is close to the simulated target fibre loss (0.04 dB/m at 5.4 μm). The transmission band between 3.5 and 4.6 μm is the fourth antiresonant window, which, as expected, is narrower than the third window. The second transmission window of this HC-ARF is between 6.5 and 10 μm. The first band of transmission of the target HC-ARF was expected to be beyond 11 μm. Since the refractive index of TZBK glass has an abrupt change between 10 and 20 μm wavelength, it was not possible to notice the first transmission band of the fibre. In order to show the first transmission band of the fibre, an idealized case scenario has been studied. In particular, the TZBK refractive index has been considered constant between 10 and 20 μm (n=1.65) and the overall and confinement losses have been re-simulated (solid blue curve and dashed green curve, respectively in Figure 7.5b). In this case, as shown in Figure 7.5b, the first transmission band of the fibre is between 11 and 20 μm. As it possible to notice, the confinement loss of the target tellurite HC-ARF is of the order of 2 dB/m between 14 and 18 μm, but the overall fibre loss are higher than 1000 dB/m due to the high material loss contribution. Although this study doesn't represent the real case, it was useful to understand the effect of the material loss on the target tellurite HC-ARF. Also, Figure 7.5b shows that the fibre confinement loss at the centre of each band, increases with the wavelength increasing. This is because the confinement loss depends on the core diameter.

7.3 Target Vitron IG3 chalcogenide HC-ARF design

In order to develop a HC-ARF that is transparent for CO_2 laser radiation, as it was mentioned above, chalcogenide glass should be used. So, the target chalcogenide HC-ARF was designed in order to transmit at 10.6 μm in the fourth antiresonant band. Since the core diameter of HC-ARF for 10.6 μm should be larger than a HC-ARF for 5.4 μm, the overall dimensions of the fibre increases. In order to keep the fibre compact and flexible, the OD of the fibre should be around 500 μm (or less). For this reason, the core diameter was chosen to be ∼18 times the wavelength (190 μm). As it will be shown later in a modelling study, with

this core diameter/wavelength ratio it is still possible to achieve low transmission loss. As with the tellurite HC-ARF design, the target chalcogenide HC-ARF had 6 capillaries but they were 7.4 μm thick. The transmission loss of the target chalcogenide HC-ARF was studied using Comsol Multiphysics. In this case, the complex refractive index of the Vitron IG3 glass, shown in Figure 4.1 was used for the simulation. A modelling optimisation study was performed to select the best z/g ratio which gives the lowest fibre loss at 10.6 μm wavelength. Also in this case, as shown in Figure 7.6, the minimum loss of the fibre was for z/g ratio of 0.3. From
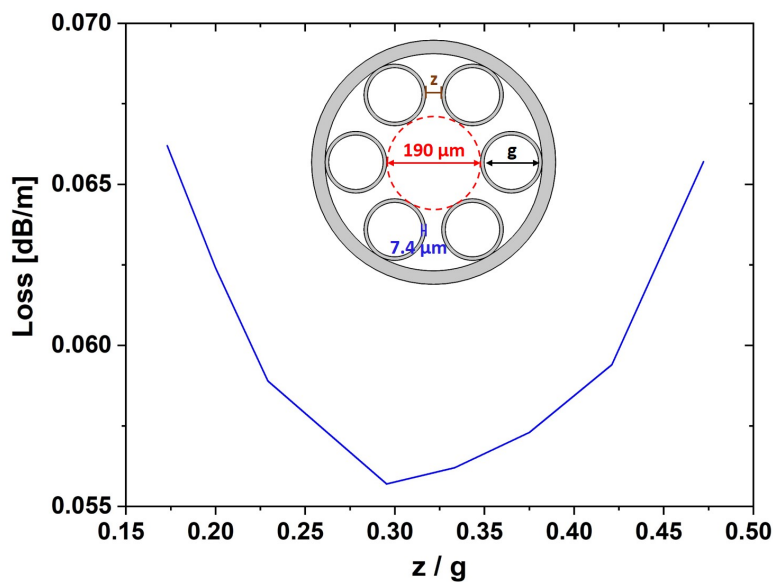
FIGURE 7.6: Simulation of the chalcogenide HC-ARF loss at 10.6 μm wavelength for different z/g ratios. The inset shows the design of the target chalcogenide HC-ARF.

this result, the chalcogenide HC-ARF was designed with capillaries of 110 μm ID and a capillary gap of 33 μm as shown in the inset of Figure 7.6. Simulations of that structure, shown in Figure 7.7, indicate that an idealised chalcogenide HC-ARF could have losses between 0.055 and 0.1 dB/m between 10 and 11 μm making the fibre suitable for CO_2 laser delivery. In this case, fibre confinement loss is close to the overall fibre loss. This means that the material loss contribution in this fibre is low.
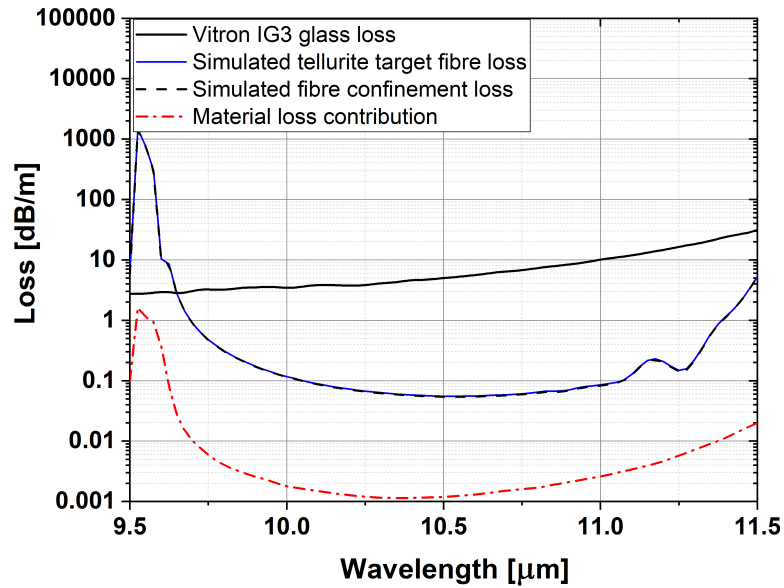
FIGURE 7.7: Target chalcogenide HC-ARF simulated loss (solid blue curve). The dashed black curve represents the simulated confinement loss of the target chalcogenide HC-ARF. The dash-dotted red curve represents the modelled material loss contribution. The black solid curve represents the tellurite glass loss.

7.4 Fabrication methods of HC-ARFs

The two main common techniques to develop HC-AR preforms are the stacking approach [146, 147] and the extrusion approach [148]. A HC-AR preform made of silica consists of several high purity silica tubes stacked inside a jacket tube [149]. The tubes are then fused to the jacket [149]. This process, and the required parameters, has been significantly developed with silica glass such that a very regular final preform can be achieved with tubes well attached to the jacket.

In the case of mid-IR glasses, the stack and draw method can be challenging due to the difficulty in producing suitable uniform and straight capillaries to stack and ensuring that the capillaries fuse in the correct location within the preform. This is due to their lower mechanical strength, steeper viscosity-temperature curves and propensity to crystallisation in processes requiring multiple re-heatings [31]. This is particularly challenging for the 'non-contact' tubes design. Additionally, fusing the capillaries to the jacket tube, which adds another thermal step for the glass preform, can increase the chance of material crystallisation.

A possible solution to these problems for mid-IR glasses is the preform extrusion technique. Extrusion has been employed in the past to develop soft-glass preforms for the fabrication of microstructured fibres such as, for example, tellurite glass

holey fibre [150] and tellurite Photonic Crystal Fibre [151]. The development a HC-AR preform made of soft-glass such as chalcogenide, which has been proposed for the first time by Gattass et al. [34], also has the advantages of design flexibility (extrusion die shape can be potentially made for many different designs, beyond restrictions imposed in the 'stacking' approach) and that the capillary elements are already fused in place. So, this technique avoids the thermal step of the capillaries consolidation which is often used for silica HC-ARFs. However, possible limitations include reduced yield, due to the length of the preform, and the risk of contaminating the glass as it moves through the extrusion die. Considering the advantages and potential drawbacks of the extrusion approach, this technique was chose to fabricate HC-AR preforms made of soft-glasses.

7.4.1   HC-AR preform extrusion

Using the extrusion process, which is shown in Section 2.2.1, glass preforms can be obtained thanks to an extrusion die that confers the shape of the die to the obtained preform. In order to obtain rods and capillaries, the extrusion die design is very simple, as shown in Section 2.2.1. In the case of HC-AR preforms, the extrusion die design is not straightforward. Moreover, the extrusion of tellurite and chalcogenide HC-AR preforms is not easy due to the presence of thin membranes. Making thin and uniform membranes is very challenging. As will be shown in this section, the design of the extrusion die is crucial for the capillaries' shape and uniformity. In this work, the tellurite TZN and the TZBK glass billets have been synthesised in-house. In contrast, the chalcogenide Vitron IG3 glass billets were provided by Vitron. Figures 7.8a, b and c show the billets of TZN glass, TZBK glass and Vitron IG3 glass, respectively; these are the starting material for the extrusion process. Since tellurite glass is less expensive than IG3 glass and also tellurite glass can be synthesised in-house, in the first extrusion trials tellurite glass was mainly used. In this way, once the extrusion process and the extrusion die design were optimised, it was possible to move to chalcogenide glass. Another advantage of using tellurite glass for the first extrusion trials is that a recipe to clean the extrusion die from the residues of glass in the inner part of the die was developed. This recipe involved boiling the extrusion die in an aqueous solution of Nitric acid (20% HNO_3) and water for 6 hours. This cleaning process, reduced the costs and the time related to the die fabrication thanks to the ability to re-use of the same die. Unfortunately, this cleaning procedure of the extrusion die was
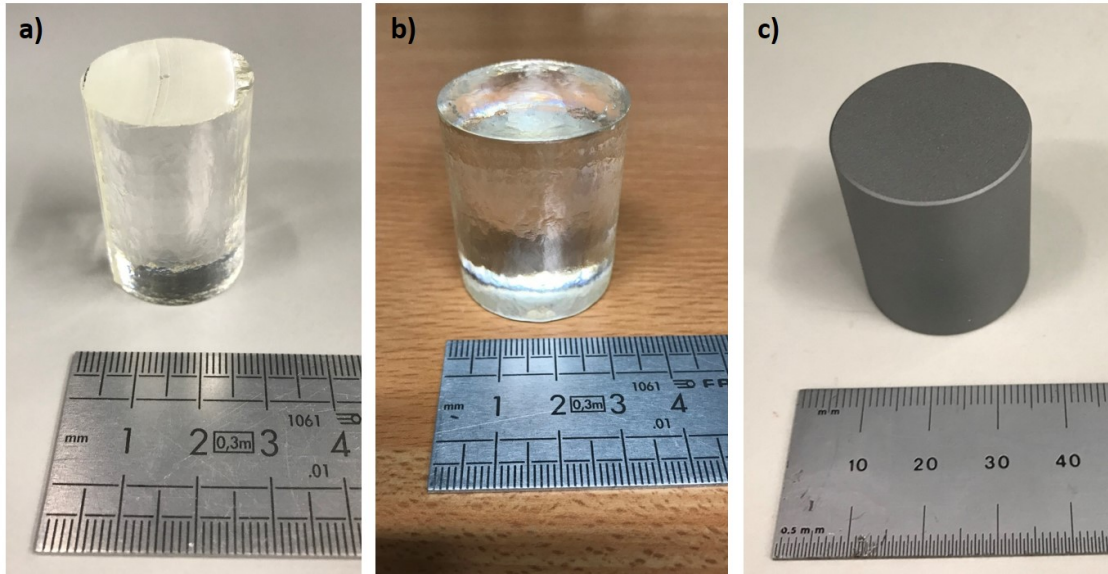
FIGURE 7.8: a) TZN glass billet, b) TZBK glass billet and c) Vitron IG3 chalcogenide glass billet.

not applicable in the case of chalcogenide glass extrusion because of the toxicity of the glass.

7.4.2 Machined complex die

The design of the extrusion die in order to make a HC-AR preform with non-touching capillaries is not straightforward. In particular, different extrusion dies made of stainless steel 316 were designed. These were fabricated in the workshop of the University of Southampton. Stainless steel 316 is quite common as material of extrusion dies because it is easy to machine and cheap. As part of this thesis, several different designs were produced and tested to inform the subsequent design modifications. Here the extrusion die design evolution is described in detail.

The first design of the die consisted of two main parts: one is the base of the die with 6 pins screwed in (Figure 7.9a) and the second one is the ring die (Figure 7.9b). Their assembly is shown in Figure 7.9c (machined complex die A). In particular, the die has 6 pins since the target HC-ARF was designed and modelled in Comsol in order to have 6 capillaries. The machined complex die A was designed to produce a preform with a jacket glass tube of 13.3 and 15 mm ID and OD, respectively, and a capillary thickness of 300 μm (Figure 7.10a).

This extrusion die was tested by extruding an IG3 glass billet. As mentioned in Chapter 3, the load, speed and temperature of extrusion are key parameters for
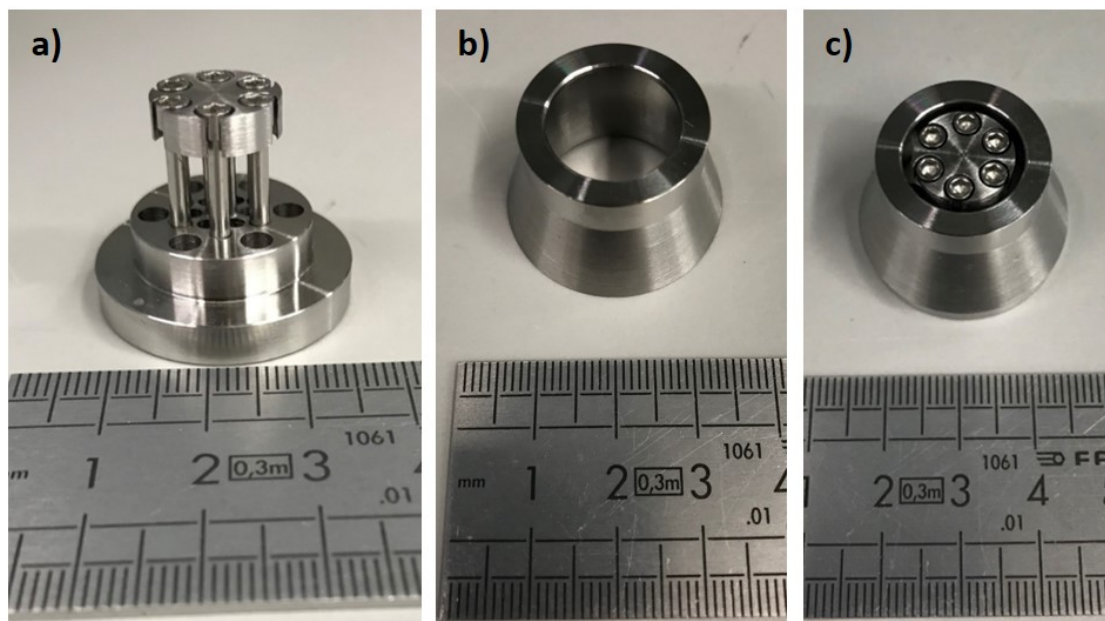
FIGURE 7.9: a) Base of the complex die with the 6 screwed pins, b) ring die and c) assembled complex die.

the extrusion process. In the case of chalcogenide glass, a low extrusion speed and a high load was applied to the billet. This is because the Vitron IG3 billet was processed at high viscosity (low temperature). The billet, 32 mm OD and 36 mm in length, was extruded through this extrusion die at 341 °C at a speed of 0.04 mm/min. The extrusion load was ∼26 kN. The cross-section of the 23.5 cm long extruded preform is shown in Figure 7.10b. As it is possible to see from the cross-section of the preform, the capillaries of the preform were too thin and they were broken along the preform. The jacket of the preform had a 13 mm ID and 15.7 mm OD.

Since the capillaries in the preform were too thin, the gap between the capillary elements in the extrusion die was increased to 600 μm in order to improve the glass flow around the pins of the die and make the capillaries thicker and more robust. In addition to this, the jacket gap was decreased in the extrusion die to constrain the glass flow for the jacket and then improve the glass flow around the pins. In fact, the machined extrusion die B was designed to have a preform of 13.3 mm and 14.3 mm ID and OD (Figure 7.10c).

From the machined extrusion die B, a billet of IG3 glass was extruded at 353 °C at a speed of 0.04 mm/min. The extrusion load was ∼26 kN. Figure 7.10d shows the cross-section of the extruded preform (26 cm long). It is possible to see that the jacket was not circular, probably because the jacket gap in the extrusion die
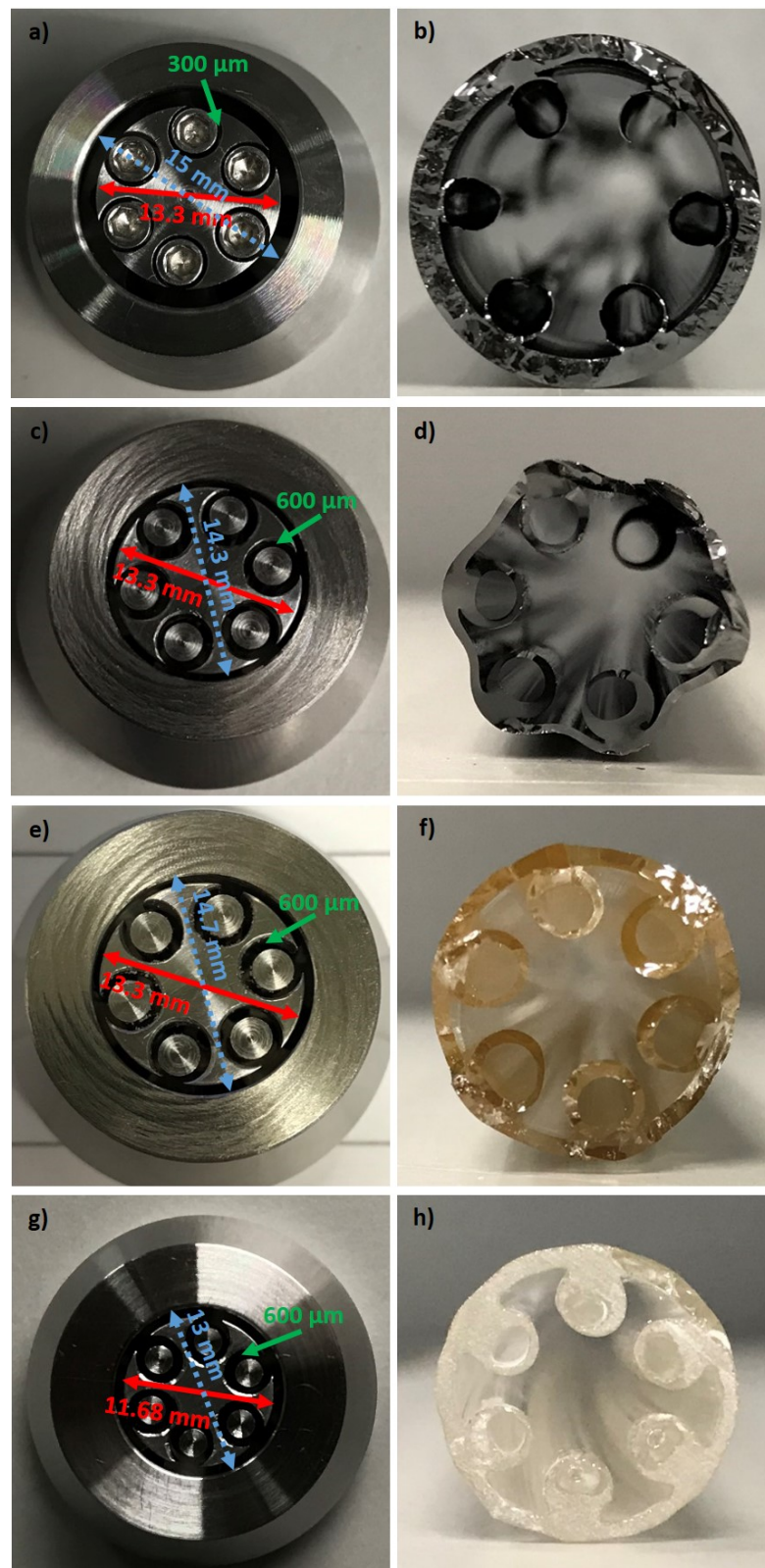
FIGURE 7.10: Machined complex dies: A (a), B (c), C (e), D (g), and cross-section of HC-AR preforms extruded from die A (b), B (d), C (f) and D (h).

was too small. In this case, the preform had 6 capillaries with a thickness between 0.7 and 0.87 mm.

Since the capillaries were not broken along the preform, only the ring die was then modified. In particular, to make the jacket circular, a ring die with a bigger hole was then used. The new ring die had a hole of 14.7 mm as shown in Figure 7.10e (machined extrusion die C). A TZN tellurite glass billet was extruded through this complex die at 327 °C at a speed of 0.05 mm/min. The extrusion load was ∼8 kN. The extrusion load was lower than the chalcogenide billet extrusion. This is because the viscosity of tellurite billet was lower than the chalcogenide one. As it is possible to see from Figure 7.10f, the preform, which was 17 cm long, had a circular jacket. The OD of the preform was 14.98 mm.

Since tellurite and chalcogenide glasses are fragile, several tubes of FEP polymer can be added to the preform in order to protect the final fibre made of these glasses. As mentioned above, this polymer, which is thermally compatible with both tellurite and chalcogenide glasses, enables a flexible and a mechanically strong fibre, thanks to its low Young's modulus. One of the limitations of this approach is the increase in the OD of the final preform. This is because the dimensions of the drawing tower furnace are limited. To accommodate a thicker layer of FEP polymer, the extrusion die was re-designed in order to decrease the dimensions of the glass preform. In particular, the die was re-designed to have a preform with an OD of 13 mm as shown in Figure 7.10g (machined extrusion die D). The capillaries in the extrusion die were 2.2 mm ID and 3.4 mm OD. A TZN tellurite glass billet was extruded through this extrusion die at a temperature of 334 °C. The extrusion speed and load were 0.28 mm/min and ∼26 kN, respectively. A preform that was 21 cm long was obtained. As shown in Figure 7.10h, the capillaries were not broken along the preform. The OD and the ID of the preform were 13.4 mm and 11.6 mm, respectively.

Although this extrusion die design enabled fabrication of a preform with 6 capillaries, it had some limitations. The die consisted of 6 pins that are screwed on the base of the extrusion die. Since each part of the die was fabricated mechanically, machining tolerances lead to different physical dimensions of different parts. For this reason, for each pin and each hole on the base of the die the resulting glass flow could be different from the others. In addition to this, the screwed pins are not well centred to the hole on the base of the die as shown in Figure 7.10g. These

irregularities in the machined extrusion die, introduce non-uniformities in the preform and in the capillaries as shown in the previous extrusion attempts. These non-uniformities in the preforms are critical for the fabricated fibre because different thicknesses in the capillary membranes in the fibre have different resonances, making the resultant fibre more lossy. In other words, by having different capillary thicknesses in the fibre structure, the resonance wavelengths are closer. This makes the antiresonant bands very narrow. For this reason, since by machining the extrusion die the fabrication tolerance is not small, a more precise method to fabricate the complex die was employed.

7.4.3 Spark corroded complex die

In order to overcome the non-uniformity problems, a new complex die was designed and fabricated. This new die consisted of two parts: the base of the die in which 6 pins are already embedded and a ring die. The key difference was that the base of the die is fabricated by spark corrosion. During spark corrosion, a carefully designed mask is positioned on the top surface of the base of the extrusion die. The base of the spark corroded die (spark corroded die E) is shown in Figure 7.11a. In this way, the extrusion die has 6 pins which are already embedded to the base of the die and consists of just one single piece. This minimises the manufacturing tolerances of each pin of the die. Figure 7.11b shows the base of the complex die E assembled with a ring die. The holes for the glass flow on the top side of the base of the die are shown in Figure 7.11c. The central hole (6 mm diameter) is for the capillary glass flow. The section of the spark corroded complex die E is shown in Figure 7.11d. As shown in Figure 7.12a, the spark corroded complex die E was designed to have a preform with capillaries 600 μm thick and a jacket of 13.6 and 11.68 mm OD and ID, respectively.

From this spark corroded die (E), a TZBK glass billet was extruded at 335 °C. The extrusion speed and load were 0.5 mm/min and ~8 kN, respectively. The extrusion load was lower than in the case of the machined complex die D because the design of spark corroded die improved the glass flow. Figure 7.13a shows the cross-section of the extruded tellurite preform. By comparing the spark corroded die and the extruded preform, it is clear that the jacket is hexagonal and the capillaries are smaller compared to the extrusion die. This is due to the glass surface tension when the glass preform comes out from the hot extrusion die. Although the jacket is
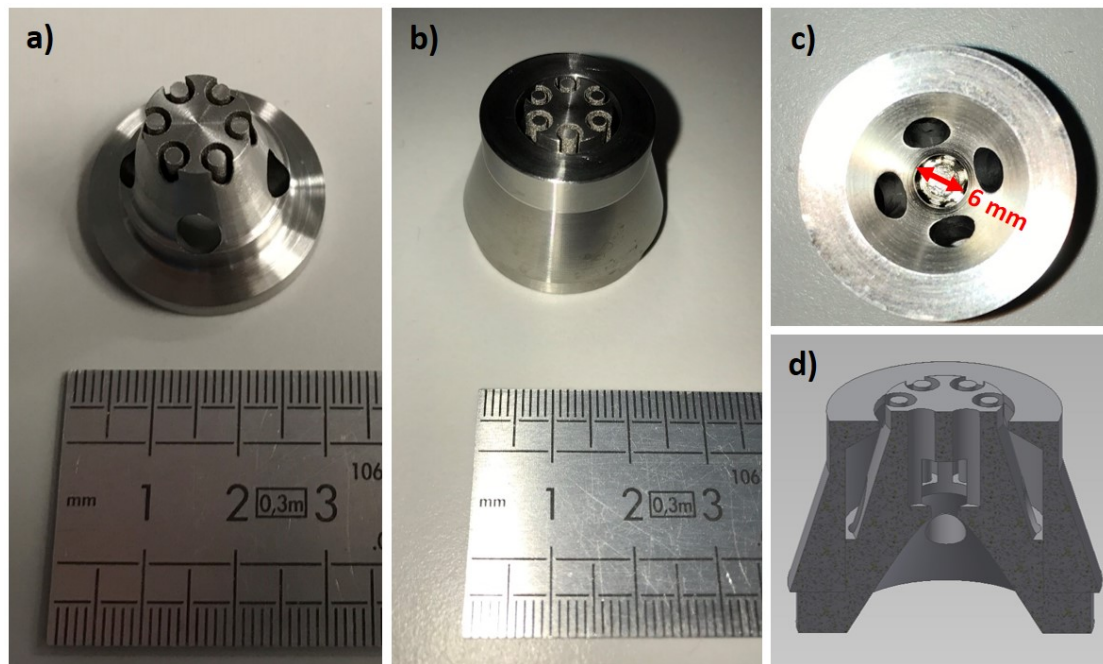
FIGURE 7.11: a) Base of the complex die E with the spark corroded pins, b) assembled spark corroded complex die E, c) holes for the glass flow on the base of the die and d) section of the spark corroded die E.
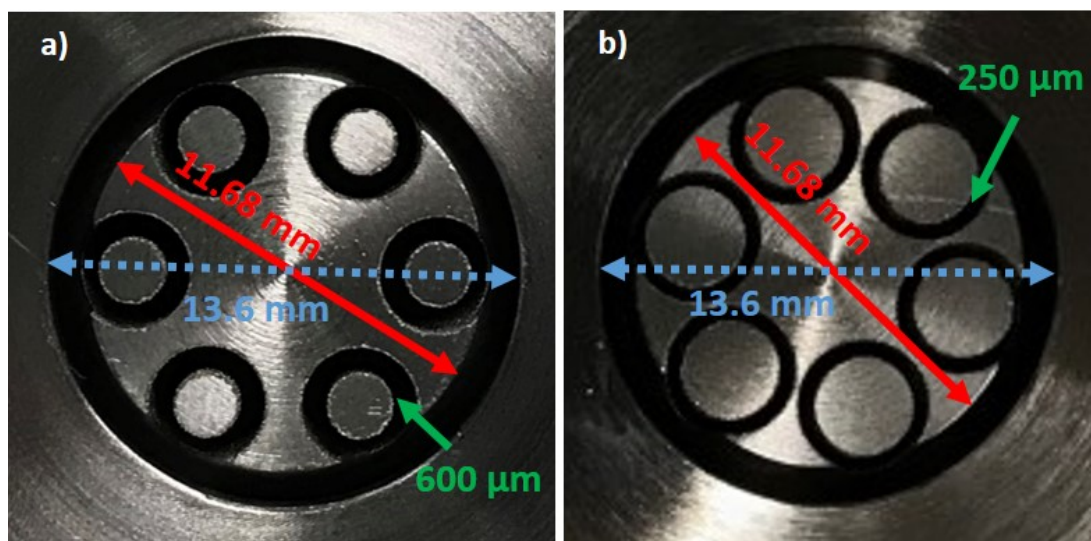
FIGURE 7.12: a) Spark corroded complex die E and b) spark corroded complex die F.
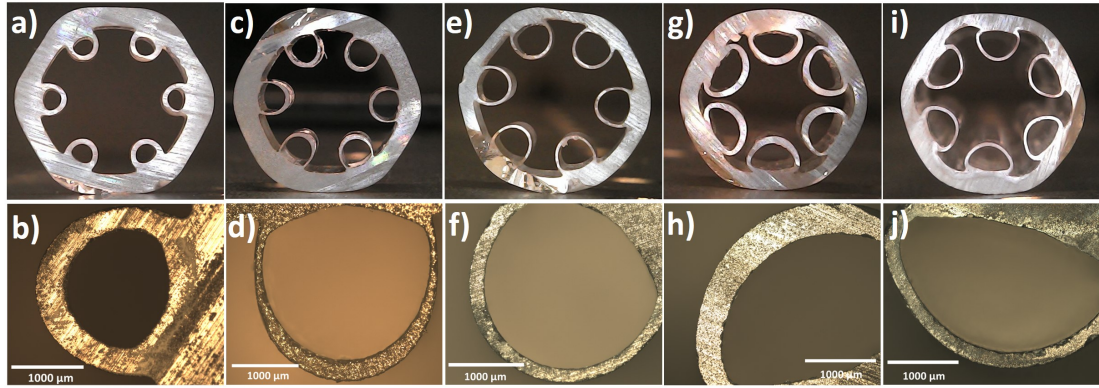
FIGURE 7.13: a) Preform extruded from the spark corroded die E and b) micrograph of one capillary. c), e), g) and i) Preforms extruded through the spark corroded die F and d), f), h) and j) micrographs of their capillaries.

not circular, as it is possible to see, the capillaries are circular and their thickness is almost constant across the capillaries radius as shown in Figure 7.13b. The capillary thicknesses are 403.9 ± 36.5 μm. This represents a huge improvement in comparison with the previous extrusion. The spark corroded die E significantly reduced the uniformities in the die and in the extruded preform.

As the capillaries in the preforms need to be pressurised during the fibre drawing, as it will be shown later, a preform with thinner and bigger capillaries is more closely related to the target fibre structure and it makes the fibre fabrication easier [152]. This allows an increase in the usable length of the preform and a subsequent increase in the length of the fibre produced. For this reason, a new spark corroded die (spark corroded die F) with thinner and bigger capillaries was designed and fabricated. The die was designed to have a preform with capillaries of 250 μm thickness and a jacket of 13.6 and 11.68 mm of OD and ID, respectively. Figure 7.12b shows the top view of the complex spark corroded die F with its dimensions. The base of the spark corroded die F is shown in Figure 7.14a. Figure 7.14b shows the base of the extrusion die F assembled with the ring die. The holes for the glass flow on the base of the die are shown in Figure 7.14c. Figure 7.14d shows the section of the spark corroded extrusion die F. The ring die was 0.5 mm lower than the base of the die as shown in Figure 7.15a.

From this spark corroded die (F), a TZBK tellurite glass billet was extruded at 336 °C at a speed of 0.15 mm/min. The extrusion load was of $\sim$12 kN. Figure 7.13c shows the cross-section of the extruded tellurite preform.
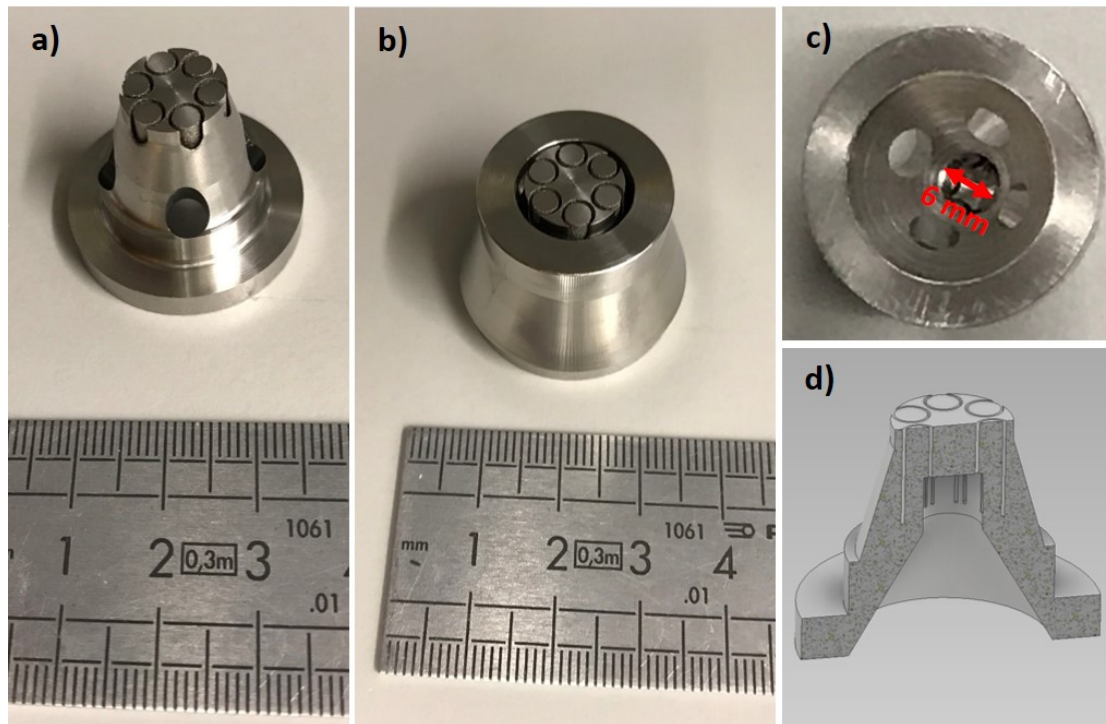
FIGURE 7.14: a) Base of the complex die F with the spark corroded pins, b) assembled spark corroded complex die F, c) holes for the glass flow on the base of the die and d) section of the spark corroded die F.
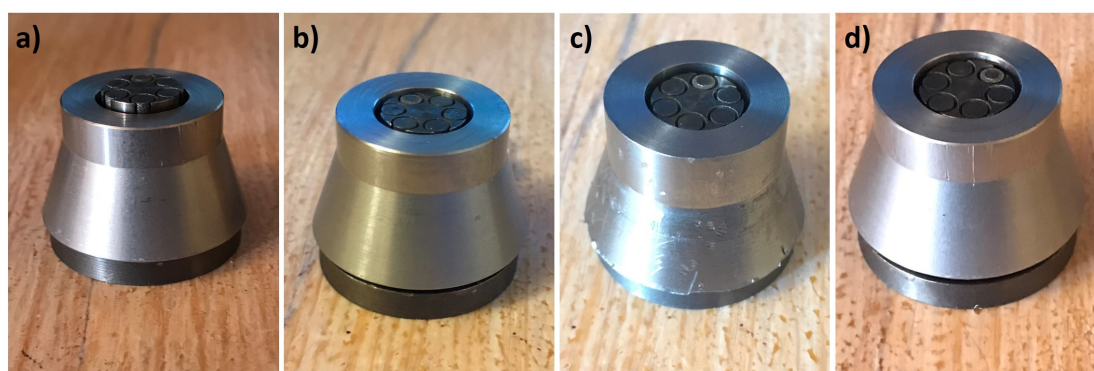
FIGURE 7.15: Different complex die configurations: a) ring die 0.5 mm lower than the base of the die , b) ring die 0.5 mm higher than the base of the die, c) ring die 1.2mm higher than the base of the die and d) ring die 0.95 mm higher than the base of the die.

As it is possible to notice, the jacket of the preform has a hexagonal shape and the capillaries are bigger in OD and thinner than the previous extruded preform. The capillary thicknesses are not constant across their radius. In fact, they are thicker at the centre and thinner closer to the jacket as shown in Figure 7.13d. The average thickness of the capillaries was 210 ± 97 μm. The thickness at the centre of the capillaries was almost 3 times than that of the sides of the capillaries. The reason of these non-uniformities is the glass flow in spark corroded die. To overcome this problem, several changes have been made on the spark corroded die F.

In particular, the central hole for the capillaries glass flow, shown in Figure 7.14c, has been increased from 6 to 6.2 mm. During several extrusion trials, it was found that the position of the ring die affects both the shape and the thickness uniformity of the extruded preform. By placing the ring die at a higher level of the base of the die, the glass flow for the jacket is constrained. This improves both the glass flow around the capillaries and avoids the jacket expansion at the exit of the extrusion die, which is the cause of the large capillary gap in the preform. In absence of a modelling study of the extrusion process, the position of the ring die was tuned by performing extrusion trials. In fact, the ring die was positioned 0.5 mm higher than the base of the die as shown in Figure 7.15b. Another tellurite TZBK billet was extruded through this modified spark corroded die F at 336 °C at a speed of 0.15 mm/min. The extrusion load was ∼12 kN. The section of the preform is shown in Figure 7.13e. The ID and OD of the extruded preform were 11.36 and 13.61 mm, respectively. As it is possible to see from Figure 7.13f, the uniformity of the capillaries was improved. The average thickness of the capillaries was 203.3 $\pm$ 28.94 μm. The variation around the average capillary thickness decreased.

Since the distance between the capillaries in the preform is still high compared to the gap between the capillaries on the complex die F, a further change in the extrusion die was made. In fact, the ring die was positioned 1.2 mm higher than the base of the die as shown in Figure 7.15c. Moreover, a new ring die of 13 mm OD was used. A TZBK tellurite glass billet was then extruded at 336 °C at a speed of 0.15 mm/min. The extrusion load was ∼12 kN. The extruded preform is shown in Figure 7.13g. The ID and OD of the extruded preform were 11.09 and 13.18 mm, respectively. In this preform, the gap between the capillaries is smaller compared to the previous extrusion, but they are not circular and also the

thickness of the capillaries (399.9 ± 82.6 μm) is not constant as shown in Figure 7.13h. For this reason, the ring die position was changed again.

In fact, the ring die was placed 0.95 mm higher than the base of the die as shown in Figure 7.15d. Another TZBK tellurite glass billet was extruded at 340 °C at a speed of 0.15 mm/min. The extrusion load was ∼6 kN. In this case the extrusion load was lower than previously because the temperature of the billet was higher and then the glass was more viscous. Figure 7.13i shows the section of the extruded preform. The extruded preform had an ID of 11.08 and an OD of 13.3 mm. The capillary thickness was 228 ± 13 μm. This die configuration seems to be the best trade-off between the thickness uniformity of the capillaries and the gap between the capillaries. In fact, the thickness of the capillaries is constant and the gaps between the capillaries are small, as shown in Figure 7.13j. Although the shape of the capillaries is not circular and their distance is not the same as the extrusion die, this is not a limitation since the capillaries are pressurised during the fibre drawing. In fact, by applying pressure into the capillaries, they expand and they become circular. Also, the gap between the capillaries decreases.

Figure 7.16 shows a summary of the extrusion trials. The picture shows the improvements that have been achieved in terms of shape and uniformity in thickness of the capillaries.
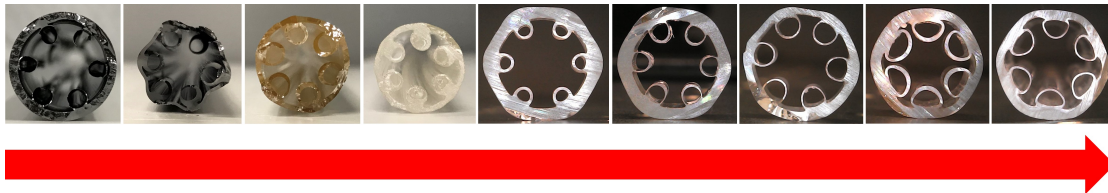
FIGURE 7.16: HC-AR preform extrusion progress

A summary of the dimensions of the extruded preforms is reported in Figure 7.17.

In the next chapter, the fabrication of different HC-ARFs made of tellurite and chalcogenide glass, will be shown. The problems encountered during the first fibre drawing trials, such as capillary breakage and non-uniformity in the capillary expansion will be shown and the solutions to these problems will be discussed.

Extruded Preform									
OD (mm)	15.7	-	14.98	13.4	14.6	14.5	13.61	13.18	13.3
ID (mm)	13	-	13	11.6	11	11	11.36	11.09	11.08
Capillary thickness (μm)	-	700÷870	280÷850	300÷700	403.9±36.5	210±97	203.3±28.94	399.9±82.6	228±13
Extrusion die	Machined A	Machined B	Machined C	Machined D	Machined E	Machined F	Machined F	Machined F	Machined F
Note	Circular jacket; broken capillaries	Non-circular jacket; Non-uniform capillaries	Circular jacket; non-uniform capillaries	Circular jacket; non-uniform capillaries	Hexagonal jacket; uniform capillaries	Hexagonal jacket; non-uniform capillaries	Hexagonal jacket; uniform capillaries	Hexagonal jacket; non-uniform capillaries	Hexagonal jacket; uniform capillaries

FIGURE 7.17: HC-AR preforms dimensions

7.5 Conclusions

The fabrication of soft-glass HC-AR preforms by extrusion process has been presented. The extrusion of the preform gives the advantage to obtain a preform which is already consolidated. Moreover, the step of consolidation of the capillaries with the jacket is not needed. This minimises the chance of glass crystallisation. Despite these advantages, the extrusion process needs optimisation. In this chapter, improvements to the extrusion die have been demonstrated. A preform with uniform capillaries has been obtained which opens up the possibility to fabricate uniform HC-ARFs. In the next chapter, the HC-ARF drawing is presented.

Chapter 8

Tellurite and chalcogenide HC-ARFs for mid-IR laser delivery

In this chapter the fabrication of tellurite and chalcogenide HC-ARFs for mid-IR laser delivery, fabricated through the extrusion and draw method is presented. In the first part of the chapter, following the description of the pressurisation system used in this work to expand the fibre capillaries, the fabrication of HC-ARFs made of TZN tellurite glass is reported. Due to crystallisation problems, the TZN glass was replaced with another tellurite glass composition developed-in-house by a colleague in my group made of $70TeO_213ZnO10BaO7K_2O$ (TZBK) which proved thermally more stable. The second part of the chapter shows the fabrication of tellurite HC-ARFs with this new glass composition. The fibres were co-drawn with a FEP polymer coating for enhanced mechanical strength. The last part of this chapter presents the fabrication of a chalcogenide HC-ARF, which, as mentioned in Chapter 7, could be useful for CO_2 laser delivery at 10.6 μm. Moreover, in this chapter, FEM simulations using Comsol have been performed on the fabricated HC-ARFs to estimate their loss and understand the road for improvements. The refractive indices and the transmission spectrum of Vitron IG3 and TZBK glass, which are shown in Chapter 3 and in Chapter 7, were useful to perform the FEM simulations of the fabricated fibre structure.

8.1 HC-ARF pressurisation during fibre drawing

The pressurisation system shown in Figure 8.1 [141, 153], consists of two chambers which enable application of different pressures (P_{core} and $P_{cladding}$) into the core and into the capillaries. By applying pressure into the capillaries, it is possible
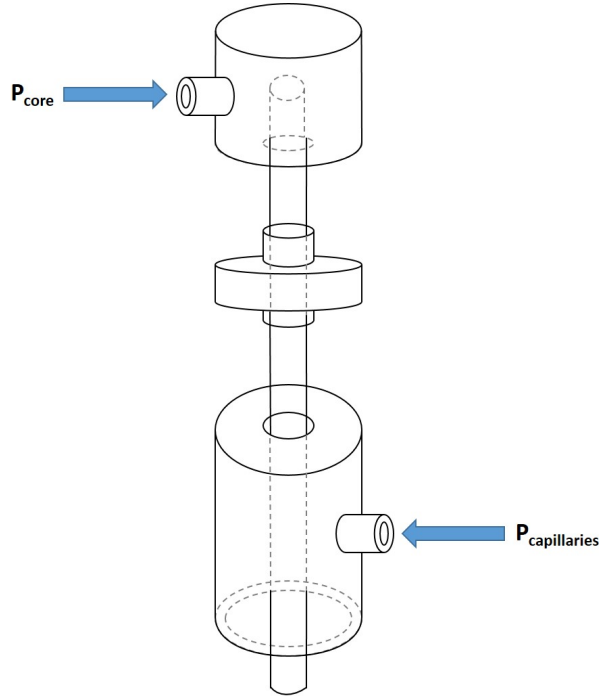
FIGURE 8.1: HC-ARF pressurisation system [153].

to obtain the desired capillary thickness and dimensions during the fibre draw. By optimizing the pressure into the core and into the capillaries, it is possible to improve the gap between the capillaries and the core dimension [154]. Controlling the balance between the surface tension and pressure with soft-glasses is more challenging compared to silica glass because of their steeper viscosity curve as shown in Figure 2.4. In this work, due to the short preforms compared to the silica HC-AR preforms, to minimise the parameters that need to be optimised during the fibre drawing, only pressure in the capillaries $P_{cladding}$ was applied, keeping the core at atmospheric pressure.

The pressurisation system that I developed for this work is shown in Figure 8.2a. A stainless steel tube, 65 cm long with a pipe weld on the side (Figure 8.2a), was fabricated in the local workshop. The top side of the tube represents the pressurisation region (Figure 8.2b). Figure 8.2c shows the preform with a borosilicate

capillary glued in the core. In particular, a silicone glue (RS) was applied only into the core region without closing the preform capillaries. The silicone consisted of two components: an activator and a silicone. By mixing the two parts, the silicone glue was obtained. After the glue was hardened (~12 hours), about 1 cm of the preform was inserted inside the pressurisation tube (Figure 8.2d). The borosilicate capillary, which is glued into the core region, was longer than the pressurisation tube. In fact, it was out of the pressurisation tube (Figure 8.2e). Figure 8.2f shows the pressurisation tube with the preform placed in the drawing tower. In this work, the borosilicate capillary was left open to keep the core at atmospheric pressure and a pressurisation tube was connected to the weld pipe on the side of the stainless steel tube in order to pressurise the capillaries of the preform. This simple system was efficient for capillary pressurisation during the fibre drawing.
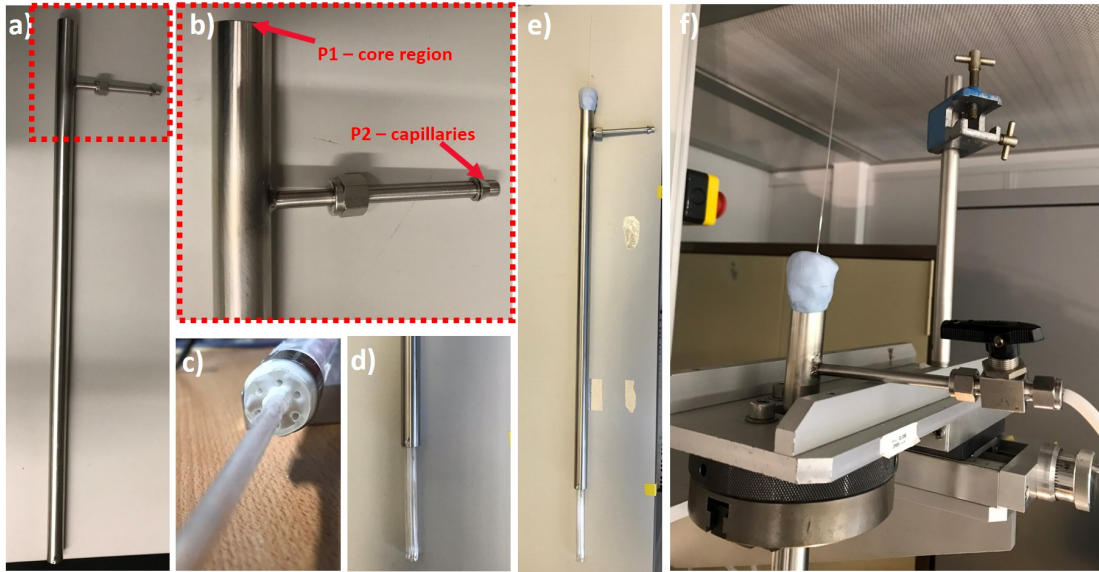
FIGURE 8.2: a) Stainless steel pressurisation tube, b) zoom of the top side of the pressurisation tube, c) glued preform with the borosilicate capillary into the core, d) bottom side of the stainless steel tube with the extruded preform, e) pressurisation tube with the extruded preform and f) pressurisation system in the drawing tower.

Figure 8.3 shows an example of the effect of increasing pressure in the capillaries during the fabrication of a tellurite TZBK HC-ARF. The tellurite TZBK HC-ARFs shown in Figure 8.3a, b and c were obtained by applying 5.1, 5.3 and 5.4 mbar of pressure, respectively, into the capillaries. As it is possible to notice, by increasing the pressure $P_{cladding}$ at some point the capillaries will get in contact. Finding the maximum pressure possible before tube contact was one of the challenges of this work, due to the short preform size and available draw time (~1.5 hours).

In the next sections, different HC-ARFs made of tellurite and chalcogenide glass,
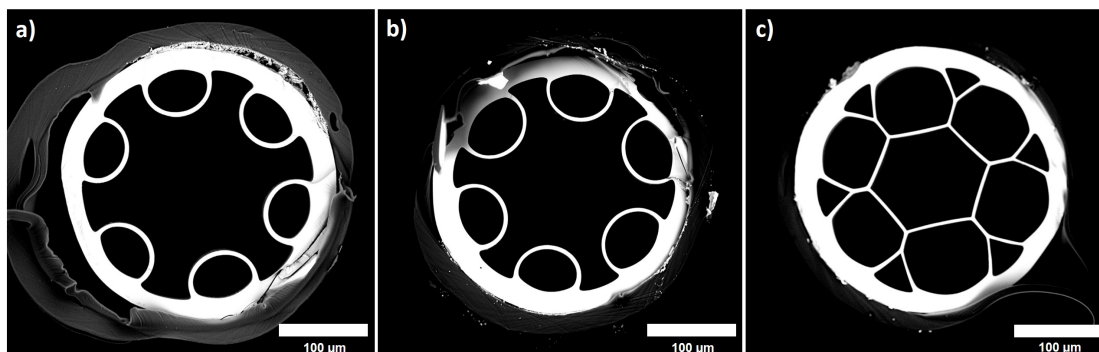
FIGURE 8.3: Tellurite TZBK HC-ARFs fabricated by applying (a) 5.1, (b) 5.3 and (c) 5.4 mbar of pressure in the capillaries and by keeping the core region at atmospheric pressure.

which were fabricated with different pressures applied in the capillaries will be shown. The pressurisation problems encountered during fibre drawing will be discussed.

8.2 TZN HC-ARF fabrication through the machined complex die and characterisation

As mentioned in the previous chapter, the machined complex die, which consists of several pins screwed on the base of the die, has large fabrication tolerances. These, as shown in Figure 7.10, led to non-uniformities in the assembled machined complex die. Despite these non-uniformites of the extrusion complex die, several extrusions and subsequent fibre draws were performed. This was part of the optimisation process of the extrusion parameters such as load, temperature, extrusion speed and also of the fibre draw parameters.

8.2.1 TZN tellurite HC-ARF fabrication

A tellurite TZN HC-AR preform was fabricated by using a tellurite TZN glass billet of 28 mm in diameter and 70 mm of height through the machined complex die D shown in Figure 7.10g. The cross-section of the extruded tellurite preform is shown in Figure 8.4a; the preform OD was 13.9 mm and the usable length was 40 cm. From Figure 8.4a, it is possible to notice that the extrusion process

enabled a symmetric structure, with the capillary elements well fused in place and a consistent azimuthal distribution. Unfortunately, the capillaries within the preform were not uniform (their thickness ranged from 170 to 539 μm), which is not ideal. The preform was then drawn into a fibre at 350 °C. During the fibre drawing, the core was kept at atmospheric pressure, while the pressure applied into the capillaries was changed to improve the fibre structure. The fibres shown in the SEM pictures of Figures 8.4b, c and d, were drawn with no pressure, 11 mbar and 12 mbar of pressure into the capillaries, respectively. As expected, the capillaries' non-uniformities from the preform are also present in the fibres.
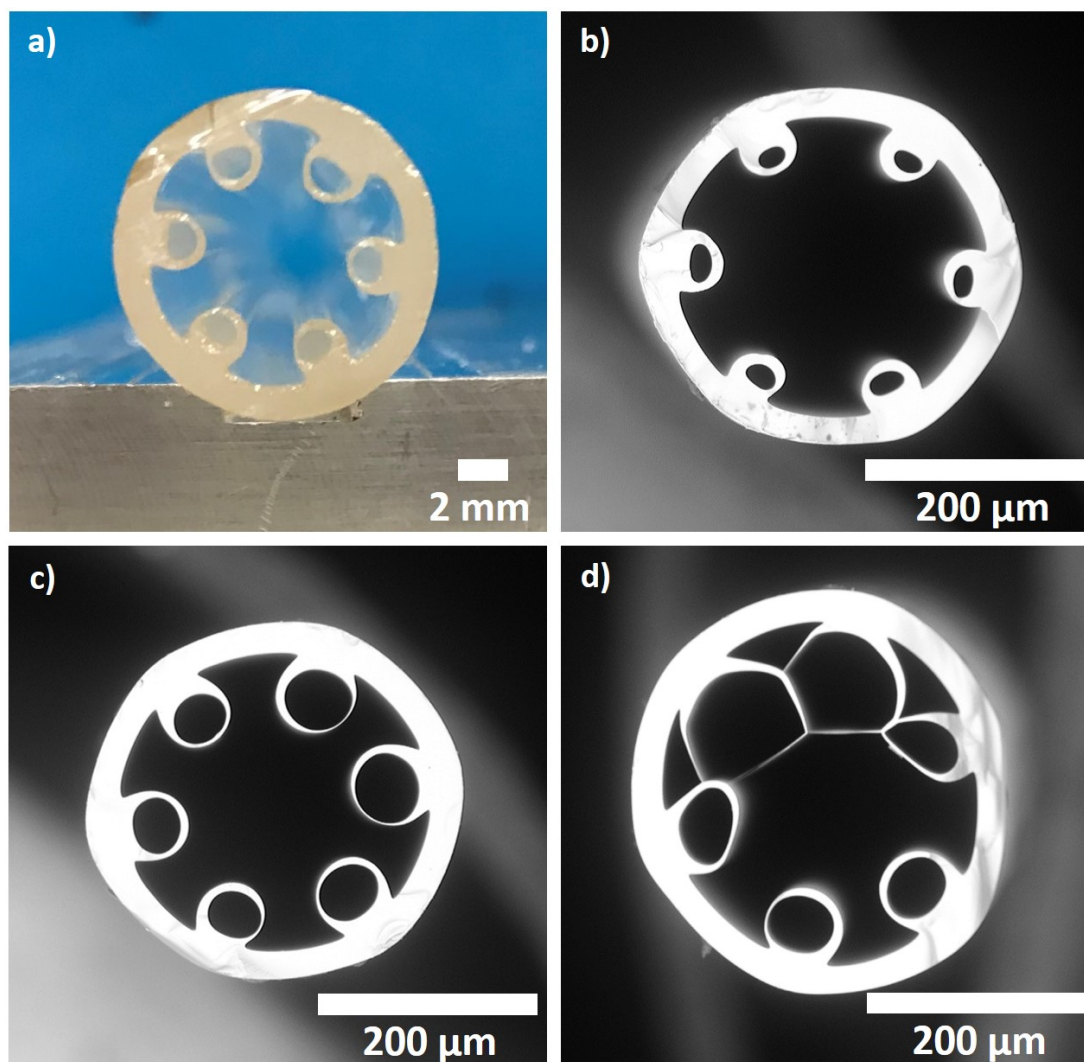
FIGURE 8.4: a) Cross-section of the tellurite TZN extruded preform. Tellurite HC-ARFs fabricated by applying: b) no pressure, c) 11 mbar and d) 12 mbar of pressure into the capillaries.

8.2.2   TZN tellurite HC-ARF characterisation

The TZN HC-ARF of Figure 8.4c was then characterised. The structural parameters were measured from SEM images; the core diameter and OD of the fibre of Figure 8.4d were 152 and 350 μm, respectively. Due to the fibre non-uniformity, which increases the confinement loss, only 20 cm length of fibre was optically characterised. A Thorlabs SLS202L lamp, which was already described in Section 4.1.1, was used to launch light into the fibre core. At the output of the fibre, a Xenics Onca MWIR 320 thermal camera, described in Section 5.2, was used for detection. The inset of Figure 8.5 shows an image at the output of the fibre recorded by the camera, and clearly shows light confined in the core region. The attenuation of this fabricated TZN HC-ARF was simulated using Comsol. The real fibre structure was reproduced from the SEM picture of the fibre (Figure 8.4d) using an image analysis software which my colleague Dr Greg Jasion developed and it was imported into Comsol. To perform the fibre loss simulation, the real and imaginary part of refractive indices in function of the wavelength of TZN glass were imported in Comsol. In particular, the real part is shown as a red curve in Figure 7.2. Instead, the imaginary part was calculated from the glass transmission spectra (black curve in Figure 7.1). The real and imaginary part of the glass refractive indices were assigned to the glass region in the imported fibre structure. In the air regions of the imported fibre structure the real and imaginary refractive indices of air were assigned. In particular, they were 1 and 0, respectively. The simulated loss is shown as a solid black curve in Figure 8.5.

The simulated loss increases with wavelength and does not show any sign of the expected antiresonant bands because the non-uniformities in the thickness of the capillaries cause an overlap of adjacent antiresonant transmission windows. In the wavelength range from 4.5 to 5 μm, the simulated loss is between 30 and 49 dB/m. A cut-back measurement (from 20 cm to 16 cm) was performed, again using the tungsten filament as a light source but using the same ARCoptix FT-IR spectrometer described in Section 4.1.1 for detection. In particular, it was found that connecting the fibre directly to the light source was the best way to launch light into the fibre. For this reason, the TZN HC-ARF was connected to the light source and to the FTIR using a FC/PC and a SMA connector, respectively.

The measurement was only possible (i.e. there was detectable signal at the receiver) at the peak of the source's blackbody emission, between 2.25 and 2.8 μm.
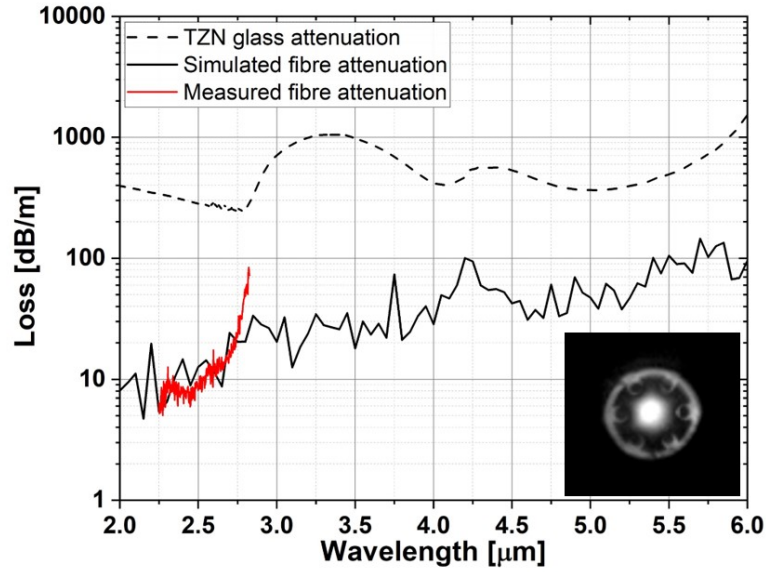
FIGURE 8.5: TZN tellurite HC-ARF simulated loss (solid black curve). The red solid curve represents the TZN tellurite HC-ARF loss measured by using FTIR spectrometer. The black dashed curve represents the TZN tellurite glass loss.

Here the fibre loss was comparable to the simulation and reached a minimum of 6 dB/m at 2.3 μm (solid red curve of Figure 8.5). Although the fibre loss is high, this first fibre demonstrated the applicability of the fabrication process to TZN tellurite glass and that this-non-toxic and durable glass can be made into a HC-ARF. However, this glass and the machined extrusion die have limitations such as crystallisation and irregularities as discussed in the following Section.

8.2.3   Machined extrusion die and TZN tellurite glass limitations

As shown above, the machined extrusion die led to a preform (and subsequently fibre) with non-uniformities and irregularities. As shown in the fabricated fibre of Figure 8.5a, the simulated fibre loss does not show any antiresonant transmission bands due to the fibre irregularities. To reduce these non-uniformities, a new complex die was designed and fabricated with a different fabrication method. As discussed in Chapter 7, the new die was fabricated by spark corrosion which enables a smaller fabrication tolerance compared to the machined complex die. Moreover, TZN tellurite glass presents a crystallisation peak in the TG/DTA curve (see Section 7.1). This represents a limitation for the fabrication process of TZN tellurite

HC-ARF. In fact, the presence of crystals in the preform could cause breakage of the capillary. An example of this occurance is shown in Figure 8.6. For this
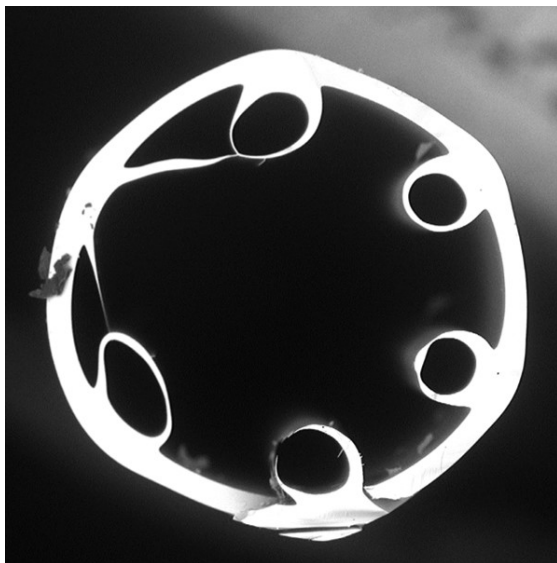
FIGURE 8.6: Tellurite HC-ARF with a broken capillary due to presence of crystals into the preform.

reason, during the course of the project, the TZN tellurite glass was replaced with a more thermally stable tellurite glass (TZBK glass). This new glass composition does not have any crystallisation peaks as shown in Section 7.1.

8.3   TZBK HC-ARF fabrication through the spark corroded complex die E

A TZBK glass billet was extruded through the spark corroded complex die E, shown in Figure 7.12a. The cross-section of the extruded preform is shown in Figure 8.7a. The 35 cm long preform was straight and free of defects. The ID and OD of the preform were 11 and 14.6 mm, respectively. The average capillary thickness was 403.9 ± 36.5 μm.

The preform was inserted in a FEP polymer tube with 15 mm ID and 17 mm OD, and the preform and FEP polymer tube were co-drawn into a fibre at 350 °C. During the draw, the core was left at atmospheric pressure and the pressure applied into the capillaries was altered during the draw. Figures 8.7b, c, d and e show the SEM pictures of the fabricated TZBK tellurite HC-ARFs by applying 11, 12, 13 and 14 mbar of pressure into the capillaries. As it is possible to see
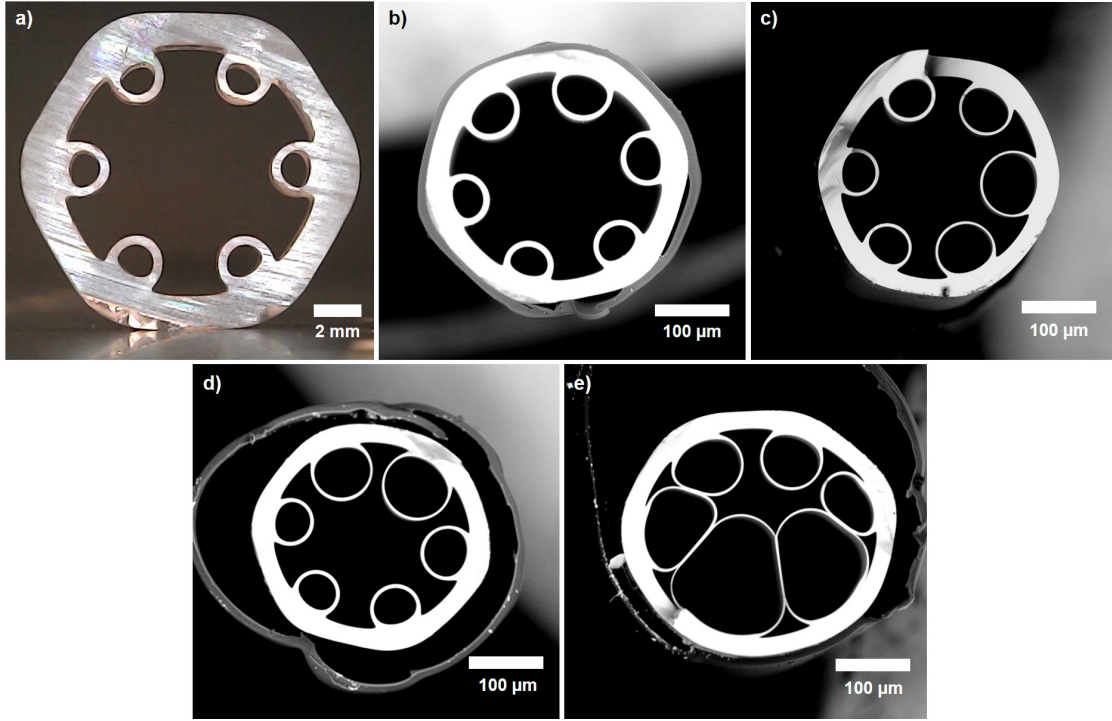
FIGURE 8.7: TZBK tellurite HC-ARFs fabricated by applying: b) 11 mbar, c) 12 mbar, d) 13 mbar and e) 14 mbar into the capillaries.

from the fabricated fibres, the capillaries were not responding uniformly with the increasing pressure. From a post fabrication analysis, I concluded that this was likely due to the fact that the preform was not well-centred in the furnace of the drawing tower. For this, one side of the preform was hotter than the other side. So, the capillaries in the hotter side of the preform expanded more than those in the colder side. By improving the centring of the preform in the furnace of the drawing tower, the capillaries should expand more uniformly (only limited by the capillary uniformity in the initial preform). Furthermore, from the images in Figures 8.7c and d, it is clear that the FEP polymer is not well contacted with the fibre. This is because some of the pressure applied into the capillaries went between the glass preform and the FEP polymer tube. By improving the gluing step, this unintended expansion of the polymer can be avoided.

A second TZBK tellurite glass preform, extruded at the same conditions of the previous one in Figure 8.7a, was then co-drawn, again with FEP polymer coating. In this case, a more uniform fibre (Figure 8.8) was obtained thanks to a better alignment of the preform in the furnace. The pressure applied into the capillaries during the draw was 14 mbar. The fibre had an OD and a core diameter of $\sim$390 μm and 165 μm, respectively. The thickness of the capillaries was 4.55 $\pm$

0.18 μm. This variation around the capillary thickness has been estimated by using an image analysis software which my colleague Dr Greg Jasion developed. This fibre was the best fabricated from a tellurite extruded preform; the several
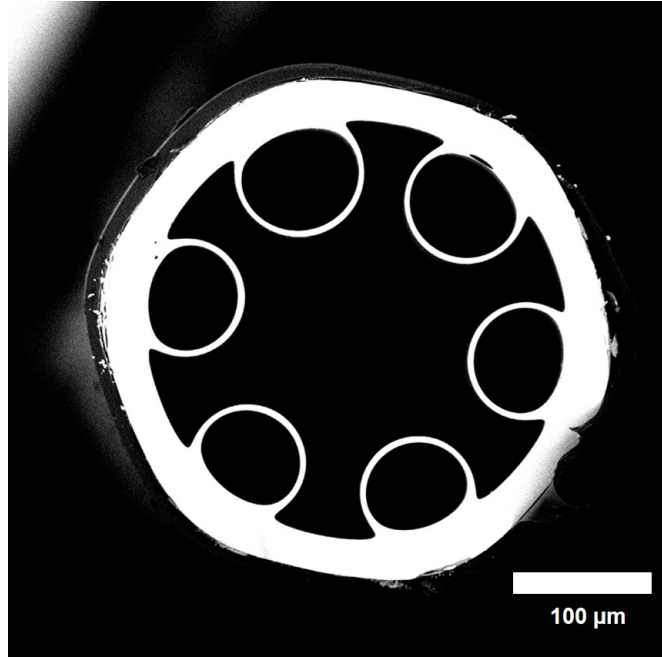
FIGURE 8.8: TZBK HC-ARF fabricated by applying 14 mbar of pressure into the capillaries.

optimisations performed on the glass composition, the extrusion die and the fibre drawing facility were fundamental in achieving this fibre structure. The fibre was then thoroughly characterised, as reported below.

8.3.1 TZBK tellurite HC-ARF characterisation

The TZBK HC-ARF fabricated through the first spark corroded die, shown in Figure 8.8, has been characterised. In particular, to measure the loss of the fibre, two different cut-backs were performed. In the first one, which was performed by using a FTIR spectrometer, the transmission of 22.5 cm of HC-ARF was measured and then cut-back to 9 cm (1 cut). The measured loss was between 20 and 100 dB/m in the 4.85 - 5.4 μm wavelength range (solid green curve in Figure 8.10a).

In order to try to obtain a more accurate loss measurement, an alternative optical source was used. Infrared light from an Optical Parameter Oscillator (OPO) with a good beam profile (close to a Gaussian beam) [155] was coupled using a ZnSe lens with a focal length of 50 mm, into the input of a 30 cm long fibre (see Figure

8.9). This lens was chosen because it allowed a spot size slightly smaller than the mode field diameter of the fundamental mode. In particular, the mode field diameter of this fibre was estimated in Comsol and it was $\sim$103 μm, while the spot size after the lens was $\sim$94 μm at 5.2 μm. The OPO was tuned sequentially

FIGURE 8.9: Cut-back measurement setup using an OPO.

to 4.9, 5 and 5.2 μm. As shown in Figure 8.9, the output power was measured using a power meter. The fibre loss, including the coupling loss, by considering the output/input power ratio, was estimated to be 45.9, 16.1 and 14.44 dB/m at 4.9, 5 and 5.2 μm, respectively (squared black dots in Figure 8.10a). These losses are lower than those measured using the FTIR. This indicates that by using the OPO, most of the light was launched into the fundamental mode. In contrast, by using the wideband light source, it was more difficult to obtain a good launch at all wavelengths and several high order and lossier propagation modes were excited.

From the SEM picture of the fabricated TZBK HC-ARF (Figure 8.8), the real fibre structure was reproduced (Figure 8.10b) as explained in Section 8.2.2. The contours of the reproduced fibre structure agree well with the SEM picture of the fibre as shown in Figure 8.10b. The real and imaginary part of the TZBK glass and air were assigned to the glass and air regions of the imported fibre structure. From simulations, this fibre was predicted to have loss between 0.35 and 124 dB/m between 4.9 and 6 μm with the minimum loss at 5.75 μm (red solid curve of Figure 8.10). As it is possible to see from Figure 8.10a, the fibre shows a transmission band (third transmission band) which is centred at 5.75 μm. This means that, according to Equation 6.5, by reducing further the thickness of the capillaries in the fibre, it would be possible to have low loss of the order of 0.35 dB/m at the wavelength where a CO laser operates (5.4 μm). The confinement loss of the fibre has been also simulated by setting the material absorption to zero and it is shown as a dashed black curve in Figure 8.10a. It is clear that the confinement loss and the fibre loss including the material absorption are close. By subtracting the confinement loss to the overall fibre loss, the material absorption contribution has been calculated (solid blue curve of Figure 8.10a). This is lower than the confinement loss. So, the TZBK HC-ARF losses are dominated by confinement loss. This contrasts with the
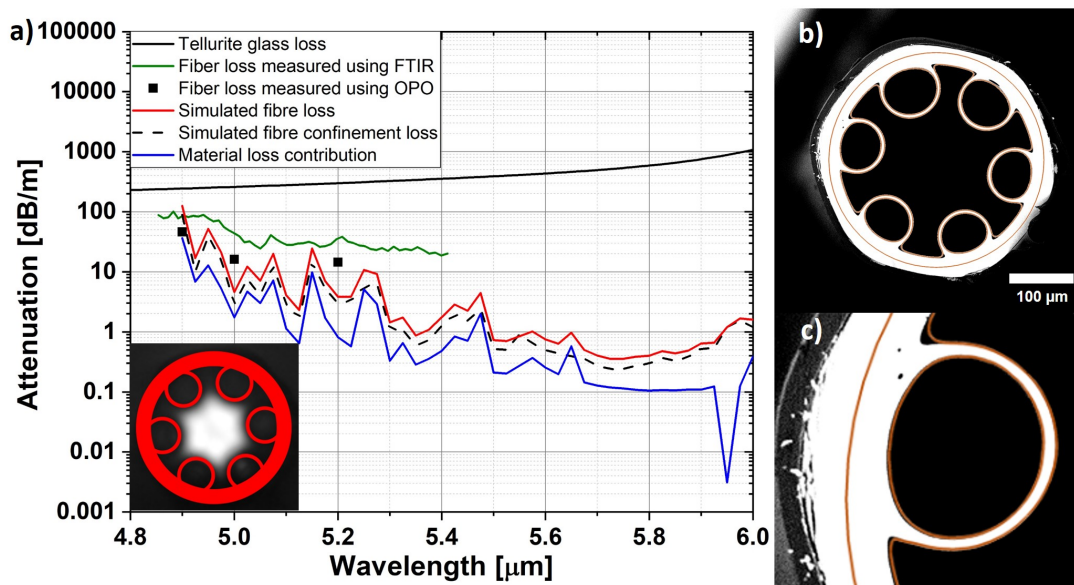
FIGURE 8.10: a) Fibre loss measured using FTIR (solid green curve), fibre loss measured using OPO (black squared dots), simulated fibre loss (red solid curve), simulated confinement loss (dashed black curve) and material loss contribution (solid blue curve). The inset shows the output of the fibre when the Thorlabs light source was coupled into the fibre. In b) the contours of the fibre used for simulation are shown. In c) a zoom on a capillary is shown where it is possible to notice the agreement between the contours and the SEM picture.

target TZBK fibre structure, where the confinement loss is the lowest contribution on the straight fibre loss (see Figure 7.5) and demonstrates that the uniformity of the fibre and of the capillaries' shape is essential to minimise the confinement loss.

8.3.2 Limitations of the spark corroded extrusion die E

The spark corroded die E allowed me to obtain the first uniform TZBK tellurite HC-ARF. However, this die design has a limitation. This is due to the small OD and the large thickness of the capillaries in the preform. As mentioned in Section 7.4.3, a preform with thinner and bigger capillaries simplifies the fibre fabrication process because the preform is closer to the target fibre structure. Also, the preforms extruded from this complex die (E), have capillaries with a large standard deviation. As shown in Figure 8.11, by expanding the capillaries in the fibre, their non-uniformities are more accentuated. For this reason, a second spark corroded die (spark corroded die F) was designed to have thinner capillaries with a larger OD compared to the spark corroded die E.
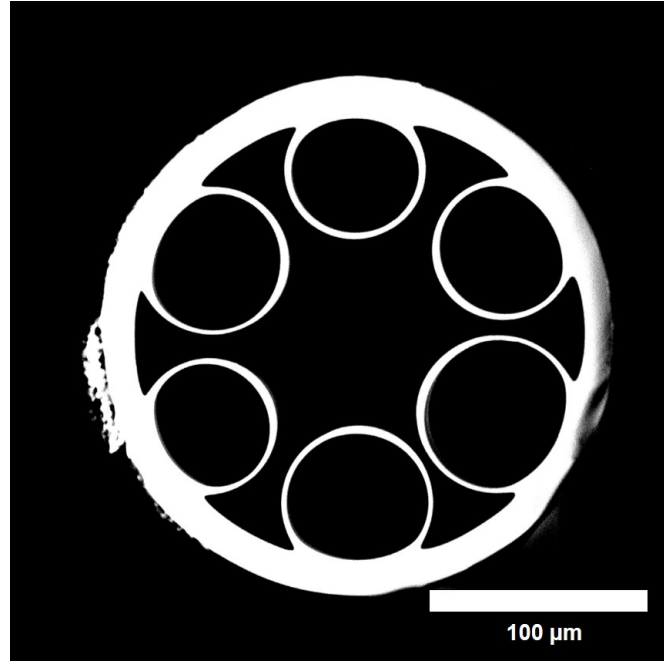
FIGURE 8.11: Capillary thickness non-uniformity.

8.4 TZBK HC-ARF fabrication through the spark corroded complex die F

The spark corroded extrusion die F (Figure 7.12b), had 6 non-touching circular tubes of 3.68 mm OD and 250 μm thickness. From this die, I extruded an in house-made TZBK tellurite glass billet. The cross-section of the extruded preform is shown in Figure 8.12a. The preform, which was 20 cm long, was straight and free of any defect or sign of crystallisation. The ID and OD of the preform were 11.08 and 13.3 mm, respectively. The average capillary thickness was 228 ± 13 μm. As it can be seen, due to surface tension effects, the capillaries are not completely circular and the preform has a hexagonal shape.

The preform was inserted in a FEP polymer tube with 15 mm ID and 17 mm OD, and the preform and the FEP polymer tube were co-drawn into a fibre at 350 °C. Figure 8.12b shows a SEM picture of a tellurite HC-ARF fabricated by applying 6 mbar of pressure into the capillaries (Fibre A). The fibres shown in Figures 8.12c, d, e, f, g and h, were fabricated by me from another preform which was extruded at the same conditions of the one in Figure 8.12a, by applying 4.7 (Fibre B), 5 (Fibre C), 5.1 (Fibre D), 5.2 (Fibre E), 5.3 (Fibre F) and 5.4 (Fibre G) mbar of pressure into the capillaries, respectively.
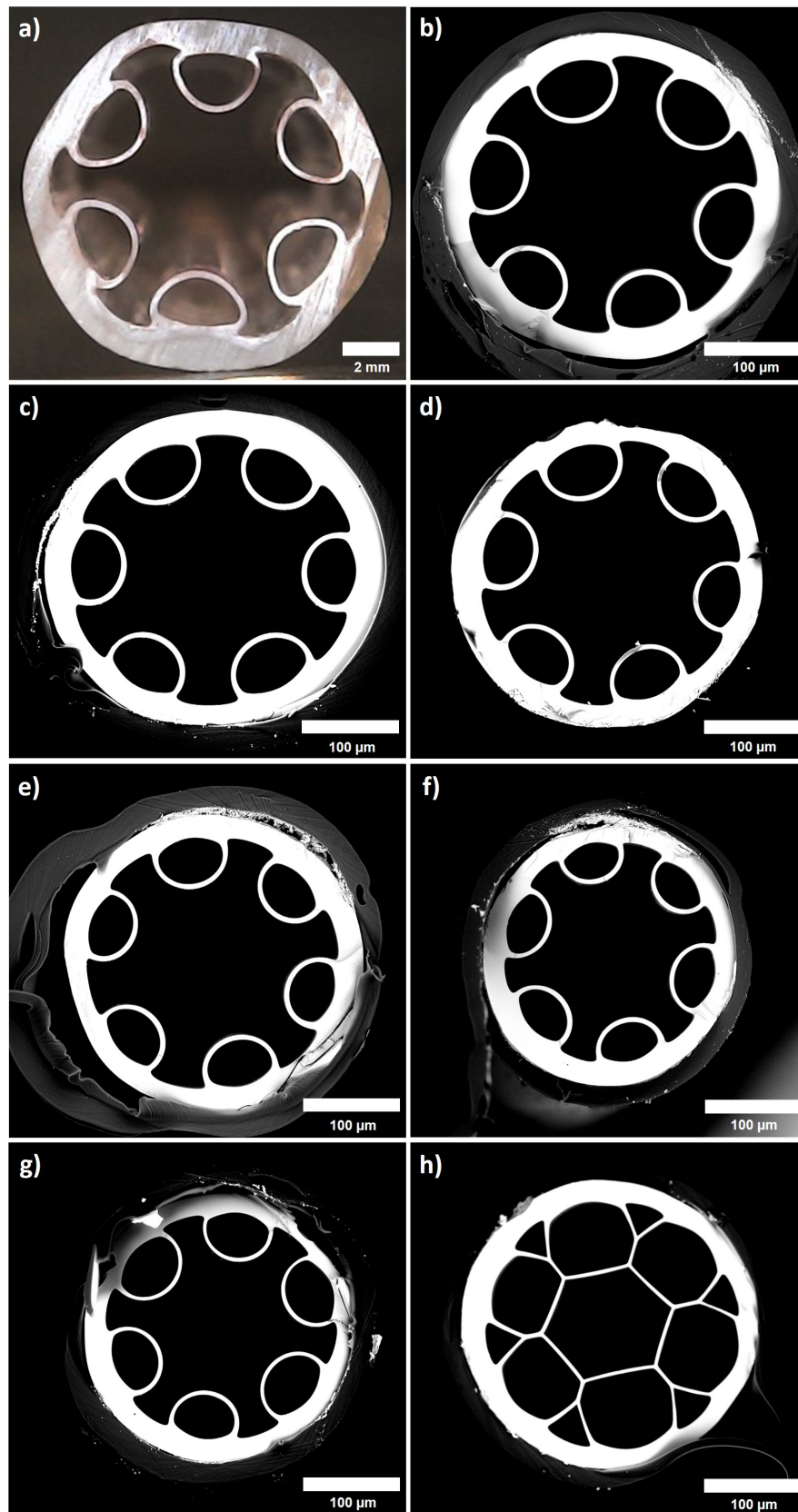
FIGURE 8.12: a) Extruded tellurite preform. SEM pictures of TZBK HC-ARF developed by applying (b) 6 mbar (Fibre A), (c) 4.7 mbar (Fibre B), (d) 5 mbar (Fibre C), (e) 5.1 mbar (Fibre D), (f) 5.2 mbar (Fibre E), (g) 5.3 mbar (Fibre F) and (h) 5.4 mbar (Fibre G) of pressure into the capillaries.

Table 8.13 shows the core dimension, the capillary thickness, the OD and the length of the TZBK HC-ARFs reported in Figure 8.12. The pressures applied during the fibre draw are also shown in the table. As it is possible to notice from this table, from a single draw, I obtained more than 70 m of fibre. Having short preforms of about 20-40 cm in length, this fibre length is good, considering that the first part of the preform is used for the neck down, part of the preform is used for the pressure optimisation and the last part of the preform is not drawable. Moreover, by looking at Fibre C, Fibre D, Fibre E, Fibre F and Fibre G, which have a similar OD, by increasing pressure applied into the capillaries, the core diameter decreases and the capillaries thickness decreases. Only Fibre D does not follow the capillaries decreasing trend with the pressure increasing. This is probably due to a small variation in the extruded preform or to the variation around the average capillary thickness. The latter variation was between 0.2 and 0.3 μm. Fibre F has the closest dimensions to the target fibre structure which had a core diameter of 126 μm and a capillary thickness of 4.4 μm. In order to investigate the loss of these fibres, I performed FEM simulations.

8.4.1 TZBK tellurite HC-ARFs simulation

The losses of the fabricated tellurite HC-ARFs have been studied with FEM simulations. Also in this case the real fibre structure was extrapolated from the SEM picture of the fibres and the real and imaginary part of refractive index of the TZBK glass and air were assigned to the glass and air region as described in Section 8.2.2. The simulated total loss (i.e. confinement plus glass absorption contribution) of the fabricated fibres is shown in Figure 8.14.

Although the fabricated fibres in Figure 8.12 transmit at different wavelength ranges, it is possible to see that a transmission loss lower than 10 dB/m between 4.6 and 6.7 μm is predicted. In particular, Fibre D has simulated loss of $\sim$2 dB/m in the 4.7-4.85 μm and in the 6.2-6.5 μm spectral range (solid blue curve of Figure 8.14). Fibre A has the lowest loss close to 5 μm compared to the other fabricated fibres. In fact, it has a predicted loss of 1.9 dB/m at 4.97 μm (dotted brown curve of Figure 8.14). The only fibre which transmits between 5.5 and 6 μm wavelength is Fibre E. It has loss between 2.4 and 3 dB/m in the 5.6-5.75 μm wavelength range (dashed blue curve of Figure 8.14).
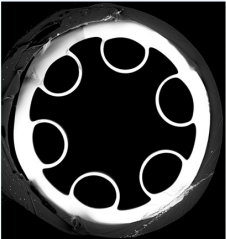
Fibre name	Fibre picture	Pressure into the capillaries (mbar)	Pressure into the core (mbar)	OD (µm)	Core diameter (µm)	Capillaries thickness (µm)	Length (m)
Fibre A		6	Atmospheric	400	187	5.7±0.3	9
Fibre B		4.7	Atmospheric	355	163	5.9±0.2	26
Fibre C		5	Atmospheric	325	157	5.2±0.3	6
Fibre D		5.1	Atmospheric	315	153	5.4±0.2	15
Fibre E		5.2	Atmospheric	300	139	5±0.2	9
Fibre F		5.3	Atmospheric	294	130	4.3±0.3	12
Fibre G		5.4	Atmospheric	306	97	3.9	4

FIGURE 8.13: Tellurite TZBK HC-ARFs dimensions and pressures applied during the fibre draw.
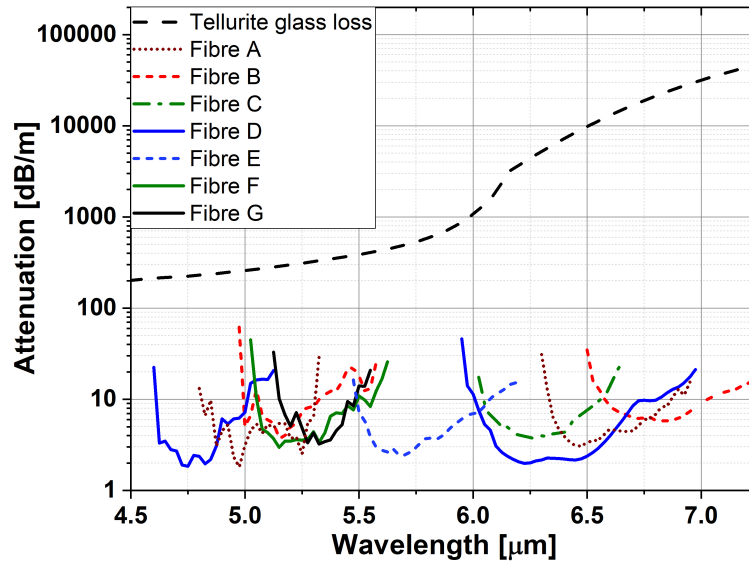
FIGURE 8.14: Simulations of the loss of the fabricated TZBK HC-ARFs through
the spark corroded die F. The black dashed curve represents the TZBK glass
loss.

Fibre F, which is the closest to the target TZBK HC-ARF, has simulated loss
between 3 and 11 dB/m in the 5.1-5.5 μm wavelength range. In particular, it has
loss of 7.1 dB/m at 5.4 μm, which is considerably higher than the target TZBK
HC-ARF. This is probably due to the variation of the thickness around the average
value and also to the shape of the capillaries, which are not completely circular.
In this work, not all these Fibres have been characterised. In particular, since the
predicted loss of fibres A and E have been simulated first compared to the other
fibres of Figure 8.12, only these fibres have been fully characterised.

8.4.2 TZBK tellurite HC-ARF characterisation

The fabricated tellurite HC-ARFs Fibre A and Fibre E have been characterised
and the experimental results compared with simulations. Infrared radiation from
the Thorlabs SLS202L lamp was coupled into a 36 cm long sample of Fibre A. The
output of the fibre, as imaged using a Xenics Onca MWIR 320 thermal camera
and shown in the inset of Figure 8.15a, indicates that most of the infrared light is
transmitted in the core. To measure the loss of Fibre A, its transmission spectrum
was measured 4 times (3 cuts) from 36 cm to 11.5 cm using a FTIR spectrometer.
Between 4.8 and 5.2 μm, the Fibre A shows losses between 6.8 and 36.8 dB/m
(solid light blue curve in Figure 8.15a). The minimum measured loss was at 5.11

μm. A cut-back was also performed on an adjacent piece of fibre by using the OPO [155] at the two wavelengths of 4.9 and 5 μm. The setup of the experiment was the same of previous OPO cut-back (Figure 8.9). The mode field diameter of the fibre and the spot size after the lens at 5 μm were $\sim$134 μm and $\sim$91 μm, respectively. At 4.9 μm, the output power was measured twice for a 1.10 m and a 0.91 m piece (1 cut). For the 5 μm measurement I measured the output power 4 times from 91 cm to 69 cm (3 cuts). The loss measured in this way was 14.2 and 8.2 $\pm$ 0.6 dB/m at 4.9 and 5 μm, respectively (black squared dots in Figure 8.15a). As shown in Figure 8.15a, these values of loss match very well with the losses measured by FTIR. This is different from the fibre shown in Figure 8.8, where the loss measured with the FTIR was higher than the one measured with the OPO. This indicates that for Fibre A, in the FTIR and OPO measurements, most of the light was launched into the fundamental mode. To measure the loss of Fibre E, two cut-backs were performed in a similar way using the OPO tuned to both 5.6 and 5.8 μm. In this case, the spot size after the lens at 5.8 μm wavelength was $\sim$104 μm and the mode field diameter of the fibre was $\sim$108 μm. At 5.6 μm, I performed 3 cuts (4 measurements) from 1.16 m to 0.9 m, while at 5.8 μm I did 2 cuts from 0.99 to 0.7 m. The measured loss was 4.8 $\pm$ 0.4 dB/m at 5.6 μm and 6.4 $\pm$ 0.4 dB/m at 5.8 μm (black squared dot in Figure 8.15b).
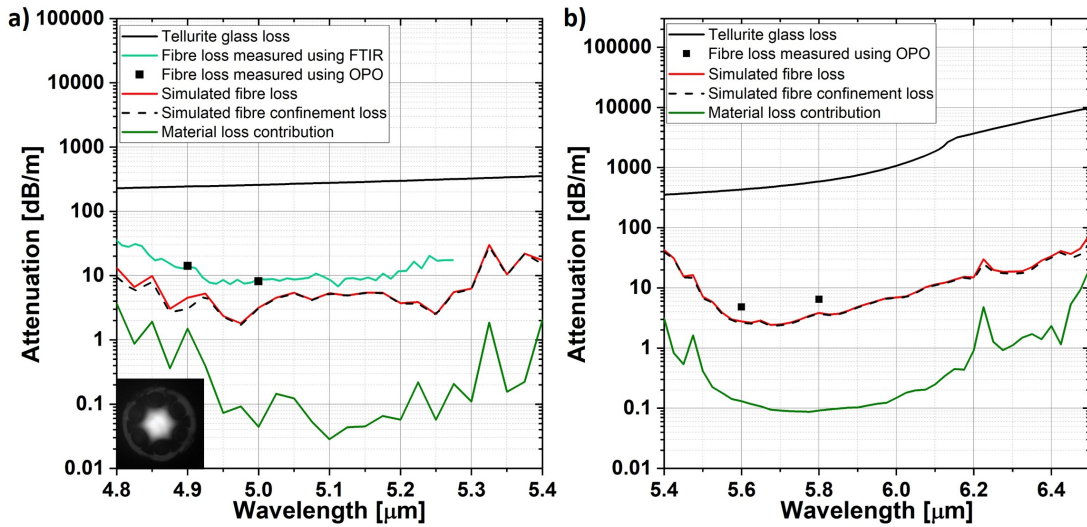
FIGURE 8.15: Attenuation simulated for (a) Fibre A and (b) Fibre E (solid red curve). The dashed black curve represents the simulated confinement loss of the fabricated fibre. The light blue curve represents the fibre loss measured using the FTIR. The black squared dots represent the fibre loss measured using the OPO. The green curve represents the modelling material loss contribution.
The black solid curve represents the loss of the fabricated tellurite glass.

These measured losses were then compared with simulations. The simulated loss of Fibre A is between 1.9 and 31.6 dB/m in the 4.8-5.4 μm spectral range, showing a minimum loss at 4.97 μm (solid red curve in Figure 8.15a). Fibre E has a simulated loss between 2.4 and 78 dB/m in the 5.4-6.5 μm wavelength range (solid red curve in Figure 8.15b). To assess the origin of these losses, the confinement loss of the fibre was also simulated (dashed black curve in Figure 8.15) and the expected contribution from material absorption has been calculated and it is shown as a green curve in Figure 8.15. As it can be seen, in both fibres the material absorption loss is one to two orders of magnitude lower than the confinement contribution, which hence dominates the overall loss. This could be due to the large gaps between the capillaries and non-uniformities in the capillaries.

Table 8.16 compares the measured and simulated losses of Fibre A and Fibre E. The measured losses in both fibres are somewhat higher than the simulation results. This could be attributed to a slight non-uniformity along the fibre which
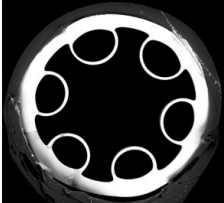
		Loss measured using FTIR		Loss measured using OPO		Simulated loss	
		λ (µm)	Loss (dB/m)	λ (µm)	Loss (dB/m)	λ (µm)	Loss (dB/m)
Fibre A		4.9	13.8	4.9	14.2	4.9	4.5
		5.0	8.8	5.0	8.2 ± 0.6	5.0	3.2
Fibre E		5.6	-	5.6	4.8 ± 0.4	5.6	2.8
		5.8	-	5.8	6.4 ± 0.4	5.8	3.8

FIGURE 8.16: Comparison between the measured and simulated losses of Fibre A and Fibre E.

is not captured by a simulation of an end cross-section, and potentially by other sources of loss like scattering and microbend which were not included in the simulation. Moreover, this discrepancy could be also due to poor launch and excitation of high order modes. It is also interesting to observe that, despite having a larger core, which normally would be expected to decrease the fibre leakage loss, Fibre A actually has a higher loss than Fibre E, and its loss is also more spectrally structured. This is observed in both measurement and simulation. This might

be explained by the fact that, as a result of a small difference between the two extruded preforms, probably arising from a small change in the quality of the two extruded billets which might result in a locally changing viscosity in the two glasses, Fibre E has capillaries with a smaller thickness non-uniformity than Fibre A. The standard deviation from the average capillary thickness decreases from 0.3 μm in Fibre A to 0.2 μm in Fibre E, and this, as I will show in the next section, can have a non-negligible impact on the overall loss. In addition, Fibre A and Fibre E transmit in the 4th and 3rd transmission bands, respectively. This makes the transmission band of Fibre A narrower and more susceptible to degradation through structural imperfections, which might explain the noisier spectral loss.

Since hollow core fibres are sensitive to bending [156], the bend loss of Fibre E, which has the lowest measured loss, was simulated as a function of the radius of curvature using the method explained in Section 6.3.1.2. Figure 8.17a shows the bending loss simulation of Fibre E at 5.6 μm.
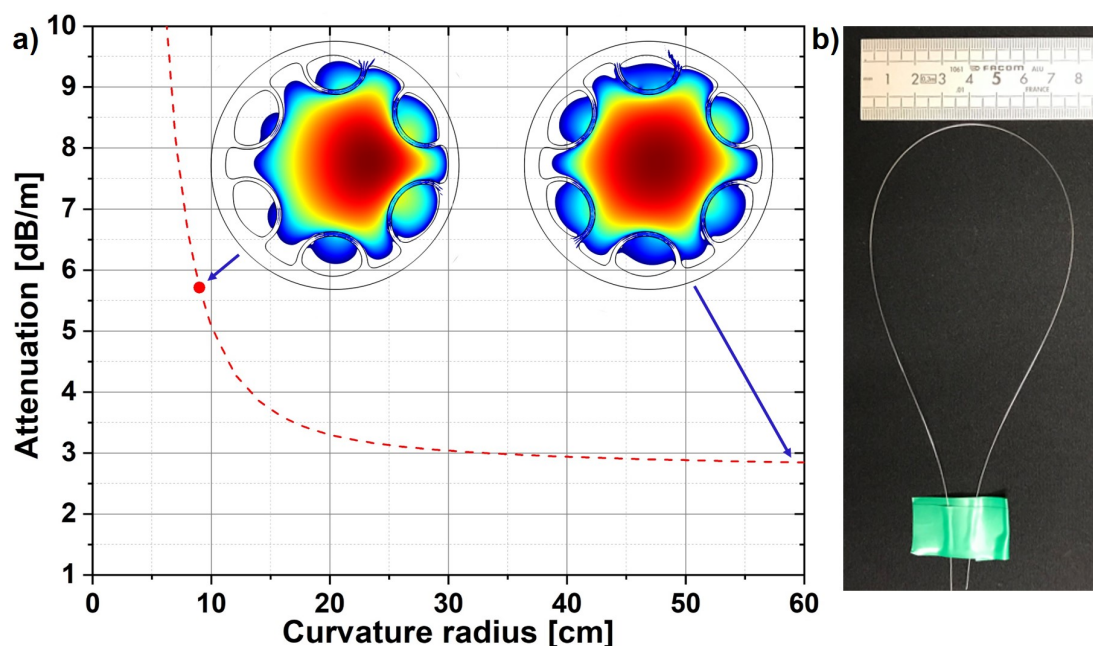
FIGURE 8.17: a) Bending loss simulation of Fibre E at 5.6 μm wavelength. The insets show the fundamental mode at 5.6 μm, for a fibre with a curvature radius of 60 cm and for a fibre with a curvature radius of 9 cm. b) Demonstration of the flexibility of the fabricated tellurite HC-ARF coated with FEP polymer.

The critical bending radius, defined as the radius at which the loss becomes double that of the straight fibre is estimated to be 9 cm. Up to bend radii of about 20 cm the loss does not increase significantly. Figure 8.17b shows the flexibility of the tellurite HC-ARF. The fibre can be bent with a curvature radius of 4

cm without breaking due to the extra mechanical strength provided by the FEP polymer coating. To assess the modal quality of Fibre E, the M^2 factor [157] was also measured at 5.6 μm at the output of a 13 cm long fibre. In particular, the beam diameter was measured at different beam positions by using a NanoScan 2s Pyro/9/5 pyroelectric detector. Figure 8.18 shows that an M^2 of 1.2 was obtained, indicating that the HC-ARF supports nearly single mode behaviour even after such a short length. I expect that an even lower M^2 should be obtainable after longer lengths of fibre, due to the high differential loss of its high order modes. To put this
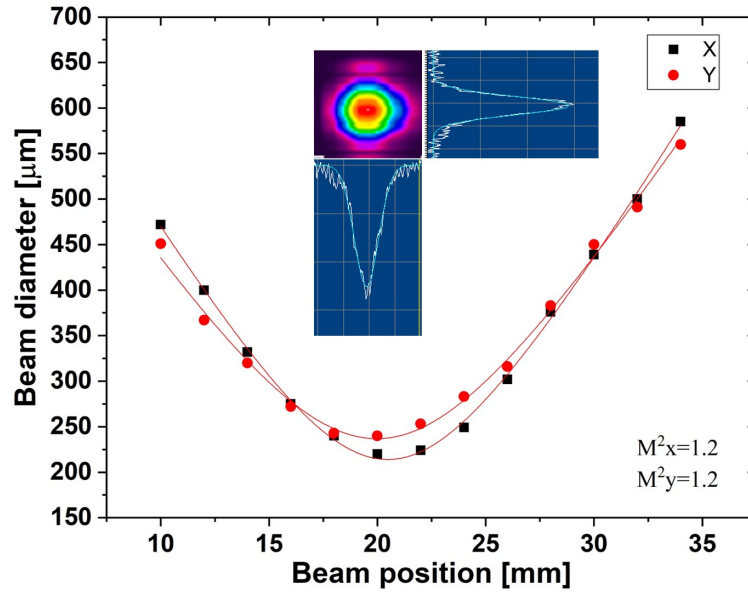
FIGURE 8.18: Beam quality at the output of the tellurite hollow core antiresonant Fibre E at 5.6 μm wavelength.

result into context, the HC-ARFs developed by Shiryaev et al. [33] and Gattass et al. [34] have transmission losses of the order of 3 dB/m at 4.8 μm and 1.7 dB/m at 4.7 μm, respectively. These values of loss are lower than the minimum loss of Fibre E. I believe that the good beam quality and the presence of a protective polymer coating, which give flexibility and protection to the fabricated fibres, represent the advantages of this work compared to these and other earlier attempts [32–34, 37].

8.4.3 Understanding the effect of membrane thickness uniformity and shape

Since the fabricated tellurite HC-ARFs have some non-uniformities in the capillaries that affect both the shape and the non-equal thicknesses along their membranes,

I performed a modelling study to assess the level of transmission loss that might be achieved by improving the fibre structure. In particular, Fibre E was investigated in more detail. An idealised structure of the fabricated fibre was designed (inset of Figure 8.19 with blue contour), in which each of the 6 capillaries were kept the same size but their thickness was made uniform. I achieved this by drawing them as concentric circles, as shown in Figure 8.19. The thickness of these circles is equal to the average radial thickness of each capillary. Simulating this structure indicates that by simply making the membranes more uniform in thickness, the loss would decrease to between 0.38 and 1 dB/m in the 5.5-6.2 μm spectral range (dashed-dotted blue curve in Figure 8.19). To decrease the leakage loss further, the
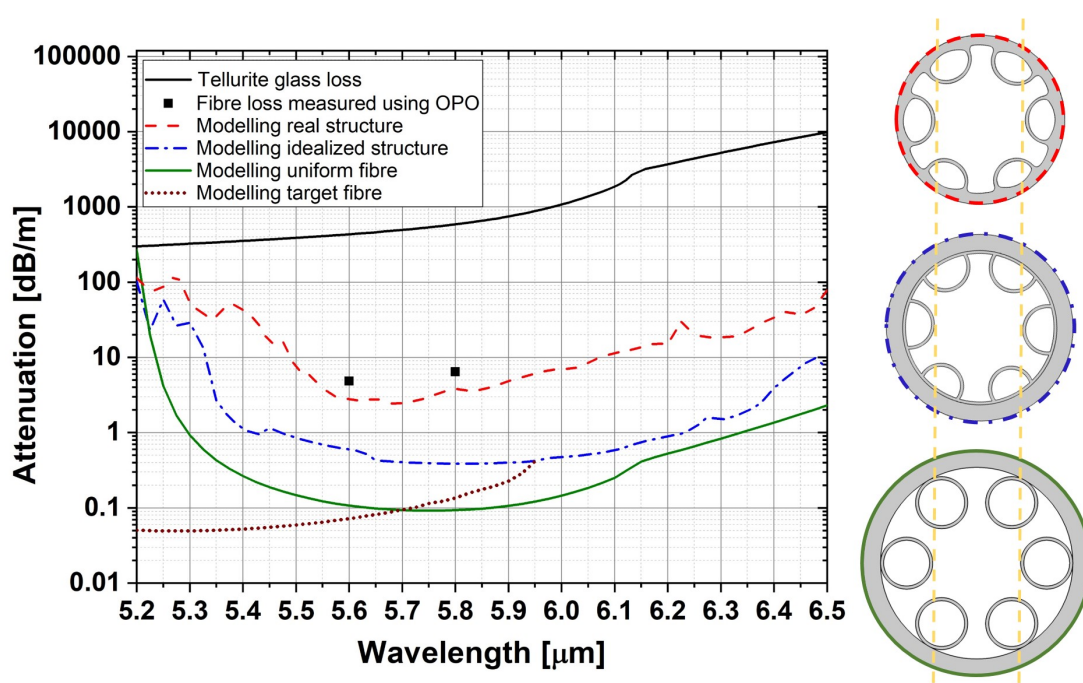
FIGURE 8.19: Comparison between the experimental loss of the tellurite antiresonant Fibre E (black squared dots), the simulation of the real fibre structure (dashed red curve), the idealised fibre structure (dashed-dotted blue curve) and the optimised fibre structure (green solid curve). The brown dotted curve represents the simulated loss of the target fibre structure. The black solid curve represents the loss of the fabricated tellurite glass.

ID of the capillaries should be increased in order to push the outer solid cladding further away from the optical mode. To check how much lower the loss might go, a HC-ARF with circular capillaries was simulated (solid green curve). This fibre structure has the same core diameter and capillaries thickness as the idealised fibre structure. As can be seen, this reduced the loss by a further factor of 3 to 5. A loss lower than 0.4 dB/m can be obtained between 5.35 and 6.15 μm, with a minimum of 0.09 dB/m at 5.75 μm. Despite the fact that the glass becomes pretty opaque

after 6.1 μm, see Figure 7.1, modelling results show that an optical loss of 2 dB/m could be in principle obtained in an optimised tellurite HC-ARF at 6.5 μm, nearly 5,000x lower than the glass absorption at that wavelength. This is due to the low overlap of the propagating fundamental mode with the cladding glass. To shift the operational window of the fabricated fibre to other wavelengths of operation, a different capillary thickness should be used. For example, to target the delivery of a CO laser at 5.4 μm, the capillary thickness should be reduced from 5 to 4.4 μm. In this way, the transmission band of the fibre would shift and produce a theoretical loss of 0.05 dB/m at 5.4 μm (brown dotted curve of Figure 8.19).

8.4.4 Tellurite HC-ARFs fabrication progress

Thanks to the optimisations performed on the glass material (e.g. overcoming the crystallisation problem), on the extrusion die and on the fibre fabrication process, HC-ARFs based on tellurite glass for mid-IR laser delivery with an increasing level of structural uniformity have been obtained during this project. The progress of the fabrication of tellurite HC-ARFs is summarised in Figure 8.20. In this project,
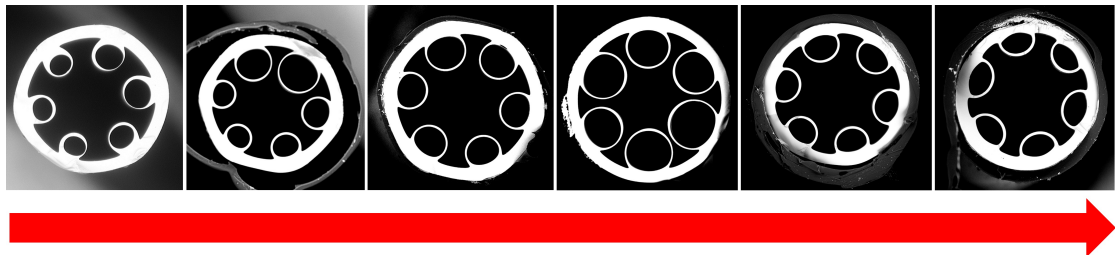
FIGURE 8.20: Tellurite hollow core antiresonant fibre progress.

more work needed to further improve the tellurite fibre structure and its loss. However, the results obtained in this project and the simulated predictions are promising. Next, I also fabricated a HC-ARF for CO_2 laser delivery as reported in the following section.

8.5 Vitron IG3 HC-ARF fabrication through the spark corroded complex die E

Having fabricated different successful tellurite HC-ARFs, I decided to move to the fabrication of HC-ARFs made of Vitron IG3 chalcogenide glass for CO_2 laser

delivery. As mentioned in Section 7.1.2, this glass transmits up to 12 μm opening up the possibility of a fibre which is transparent at 10.6 μm. To do so, I started to fabricate a HC-AR preform using the spark corroded complex die E, which is shown in Figure 7.12a. A commercial Vitron IG3 glass billet of 28 mm OD and 33 mm in length was extruded at $\sim$350 °C at a speed of 0.04 mm/min. The extrusion load was $\sim$28 kN. The cross-section of the extruded preform is shown in Figure 8.21a. The preform was 25 cm long and was straight. The ID and OD of the preform were 11.7 and 14.3 mm, respectively. The capillary thickness was 560 $\pm$ 90 μm.

The preform was inserted in a FEP polymer tube 15 mm ID and 17 mm OD, and they were co-drawn into a fibre at 360 °C. During the draw, only the capillaries were pressurised and the core was kept at atmospheric pressure. By applying 6 mbar of pressure into the capillaries, the fibre shown in Figure 8.21b was obtained. The Vitron IG3 chalcogenide HC-ARF was 2 m long, had an OD of $\sim$400 μm, a core diameter of $\sim$160 μm and capillaries 5.7 $\pm$ 0.8 μm thick. The loss of the
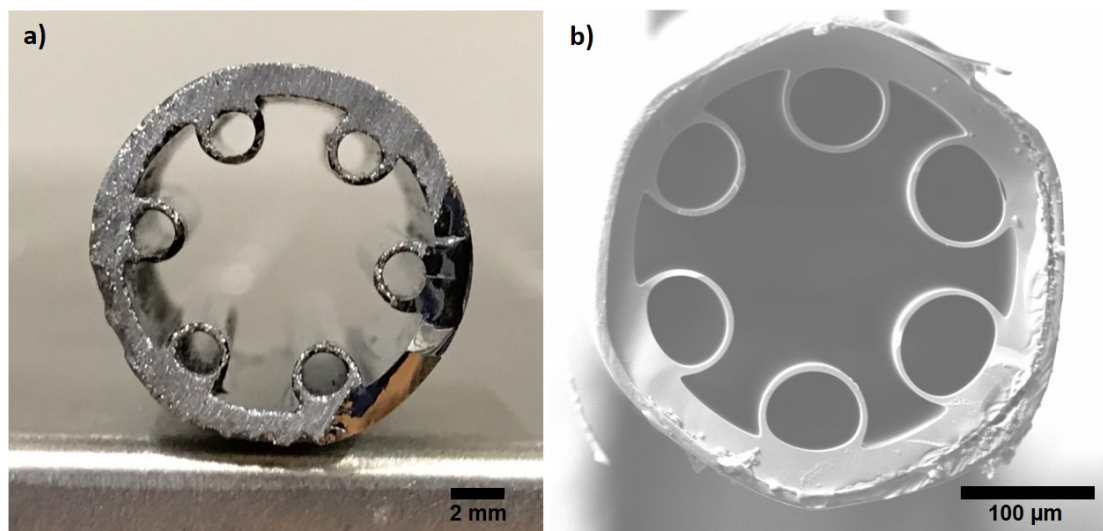
FIGURE 8.21: a) Vitron IG3 HC-AR preform and b) SEM picture of Vitron IG3 HC-ARF.

fabricated fibre has been simulated and it is shown as a blue curve in Figure 8.22. This figure indicates that the loss of the fibre is higher than 20 dB/m in the spectral region around 10 μm where the fibre is designed to operate and the transmission bands of the fibre are not clearly visible. This is due to the large capillaries variation. In order to understand the effect of the capillaries non-uniformity, a fibre structure with capillaries of constant thickness was simulated. In this case, it is possible to notice the transmission band of the fibre between 9.5 and 11.5

μm (dashed black curve in Figure 8.22). The minimum loss of this uniform fibre structure is of 0.6 dB/m at 10.1 μm. This demonstrates that by improving the capillary uniformity, loss lower than 1 dB/m can be achieved. This fibre has not
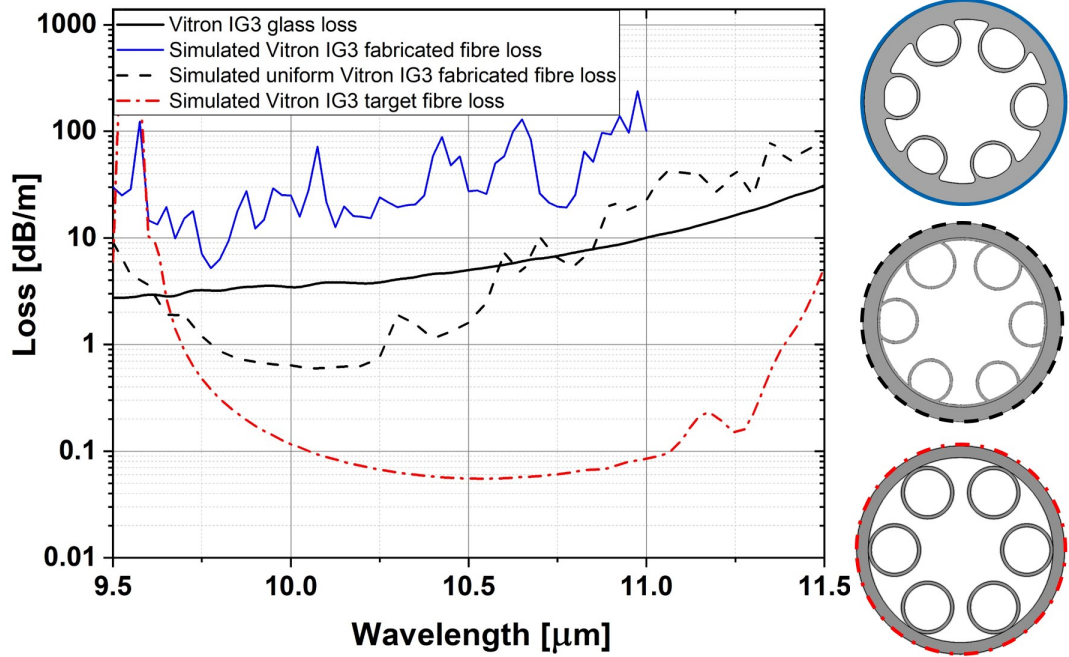
FIGURE 8.22: Simulation of the fabricated Vitron IG3 HC-ARF loss (solid blue curve), idealised Vitron IG3 fibre structure (dashed black curve) and target Vitron IG3 fibre structure (dashed-dotted red curve). The solid black curve represents the loss of the Vitron IG3 glass.

been characterised due to the absence of antiresonance band and due to its high estimated loss. Differently from TZBK glass, Vitron IG3 glass was not yet tested with the spark corroded die F. I believe that by using this die it would be possible to decrease the loss of the Vitron IG3 HC-ARF and to see the transmission bands.

8.6   Conclusions

In this chapter, the fabrication of HC-ARFs for CO and CO_2 laser delivery has been presented. In particular, after several optimisations of the glass, of the extrusion die and of the fibre fabrication process, tellurite HC-ARFs with loss of 8.2, 4.8 and 6.4 dB/m at 5, 5.6 and 5.8 μm, respectively, and a M^2 of 1.2 have been obtained. Moreover, thanks to the FEP polymer coating, the fibres can be coiled to radii down to 4 cm without permanent damage. By improving the flow in the

extrusion die to make the membranes more uniform and by applying more pressure into the capillaries to reduce the gaps and make them more circular, tellurite HC-ARFs with more uniform and circular capillaries can be obtained, opening up the possibility of flexible and long term durable fibres with sub 1-2 dB/m loss anywhere in the technologically important spectral region between 4.5 and 6.5 μm. In this work, the fabrication of chalcogenide HC-ARFs for CO_2 laser delivery through the extrusion and draw method was also demonstrated. The fibre, which had high non-uniformities and high simulated loss, did not show any transmission bands. Simulation of a Vitron IG3 HC-ARF with uniform capillaries predicted that loss of the order of 0.8 dB/m could be achieved in future works.

Chapter 9

Overall conclusion and future works

In this work, I investigated novel mid-IR optical fibres for thermal imaging and laser delivery.

In medical, industrial and military applications, there is a need to investigate hard to reach areas by using thermal imaging and to deliver mid-IR laser radiation to those areas. Thermal imaging in such areas can be done by using fibre bundles. Previous attempts on the fabrication of such bundles presented some limitations such as length, cross-talk, resolution and dimension. In this work, these limitations have been overcome. In particular, a fibre bundle made of 1200 chalcogenide core and FEP polymer cladding fibres was developed using the stack and draw method. The fibre bundle, which was 1.1 mm in diameter, was compact and flexible. Thanks to the high refractive index contrast between core and cladding, the intercore cross-talk was low and thermal images were not affected by image deterioration. Thermal images of a human hand were performed through a fibre bundle 62.5 cm long. A modelling study to understand how to improve the fibre bundle for future fabrications was reported. In particular, since objects at a low temperature as human body have the maximum infrared emission close to 10 μm, and cheap thermal cameras operate between 8 and 12 μm, the modelling study was oriented to fabricate a fibre bundle with low loss in that spectral range. Future work beyond the fibre bundle study presented in this thesis might look at the fabrication of an efficient fibre bundle transparent between 8 and 12 μm and with a length greater than 2 m. Thanks to my modelling study, which gives a good indication of the dimension of each pixel in the fibre bundle to achieve low transmission loss,

the fabrication costs and time will be hugely reduced. In particular, modelling demonstrated that in order to have a fibre bundle with low transmission loss in the 8 - 12 μm wavelength range, the pixel size of the fibre bundle should be larger than 80 μm in diameter. This will minimise the fraction of power in the cladding and will lead to a strong confinement of the ensemble of optical modes into the core. The only disadvantage of having such large pixels is that the fibre flexibility is compromised. To overcome this limitation, several subsets of the total bundle can be cemented together only at the bundle extremities. In this way, the subsets of the total bundle are indipendent and this would give flexibility to the bundle. Moreover, as mentioned in Chapter 4, it could be possible to purify the core material using distillation process in order to decrease even further the loss of the fibre bundle.

Mid-IR laser delivery to inaccessible points could be performed using optical fibres. In particular, from state of the art it was found that solid core fibres suffer from non-linearities of the fibre material and power handling limitations due to fibre melting. As an alternative, hollow core fibres can overcome these limitations. In particular, HC-ARFs have the most promising performances for laser delivery. Several HC-ARFs for CO and CO_2 laser delivery have been developed in the past. Those attempts had problems such as non-uniformity, length and absence of a protective coating. In this work, I fabricated the first tellurite HC-ARFs using the extrusion and draw method. This fabrication method allowed me to obtain uniform fibres and with losses such as 8.2, 4.8 and 6.4 dB/m at 5, 5.6 and 5.8 μm, respectively. Moreover, thanks to the use of FEP polymer as a protective jacket, the fibres were durable and flexible. In fact, these fibres can be bent with a curvature radius up to 4 cm without breaking. The fabricated tellurite HC-ARF had a M^2 of 1.2 after a length of 13 cm, demonstrating that the output beam is close to a Gaussian beam. Modelling study suggests that the shape and uniformity of the fibre can be improved in order to decrease the fibre loss. For this reason, in future works, I do envisage that, building on the work in this thesis, it should be possible to optimise the extrusion process and the fibre draw to obtain a tellurite HC-ARF with loss. A fibre with those low losses can be used to transmit CO laser radiation. In particular, the extrusion process can be improved by modifying the die design in order to compensate the deformations due to the glass swelling. The new die design can be optimised using an extrusion software as Ansys Polyflow. Having this new die would allow to obtain a preform with circular capillaries and with a lower standard deviation from the average capillary thickness obtained in

this work. In this way, more uniform fibres can be obtained and transmission loss lower than 0.4 dB/m between 5 and 6 μm can be achieved.

Moreover, in the present work, I started to fabricate a chalcogenide HC-ARF for CO_2 laser delivery. In this case, the fibre was also developed by using the extrusion and draw method and a FEP polymer coating was applied to protect the fibre. Unfortunately, this fibre had higher non-uniformities that resulted in a higher transmission loss compared to tellurite HC-ARFs. For this reason, the fibre did not have any transmission band. Future work beyond this thesis might focus on the fabrication of more uniform chalcogenide HC-ARFs. In particular, the optimisations achieved in the tellurite HC-ARFs fabrication, using the extrusion die F, could be used as a starting point to improve the uniformity of chalcogenide HC-ARFs. Also in this case, modelling of extrusion can be employed to optimise the shape and uniformity of the extruded preform. This would allow to achieve chalcogenide HC-ARFs with low transmission loss at 10.6 μm.

Moreover, it would be interesting to understand the resistance of tellurite and chalcogenide HC-ARFs to high laser power.

Appendix A

List of Publications

A.1 Journal Papers

Andrea Ventura, Fedia Ben Slimen, Joris Lousteau, Nicholas White, Ali Masoudi, Petr Janicek, Francesco Poletti, "Flexible Mid-IR fiber bundle for thermal imaging of inaccessible areas", Optics Express, 27(15), 20259-20272, 2019

Andrea Ventura, Juliano Grigoleto Hayashi, Jaroslaw Cimek, Gregory Jasion, Petr Janicek, Fedia Ben Slimen, Nicolas White, Qiang Fu, Lin Xu, Hesham Sakr, Natalie Wheeler, David Richardson Francesco Poletti, "Extruded Tellurite Antiresonant Hollow Core Fiber for Mid-IR Operation", Optics Express, 28(10), 2020

A.2 Conference Papers

Joris Lousteau, Nicholas White, Andrea Ventura, Ali Masoudi, Francesco Poletti, "Multimaterial mid-infrared transmitting fibre bundle for thermal imaging", The European Conference on Lasers and Electro-Optics, 2017

Joris Lousteau, Andrea Ventura, Nicholas White, Fedia Ben Slimen, Petr Janicek, Francesco Poletti, "Soft glass/polymer multimaterial fibre bundles for thermal imaging", Fifth Workshop on Specialty Optical Fibers and Their Applications—WSOF 2017, 2017

Fedia Ben Slimen, Joris Lousteau, Andrea Ventura, Walter Belardi, Nicholas White, Francesco Poletti, "Germanate glasses and fibres for 2 μm lasers and amplifiers", Fifth Workshop on Specialty Optical Fibers and Their Applications—WSOF 2017, 2017

Andrea Ventura, Joris Lousteau, Fedia Ben Slimen, Nicholas White, Francesco Poletti, "Development of Mid-IR Fiber Bundle for Thermal Imaging", Photoptics 2018, 2018

Andrea Ventura, Juliano Grigoleto Hayashi, Jaroslaw Cimek, Fedia Ben Slimen, Nick White, Hesham Sakr, Natalie V Wheeler, Francesco Poletti, "Tellurite Antiresonant Hollow Core Microstructured Fiber for Mid-IR Power Delivery", Frontiers in Optics + Laser Science APS/DLS, 2019

Juliano G Hayashi, Andrea Ventura, Gregory T Jasion, Jaroslaw Cimek, Fedia B Slimen, Nicholas White, Hesham Sakr, Natalie V Wheeler, Francesco Poletti, "Extruded Chalcogenide Antiresonant Hollow Core Fiber for Mid-IR Laser Delivery", Sixth International Workshop on Specialty Optical Fibers and Their Applications (WSOF 2019), 2019

Bibliography

[1] V. S. Aleinikov, V. P. Belyaev, N. D. Devyatkov, L. D. Mamedly, V. I. Masychev, V. K. Sysoev, "CO laser applications in surgery", Optics and laser technology, 16, 265 - 256 (1984)

[2] J. Sanghera, L. Brandon Shaw, L. E. Busse, V. Q. Nguyen, P. C. Pureza, B. C. Cole, B. B. Harbison, I. D. Aggarwal, R. Mossadegh, F. Kung, D. Talley, D. Roselle, R. Miklos, "Development and infrared applications of chalcogenide glass optical fibers", Fiber and Integrated Optics, 19, 251 - 274 (2000)

[3] E. F. J. Ring, and K. Ammer, "Infrared thermal imaging in medicine", Physiol. Meas., 33, R33 - R46 (2012)

[4] C. E. Rash, R. W. Verona, and J. S. Crowley, "Human factors and safety considerations of night vision systems flight using thermal imaging systems", Proc. SPIE, 1290, 142 - 164 (1990)

[5] B. F. Jones, "A reappraisal of the use of infrared thermal image analysis in medicine", IEEE Transaction on Medical Imaging, 17, 1019 - 1027 (1998)

[6] A. Glowacz and Z. Glowacz, "Diagnosis of three-phase induction motor using thermal imaging", Infrared Phys. Technol., 81, 7 - 16 (2017)

[7] H. Kaplan, "Pratical Applications of Infrared Thermal Sensing and Imaging Equipment", SPIE Press (2007)

[8] B. J. Peterson, H. Parchamy, N. Ashikawa, H. Kawashima, S. Knoshima, A. Y. Kostryukov, I. V. Miroshnikov, D. Seo, and T. Omori, "Development of imaging bolometers for magnetic fusion reactors", Review of scientific instruments, 79, (2008)

[9] R. Andoga, L. Fozo, M. Schrotter, M. Ceskovic, S. Szabo, R. Breda and M. Schreiner, "Intelligent thermal imaging-based diagnostis turbojet engines", Appl. Sci., 9, (2019)

[10] `https://www.fujikura.co.uk/products/medical-industrial-optical-fibre/image-fibre/` (Accessed March 2017)

[11] I. Paiss, and A. Katzir, "Thermal imaging by ordered bundles of silver halide crystalline fibers", Appl. Phys. Lett., 61, 1384 - 1386 (1992)

[12] E. Rave, L. Nagli, A. Katzir, "Ordered bundles of infrared-transmitting Ag-ClBr fibers: optical characterization of individual fibers", Opt. Lett., 25, 1237 - 1239 (2000)

[13] T. Lavi, A. Millo, A. Katzir, "Flexible ordered bundles of infrared transmitting silver-halide fibers: design, fabrication, and optical measurements", Appl. Opt., 45, 5808 - 5814 (2006)

[14] V. Gopal, J. A. Harrington, A. Goren, I. Gannot, "Coherent hollow-core waveguide bundles for infrared imaging", Opt. Eng., 43, 1195 - 1199 (2004)

[15] T. Kobayashi, T. Katagiri, Y. Matsuura, "Fabrication of bundle-structured tube-leaky optical fibers for infrared thermal imaging", Proc. SPIE, 10058, (2011)

[16] M. Saito, M. Takizawa, S. Sakuragi, F. Tanei, "Infrared image guide with bundled As-S glass fibers", Appl. Opt., 24, (1985)

[17] J. Nishii, T. Yamashita, T. Yamagishi, C. Tanaka, H. Sone, "Coherent infrared fiber image bundle", Appl. Phys. Lett., 59, 2639 - 2641 (1991)

[18] B. Zhang, C. Zhai, S. Qi, W. Guo, Z. Yang, A Yang, X. Gai, Y. Yu, R. Wang, D. Tang, G. Tao, B. Luther-Davies, "High-resolution chalcogenide fiber bundles for infrared imaging", Opt. Lett., 40, 4384 - 4387 (2015)

[19] F. Chenard, O. Alvarez, D. Gibson, L. Brandon Shaw, J. Sanghera, "Mid-infrared imaging fiber bundle", Proc. SPIE, 10181, (2017)

[20] S. Qi, B. Zhang, C. Zhai, Y. Li, A. Yang, Y. Yu, D. Tang, Z. Yang, B. Luther-Davies, "High-resolution chalcogenide fiber bundles for longwave infrared imaging", Opt. Express, 25, 26148 - 26153 (2017)

[21] T. Arai, and M. Kikuchi, "Carbon monoxide laser power delivery with an As_2S_3 infrared glass fiber", Appl. Opt., 23, 3017 - 3019 (1984)

[22] T. G. King, J. Powell, "Laser-cut mild steel - factors affecting edge quality", Wear, 109, 135 - 144 (1986)

[23] L. B. Kreuzer, N. D. Keyon, C. K. N. Patel, "Air pollution: sensitive detection of ten pollutant gases by carbon monoxide and carbon dioxide lasers", Science, 177, 347 - 349 (1972)

[24] B. Temelkuran, S. D. Hart, G. Benoit, J. D. Joannopoulos, and Y. Fink, "Wavelength-scalable hollow optical fibres with large photonic bandgaps for CO_2 laser transmission", Nature, 420, 650 - 653 (2002)

[25] B. F. Bowden, "Design theory, materials selection, and fabrication of hollow core waveguides for infrared to Thz radiation", (2007)

[26] J. A. Harrington, "Infrared fibers and their applications", SPIE Press, (2004)

[27] N. Croitoru, J. Dror, and I. Gannot, "Characterization of hollow fibers for the transmission of infrared radiation", Appl. Opt., 29, 1805 - 1809 (1990)

[28] J. S. Sanghera, L. Brandon Shaw, C. M. Florea, P. Pureza, V. Q. Nguyen, F. Kung, D. Gibson, and I. D. Aggarwal, "Nonlinear properties of chalcogenide glass fibers", Int. J. Appl. Glass Sci., 1, 296 - 308 (2010)

[29] F. Yu, and J. C. Knight, "Spectral attenuation limits of silica hollow core negative curvature fiber", Opt. Express, 21, (2013)

[30] A. N. Kolyadin, A. F. Kosolapov, A. D. Pryamikov, A. S. Biriukov, V. G. Plotnichenko, E. M. Dianov, "Light transmission in negative curvature hollow core fiber in extremely high material loss region", Opt. Express, 21, 9514 - 9519 (2013)

[31] G. Tao, H. Ebendorff-Heidepriem, A. M. Stolyarov, S. Danto, J. V. Badding, Y. Fink, J. Ballato and A. F. Abouraddy, "Infrared fibers", Adv. Opt. Photon., 7, 379 - 458 (2015)

[32] A. F. Kosolapov, A. D. Pryamikov, A. S. Biriukov, V. S. Shiryaev, M. S. Astapovich, G. E. Snopatin, V. G. Plotnichenko, M. F. Churbanov, and E. M.

Dianov, "Demonstration of CO_2-laser power delivery through chalcogenide-glass fiber with negative curvature hollow core", Opt. Express, 19, 25273 - 25278 (2011)

[33] V. S. Shiryaev, A. F. Kosolapov, A. D. Pryamikov, G. E. Snopatin, M. F. Churbanov, A. S. Biriukov, T. V. Kotereva, S. V. Mishinov, G. K. Alagashev, and A. N. Kolyadin, "Development of technique for preparation of As_2S_3 glass preforms for hollow core microstructured optical fibers", Journal of Optoelectronics and Advanced Materials, 16, 1020 - 1025 (2014)

[34] R. R. Gattass, D. Rhonehouse, D. Gibson, C. C. McClain, R. Thapa, V. Q. Nguyen, S. S. Bayya, R. J. Weiblen, C. R. Menyuk, L. Brandon Shaw, and J. S. Sanghera, "Infrared glass-based negative-curvature antiresonant fibers fabricated through extrusion", Opt. Express, 24, 25697 - 25703 (2016)

[35] W. Belardi, and P. J. Sazio, "Borosilicate based hollow-core optical fibers", Fibers, 7, (2019)

[36] H. T. Tong, N. Nishiharaguchi, T. Suzuki, and Y. Ohishi, "Fabrication of a novel tellurite hollow core optical fiber", Journal of the Ceramic Society of Japan, 127, (2019)

[37] H. T. Tong, N. Nishiharaguchi, T. Suzuki, and Y. Ohishi, "Mid-Infrared transmission by a tellurite hollow core optical fiber", Opt. Express, 27, (2019)

[38] J. M. Senior, "Optical fiber communications principles and practice", Pearson Education, (2009)

[39] N. S. Kapany, "Fibre optics. VI. Image quality and optical insulation", J. Opt. Soc. Am., 49, 779 - 787 (1959)

[40] A. W. Snyder and J. D. Love, "Optical waveguide theory", Chapman and Hall, (1983)

[41] G. P. Agrawal, "Fiber-optic communication systems", Wiley, (2002)

[42] G. Tao, A. M. Stolyarov and A. F. Abouraddy, "Multimaterial fibers", Int. J. Appl. Glass Sci., 3, 349 - 368 (2012)

[43] K. Okamoto, "Fundamentals of optical waveguides", Elsevier, (2006)

[44] G. H. Sigel Jr., "Optical absorption of glasses", Treatise on Materials Science and Technology, 12, (1977)

[45] J. S. Sanghera, and I. D. Aggarwal, "Infrared fiber optics", CRC Press, (1998)

[46] B. E. A. Saleh, and M. C. Teich, "Fundamentals of photonics", John Wiley and Sons, (1991)

[47] A. W. Snyder, "Power loss on optical fibers", Proceedings of the IEEE, 60, (1972)

[48] T. Kanamori, Y. Terunuma, S. Takahashi, and T. Miyashita, "Chalcogenide glass fibers for mid-infrared transmission", Journal of Lightwave Technology, 2, 607 - 613 (1984)

[49] J. B. MacChesney, P. B. O'Connor, and H. M. Presby, "A new technique for the preparation of low-loss and graded-index optical fibers", Proceedings of the IEEE, 62, 1280 - 1281 (1974)

[50] L. Cognolato, "Chemical vapour deposition for optical fibre technology", J. Phys. IV, 5, 975 - 987 (1995)

[51] E. Snitzer and R. Tumminelli, "SiO$_2$-clad fibers with selectively volatilized soft-glass cores", Opt. Lett., 14, 757 - 759 (1989)

[52] Q. Chen, H. Wang, Q. Wang, Q. Chen, and Y. Hao, "Modified rod-in-tube for high-NA tellurite glass fiber fabrication: materials and technologies", Appl. Opt., 54, 946 - 952 (2015)

[53] R. Wolfe, "Applied solid state science", Academic Press, (1976)

[54] A. R. Tynes, A. D. Pearson, and D. L. Bisbee, "Loss mechanisms and measurements in clad glass fibers and bulk glass", J. Opt. Soc. Am., 61, 143 - 153 (1971)

[55] V. M. Sglavo, "Advances in glass science and technology", Intrechopen, (2018)

[56] E. Roeder, "Extrusion of glass", J. Non-Cryst. Solids, 5, 377 - 388 (1971)

[57] H. Ebendorff-Heidepriem and T. M. Monro, "Analysis of glass flow during extrusion of optical fiber preforms", Opt. Mat. Express, 2, 304 - 320 (2012)

[58] J. C. Daly, "Fiber optics", CRC Press (1984)

[59] H. H. Hopkins, and N. S. Kapany, "A flexible fiberscope, using static scanning", Nature, 173, 39 - 41 (1954)

[60] "https://veteriankey.com/endoscopic-instrumentation-and-documentation-for-flexible-and-rigid-endoscopy/", (Accessed June 2017)

[61] N. S. Kapany, "Fiber optics", Academic Press, (1967)

[62] D. Pysz, I. Kujawa, R. Stepien, M. Klimczak, A. Filipkowski, M. Franczyk, L. Kociszewski, J. Buzniak, K. Harasny, and R. Buczynski, "Stack and draw fabrication of soft glass microstructured fiber optics", Bulletin of the Polish Academy of Sciences, 62, 142 - 164 (2014)

[63] J. Jin "The finite element method in electromagnetics", Wiley, (2014)

[64] B. M. Rahman and A. Agrawal, "Finite elements modeling methods for photonics ", Artech house, (2013)

[65] `https://www.comsol.com/comsol-multiphysics` (Accessed April 2017)

[66] Y Liu and G. Glass "Effect of mesh density on finite element analysis", SAE International, (2013)

[67] `http://people.ee.ethz.ch/~fieldcom/pps-comsol/documents/User%20Guide%20and%20Examples/WaveOpticsModuleUsersGuide.pdf` (Accessed March 2017)

[68] `https://www.mathworks.com/matlabcentral/fileexchange/27819-optical-fibre-toolbox` (Accessed May 2017)

[69] J. P. Berenger, "A perfectly matched layer for the absorption of the electromagnetic waves", J. Comput. Phys., 114, 185 - 200 (1994)

[70] Z. S. Sacks, D. M. Kingsland, R. Lee, and J. Lee, "A perfectly matched anisotropic absorber for use as an absorbing boundary condition", IEEE transaction on antennas and propagation, 43, 1460 - 1463 (1985)

[71] M. Imran Cheema, and A. G. Kirk, "Implementation of the perfectly matched layer to determine the quality factor of axisymmetric resonators in comsol", Proceedings of the Comsol Conference, (2010)

[72] F. A. Sowan, "Applications of infrared detector", Mullar Limited (1971)

[73] P. G. Datskos, N. V. Lavrik, "Detectors - figure of merit", CRC Press (2003)

[74] A. Rogalski, "Infrared detectors: status and trends", Progress in Quantum Electronics, 27, 59 - 210 (2003)

[75] B. G. Grant, "Field guide to radiometry", SPIE Press (2011)

[76] P. A. Jacobs, "Thermal infrared characterization of ground targets and backgrounds", SPIE The International Society for Optical Engineering (2006)

[77] `https://www.optex-fa.com/tech_guide/temp/guide/`, (Accessed November 2019)

[78] `https://www.hamamatsu.com/resources/pdf/ssd/infrared_kird9001e.pdf`, (Accessed May 2017)

[79] `http://support.fluke.com/find-sales/Download/Asset/3038318_6251_ENG_A_W.PDF`, (Accessed February 2019)

[80] J. A. Harrington, "Infrared fibers", Handbook of Optics, 4, McGraw Hill, (2000)

[81] J. Bei, H. T. C. Foo, G. Qian, T. M. Monro, A. Hemming, and H. Ebendorff-Heidepriem, "Experimental study of chemical durability of fluorozirconate and fluoroindate glasses in deionized water", Opt. Mat. Express, 4, 1213-1226 (2014)

[82] O. Mouawad, C. Strutynski, J. Picot-Clemente, F. Desevedavy, G. Garnet, J-C Jules and F. Smektala, "Optical aging behaviour naturally induced on As_2S_3 microstructured optical fibers", Opt. Mat. Express, 4, 2190-2203 (2014)

[83] M. Saito and K. Kikuchi, "Infrared optical fiber sensors", Opt. Rev., 4, 527 - 538 (1997)

[84] G. N. Merberg and J. A. Harrington, "Optical and mechanical properties of single-crystal sapphire optical fibers", Appl. Opt., 32, 3201 - 3209 (1993)

[85] D. Jayasuriya, B. Wilson, D. Furniss, Z. Tang, E. Barney, T. M. Benson and A. B. Seddon, "Towards mid-infrared fiber-optic devices and systems for sensing, mapping and imaging", Proc. SPIE, 9702, (2016)

[86] R. K. Nubling and J. A. Harrington, "Optical properties of single-crystal sapphire fibers", Appl. Opt., 36, 5934 - 5940 (1997)

[87] T. J. Bridges, J. S. Hasiak and A. R. Strnad, "Single-crystal AlBr infrared optical fibers", Opt. Lett., 5, 85 - 86 (1980)

[88] J. S. Sanghera, L. Brandon Shaw, I. D. Aggrawal, "Applications of chalcogenide glass optical fibers", C. R. Chimie, 5, 873 - 883 (2002)

[89] G. Qin, X. Yan, C. Kito, M. Liao, C. Chaudhari, T. Suzuki and Y. Ohishi, "Ultrabroadband supercontinuum generation from ultraviolet to 6.28 μm in a fluoride fiber", Appl. Phys. Lett., 95, (2009)

[90] A. B. Seddon, "Chalcogenide glasses: a review of their preparation, properties and applications", J. of Non-Cryst. Solids, 184, 44 - 50 (1995)

[91] H. T. Munasinghe, A. Winterstein-Beckmann, C. Schiele, D. Manzani, L. Wodraczek, S. Afshar V., T. M. Monro, and H. Ebendorff-Heidepriem, "Lead-germanate practical alternative to tellurite for nonlinear fiber applications", Opt. Mat. Express, 3, (2013)

[92] B. Zhou, C. F. Rapp, J. K. Driver, M. J. Myers, J. D. Myers, J. Goldstein, R. Utano, S. Gupta, "Development of tellurium oxide and lead-bismuth oxide glasses for mid-wave infra-red transmission optics", Proc. SPIE, 8626, (2013)

[93] https://www.infrared-materials.com/upload/13623009-1219schott-ig3.pdf (Accessed December 2016)

[94] G. E. Snopatin, V. S. Shiryaev, V. G. Plotnichencko, E. M. Dianov, and M. F. Churbanov, "High-purity chalcogenide glasses for fiber optics", Inorg. Mater., 45, 1439 - 1460 (2009)

[95] A. Zakery and S. R. Elliott, "Optical nonlinearities in chalcogenide glasses and their applications", Hardcover, (2007)

[96] J. Nishii, T. Yamashita, T. Yamagishi, "Chalcogenide glass fiber with a core-cladding structure", Appl. Opt., 28, 5122 - 5127 (1989)

[97] E. Rave, and A. Katzir, "Ordered bundles of infrared-transmitting silver halide fibers: attenuation, resolution and crosstalk in long and flexible bundles", Opt. Eng., 41, 1467 - 1468 (2002)

[98] T. Lavi, A. Millo, A. Katzir, "Thin ordered bundles of infrared-transmitting silver halide fibers", Appl. Phys. Lett., 87, (2005)

[99] U. Gal, J. Harrington, M. Ben-David, C. Bledt, N. Syzonenko, and I. Gannot, "Coherent hollow-core waveguide bundles for thermal imaging", Appl. Opt., 49, 4700 - 4709 (2010)

[100] Y. Matsuura, and K. Naito, "Flexible hollow-fiber bundle for body temperature imaging", Proc. SPIE, 7894, (2011)

[101] Thorlabs, "Stabilized tungsten light sources", User guide, (2017)

[102] ARCoptix, "Arcoptix FT-IR rocket", Data sheet, (2015)

[103] W. A. King, A. G. Claire and W. C. LaCourse, "Laboratory preparation of highly pure As_2Se_3 glass", J. Non-Cryst. Solids, 181(3), 231 - 237 (1995)

[104] `http://www.rjchase.com/fep_handbook.pdf` (Accessed January 2017)

[105] `https://www.fluorotherm.com/technical-information/ materials-overview/fep-properties/` (Accessed January 2017)

[106] A. M. S. Galante, O. L. Galante, L. L. Campos, "Study of application of the PTFE, FEP and PFA fluoropolymers on radiation dosimetry ", Nucl. Instrum. Method Phys. Res. A, 619, 177 - 180 (2010)

[107] `http://www.kpvision.co.kr/_upload/product/doc/201311261952581. pdf?PHPSESSID=47096b170372f62032d4821cb6b1f851&ckattempt=1` (Accessed March 2017)

[108] `https://www.spectrogon.com/product-services/optical-filters/ spectrogon-ab/broad-bandpass-filters/` (Accessed March 2017)

[109] `https://www.photonics.com/Products/ASIO_Microscopic_ Objectives_Lens/pr22959` (Accessed February 2017)

[110] `https://www.thorlabs.com/newgrouppage9.cfm?objectgroup_id=4791` (Accessed February 2017)

[111] A. W. Snyder, "Asymptotic expression for eigenfunctions and eigenvalues of a dielectric or optical waveguide", IEEE Trans. MTT, 17, 1130 - 1138 (1969)

[112] J. A. Harrington, "Infrared fiber optics", Handbook of Optics, 2nd ed., Vol III, McGraw Hill, (2011)

[113] T. Kanamori and S. Sakaguchi, "Preparation of elevated NA fluoride optical fibers", Japanese Journal of Applied Physics, 25, 468 - 470 (1986)

[114] M. F. Churbanov, G. E. Snopatin, V. S. Shiryaev, V. G. Plotnichenko, E. M. Dianov, "Recent advances in preparation of high-purity glasses based on arsenic chalcogenides for fiber optics", J. Non-Cryst. Solids, 357, 2352 - 2357 (2011)

[115] J. Nishii, S. Morimoto, I. Inagawa, R. Iizuka, T. Yamashita, and T. Yamagishi, "Recent advances and trends in chalcogenide glass fiber technology: a review", J. Non-Cryst. Solids, 140, 199 - 208 (1992)

[116] S. Sato, K. Igarashi, M. Taniwaki, K. Tanimoto and Y. Kikuchi "Multihundred-watt CO laser power delivery through chalcogenide glass fibers", Appl. Phys. Lett., 62, 669 - 671 (1993)

[117] F. Poletti, "Nested antiresonant nodeless hollow core fiber", Opt. Express, 22, (2014)

[118] B. Debord, F. Amrani, L. Vincetti, F. Gerome and F. Benabid, "Hollow-core fiber technology: the rising of gas photonics", Fibers, 7, (2019)

[119] E. A. J. Marcatili, and R. A. Schmeltzer, "Hollow metallic and dielectric waveguides for long distance optical transmission and lasers", The Bell System Technical Journal, 43, 1784 - 1809 (1964)

[120] P. Yeh and A. Yariv, "Bragg reflection waveguides", Optics communications, 19, 427 - 430 (1976)

[121] E. Garmiere, T. McMahon, and M. Bass, "Flexible infrared waveguides for high-power transmission", IEEE Journal of quantum electronics, 16, 23 - 32 (1980)

[122] T. A. Birks, P. J. Roberts, P. St. J. Russell, D. M. Aktin and T. J. Shepherd, "Full 2-D photonic bangaps in silica/air structures", Electronics letters, 31, (1995)

[123] J. R. Hayes, F. Poletti, M. S. Abokhamis, N. V. Wheeler, N. K. Baddela, and D. J. Richardson, "Anti-resonant hexagram hollow core fibers", Opt. Express, 23, 1289 - 1299 (2015)

[124] R. F. Cregan, B. J. Mangan, J. C. Knight, T. A. Birks, P. St. Russell, P. J. Roberts, D. C. Allan, "Single-mode photonic band gap guidance of light in air", Science, 285, 1537 - 1539 (1999)

[125] A. Hongo, K. Morosawa, K. Matsumoto, T. Shiota, and T. Hashimoto, "Transmission of kilowatt-class CO_2 laser light through dielectric-coated metallic hollow waveguides for material processing", Appl. Opt., 31, 5114 - 5120 (1992)

[126] N. M. Lichinitser, A. K. Abeeluck, C. Headley, and B. J. Eggleton, "Antiresonant reflecting photonic crystal optical waveguides", Opt. Lett., 27, (2002)

[127] K. Saitoh, M. Koshiba, "Confinement losses in air-guiding photonic bandgap fibers", IEEE Photonics Technology Letters, 15, 279 - 284 (2003)

[128] N. V. Wheeler, A. M. Heidt, N. K. Baddela, E. N. Fokoua, J. R. Hayes, S. R. Sandoghchi, F. Poletti, M. N. Petrovich, and D. J. Richardson, "Low-loss and low-bend-sensitivity mid-infrared guidance in a hollow-core-photonic-bandgap fiber", Opt. Lett., 39, (2014)

[129] F. Benabid, J. C. Knight, G. Antonopoulos, P. St. Russell, "Stimulated raman scattering in hydrogen-filled hollow-core photonic crystal fiber", Science, 298, (2002)

[130] A. D. Pryamikov, A. S. Biriukov, A. F. Kosolapov, V. G. Plotnichenko, S. L. Semjonov, and E. M. Dianov, "Demonstration of a waveguide regime for a silica hollow-core microstructured optical fiber with a negative curvature of the core boundary in the spectral region > 3.5 μm", Opt. Express, 19, 1441 - 1448 (2011)

[131] C. Wei, J. Hu, and C. R. Menyuk, "Comparison of loss in silica and chalcogenide negative curvature fibers as the wavelentgh varies", Frontiers in Physics, 4, (2016)

[132] P. Yeh, "Optical waves in layered media", Wiley, (2004)

[133] D. Bird, "Attenuation of model hollow-core, anti-resonant fibres", Opt. Express, 25, 23215 - 23237 (2017)

[134] C. Wei, C. R. Menyuk, and J. Hu, "Impact of cladding tubes in chalcogenide negative curvature fibers", IEEE Photonics Journal, 8, (2016)

[135] C. R. Menyuk, C. Wei, R. Joseph Weiblen, J. Hu, R. R. Gattass, L. Brandon Shaw, J. S. Sanghera, "Chalcogenide negative curvature fibers", Proc. SPIE, 10435, (2017)

[136] F. Yu, and J. C. Knight, "Negative curvature hollow-core optical fiber", IEEE Journal of Selected Topics in Quantum Electronics, 22, (2016)

[137] Y. Xu, G. X. Ouyang, R K. Lee and A. Yariv, "Asymptotic matrix theory of bragg fibers", Journal of lightwave technology, 20, 428 - 440 (2002)

[138] A. Martins, A. M. Rocha, B. Neto, A. L. J. Teixeira, M. Facao, R. N. Nogueira, M. J. Lima, P. S. Andre, "Modeling of bend losses in single-mode optical fibers", 7 th Conference on Telecommunications - Conftele, (2009)

[139] M. Heiblum, and J. H. Harris, "Analysis of Curved Optical Waveguides by Conformal Transformation", IEEE journal of quantum electronics, QE-11, 75 - 83 (1975)

[140] A. B. Sharma, A. H. Al-Ani, and S. J. Halme, "Constant-curvature loss in monomode fibers: an experimental investigation", Appl. Opt., 23, 3297-3301 (1984)

[141] G. D. Peng, "Handbook of optical fibers", Springer Nature Singapore, (2019)

[142] Y. Chen, Z. Liu, S. R. Sandoghchi, G. Jasion, T. D. Bradley, E. Numkan, J. R. Hayes, N. V. Wheeler, D. R. Gray, B. J. Mangan, R. Slavik, F. Poletti, M. N. Petrovich, D. J. Richardson "Demonstration of an 11km hollow core photonic bandagap fiber for broadband low-latency data transmission", IEEE, (2015)

[143] I. Savelii, F. Desedavy, J. C. Jules, G. Gadret, J. Fatome, B. Kibler, H. Kawashima, Y. Ohishi, F. Smektala, "Management of OH absorption in tellurite optical fibers and related supercontinuum generation", Opt. Mat., 35, 1595-1599 (2013)

[144] H. J. Hoffmann, "Optical glasses", Encyclopedia of Materials: Science and Technology, (2001)

[145] https://www.heraeus.com (Accessed February 2019)

[146] J. D. Shephard, A. Urich, R. M. Carter, P. Jaworski, R. R. J. Maier, W. Belardi, F. Yu, W. J. Wadsworth, J. C. Knight, and D. P. Hand "Silica hollow core microstructured fibers for beam delivery in industrial and medical applications", Frontiers in Physics, 3, 1 - 11 (2015)

[147] A. D. Pryamikov "Negative curvature hollow core fibers: design, fabrication, and applications", Proc. SPIE, 8961, (2014)

[148] J. Hu, C. Wei, R. J. Weiblen, C. R. Menyuk, R. R. Gattass, L. B. Shaw, J. S. Sanghera, and F. Chenard, "Recent progress on chalcogenide negative curvature fibers", IEEE, 209 - 213 (2018)

[149] T. D. Bradley, J. R. Hayes, G. T. Jasion, S. R. Sandoghchi, R. Slavik, E. N. Fokoa, S. Bawn, H. Sakr, I. A. Davidson, A. Taranta, J. P. Thomas, M. N. Petrovich, D. J. Richardson and F. Poletti, "Record low-loss 1.3dB/km data transmitting antiresonant hollow core fibre", IEEE 2018 European Conference on Optical Communication (ECOC), (2018)

[150] X. Feng, T. M. Monro, V. Finazzi, R. C. Moore, K. Frampton, P. Petropoulos and D. J. Richardson, "Extruded singlemode, high-nonlinearity, tellurite glass holey fibre", Electronics Letters, 41, (2005)

[151] V. V. Ravi Kanth Kumar, A. K. George, J. C. Knight, P. St. Russell, "Tellurite photonic crystal fiber", Opt. Express, 11, 2641 - 2645 (2003)

[152] G. T. Jasion, J. R. Hayes, N. V. Wheeler, Y. Chen, T. D. Bradley, D. J. Richardson, and F. Poletti, "Fabrication of tubular anti-resonant hollow core fibers: modelling, draw dynamics and process optimization", Opt. Express, 27, (2019)

[153] F. Yu, "Hollow core negative curvature fibres", Thesis, University of Bath (2013)

[154] G. T. Jasion, J. R. Hayes, N. V. Wheeler, Y. Chen, T. D. Bradley, S. R. Sandoghchi, M. Petrovich, D. J. Richardson, F. Poletti "Virtual draw of tubular hollow-core fibers", Frontiers in Optics OSA, (2018)

[155] Q. Fu, L. Xu, S. Liang, P. C. Shardlow, D. P. Shepherd, S.-U. Alam, and D.J. Richardson, "High-beam-quality, watt-level, widely tunable, mid-infrared OP-GaAs optical parametric oscillator", Opt. Lett., 44, 2744-2747 (2019)

[156] I. A. Bufetov, A. F. Kosolapov, A. D. Pryamikov, A. V. Gladyshev, A. N. Kolyadin, A. Krylov, Y. P. Yatsenko, A. S. Biriukov, "Revolver hollow core optical fibers", Fibers, 6, 1 - 26 (2018)

[157] A. E. Siegman, "New developments in laser resonators", Proc. SPIE, 1224, 75-83 (1990)